HIGH SURFACE AREA ELECTRODES FOR NEUROSTIMULATION OF THE RETINA

by

KARA MICHELLE ZAPPITELLI

A DISSERTATION

Presented to the Department of Physics
and the Graduate School of the University of Oregon
in partial fulfillment of the requirements
for the degree of
Doctor of Philosophy

September 2020

DISSERTATION APPROVAL PAGE

Student: Kara Michelle Zappitelli

Title: High Surface Area Electrodes for Neurostimulation of the Retina

This dissertation has been accepted and approved in partial fulfillment of the requirements for the Doctor of Philosophy degree in the Department of Physics by:

Tristan Ursell	Chair
Benjamín Alemán	Advisor
Dietrich Belitz	Core Member
Richard Taylor	Core Member
Cris Niell	Institutional Representative

and

Kate Mondloch	Interim Vice Provost and Dean of the Graduate School

Original approval signatures are on file with the University of Oregon Graduate School.

Degree awarded September 2020

DISSERTATION ABSTRACT

Kara Michelle Zappitelli

Doctor of Philosophy

Department of Physics

September 2020

Title: High Surface Area Electrodes for Neurostimulation of the Retina

Retinal degenerative diseases (RDDs), which cause the gradual death of rods and cones in the retina, impact millions of people all over the world, yet there are few clinically viable treatments and no cure. Multi-electrode array (MEA) - based retinal implants have emerged over the last two decades as a viable treatment option for those blinded by RDDs. Small electronic implants placed within the degenerate retina are able to restore vision to blind patients, however restored visual acuity (VA) is currently low. To provide patients with useful, high-resolution vision, electrode sizes must be decreased and the density of MEAs increased. As sizes decrease, small electrodes must pass increasingly more charge per unit area in order to provide enough current to stimulate the remaining retinal circuitry. The amount of charge needed often exceeds well-established safety limits that prevent electrode degradation and tissue damage. In order to safely provide enough current to the tissue, one aims to maximize electrode capacitance - the amount of charge an electrode can store for use in stimulation - by increasing the overall surface area without increasing the electrode footprint. In this dissertation, I approach surface area enhancement from the microscale and the nanoscale. I first investigate

how micro-patterning of electrode geometry with a fixed footprint can increase stimulation capability. I utilize an electric force microscopy (EFM) characterization technique to compare multiple different microscale electrode geometries. I then introduce vertically aligned carbon nanotubes (VACNTs) grown with chemical vapor deposition (CVD) as an ideal high surface area electrode material. I demonstrate VACNT biocompatibility with retinal neurons *in vitro* and show that high aspect ratio VACNTs can be integrated with silicon microfabrication processes to create an *in vivo* platform for rodent studies. Finally, I present work towards integrating these two approaches to create the next generation of high surface area retinal implant electrodes. Taken as a whole, this work offers promise for improving retinal neuron stimulation and restoring high VA to blind patients.

This dissertation includes previously published co-authored material.

CURRICULUM VITAE

NAME OF AUTHOR: Kara Michelle Zappitelli

GRADUATE AND UNDERGRADUATE SCHOOLS ATTENDED:

University of Oregon, Eugene, OR
California Polytechnic State University, San Luis Obispo, CA

DEGREES AWARDED:

Doctor of Philosophy, Physics, 2020, University of Oregon
Master of Science, Physics, 2019, University of Oregon
Bachelor of Science, Physics, 2013, Cal Poly - San Luis Obispo

AREAS OF SPECIAL INTEREST:

Neural Interfaces, Brain Computer Interfaces, Nanofabrication, Microscopy & Advanced Characterization

PROFESSIONAL EXPERIENCE:

Graduate Research Assistant, Alemán Lab, University of Oregon, 2014-2020
Graduate Teaching Fellow, Department of Physics, University of Oregon, 2014-2016

GRANTS, AWARDS AND HONORS:

Karfilis Women in Leadership Award, UOWGS, 2018
Weiser Senior Teaching Assistant Award, University of Oregon, 2016

PUBLICATIONS:

Watterson, W. J., Moslehi, S., Rowland, C., Zappitelli, K. M., Smith, J. H., Miller, D., Chouinard, J. E., Golledge, S. L., Taylor, R. P., Perez, M., & Alemán, B. J. The roles of an aluminum underlayer in the biocompatibility and mechanical integrity of vertically aligned carbon nanotubes for interfacing with retinal neurons. *Micromachines*, 11(6):546 (2020)

Zappitelli, K. M., Hipolite, D. N., & Saunders, K. Modeling the field control of the surface electroclinic effect near continuous and first-order smectic-A* to smectic-C* transitions, *Phys. Rev. E* **89**, 022502 (2014)

ACKNOWLEDGEMENTS

"So, it's kind of like the quest for the holy grail. Well, you know, who gives a shit what the holy grail is. It's the quest is what's important."

- Yvon Chouinard

And what a quest it has been. I'd like to start by thanking my advisor, Benjamín Alemán. Thank you for joining me on this wild adventure into the world of neuroscience and for pushing me, believing in me, and fighting with me through it all. You taught me how to see beauty in the things we create as scientists and, above all, how to tell a story.

A deep thank you to my committee chair, Tristan Ursell, for consistently going above and beyond. For perfectly timed and expertly crafted advice, without which I'd never have made it. To the rest of my committee - thank you for the support and feedback. Thank you to my collaborators, Maithe Perez and Trevor McGill, for paramount contributions to the animal work in this dissertation. And to Karl Saunders, for kickstarting my passion for research and encouraging me to check out a little school up in Oregon.

To my lab mates for inspiring me to be a better scientist and for showing me how much more fun it is when your colleagues are your friends. David Miller, for a decade of paving the way - excited to work with you forever and ever. Andrew Blaikie, for drinking more coffee than he ever wanted. Josh Ziegler, for Python, memes, and Ruby walks. Rudy Resch, for COMSOL and complaints. Brittany Carter, for shared observations and climbing. Rachael Klaiss, for taking over. To Kerisha Williams and Emily Hommerding for kicking this thing off right. And to Chase Craig for his programming contributions to this work.

To the Taylor Lab - especially Bill Watterson, Saba Moslehi, Conor Rowland and Julian Smith. Thanks for letting me crash your party and encouraging me to think differently. To the staff in CAMCOR - especially Kurt Langworthy and Fuding Lin, for helping me develop the skills necessary to do all of this work. And to Fuding, for teaching me to "just think about it" 6 years ago. To Meredith Sharps, Erik Hadland, and Mike Nellist, for getting me through that first summer and beyond.

To my partner and love, Tyler Swanson, for supporting me in the pursuit of my passion even if it meant being apart. For being there through the ups and downs, for all the travel, and for being my light at the end of a very long tunnel. To my parents, for never-ending support and encouragement. To my mom, who taught me to persevere. To my dad, who taught me to succeed. To my step-mom, who taught me to create. To my sisters - Lauren, Meg, Julie, and Mackenzie - who've taught me that intelligence, charisma, and grit come in all different shapes and sizes.

To my best friend, Kristen Hawkinson - for moving to Oregon, and for always being my number one supporter and low-key fangirl. To Alice Greenberg for being the best partner-in-crime without whom I'd never have survived physics graduate school. To Rosie Mueller, for being the best "roomie-bestie" and making Eugene feel like home. To Jameson and Teren for "The Kara". To my Lane 5 gym family for getting me in the best shape of my life - physically and mentally. To my wonderfully moody cat Puff. And to all of those who have hiked, camped, climbed, and drank their way through Oregon with me over the last six years - this one is for us.

And to Metallica, for writing Master of Puppets.

For Judy Powell-Miller

TABLE OF CONTENTS

LIST OF FIGURES

Figure Page

LIST OF TABLES

Table Page

CHAPTER I

INTRODUCTION

In the past few decades, the field of neural prostheses has seen rapid expansion throughout numerous areas of medicine [1][2]. These implantable electronic devices can be divided into two classes; those meant to record from neural tissue and those meant to stimulate neural tissue. Recording devices have been used extensively for applications in upper and lower limb prosthesis and researchers have made substantial strides towards closed loop feedback control of neural modulation [3][4][5]. In contrast, stimulating devices modulate neural tissue directly and have numerous therapeutic uses, including treatments for chronic pain, Parkinson's, depression, hearing loss, vision loss, and more [6][7][8][9].

Blindness especially has a staggering impact on the world. Degenerative retinal diseases like Retinitis Pigmentosa (RP) and Age-related Macular Degeneration (AMD) affect millions of people each year and have a substantial impact on patient quality of life [10][11]. Both of these diseases involve the gradual degeneration of photoreceptors in the retina, leading to eventual loss of vision. It is possible, however, to partially restore vision in these patients using small neurostimulation devices called retinal implants [9]. Retinal implants are composed of regularly spaced arrays of stimulating electrodes, or multi-electrode arrays (MEAs), that illicit a neural response by altering the ionic current flow near the target tissue [12]. The retinal implant market has grown substantially in the last decade, with two devices currently approved for clinical use [13][14], and many more in various stages of clinical trials [15][16][17]. While research in this area has

made significant progress, current devices still fail to restore sight to functional levels such that blind patients no longer need aid or assistance.

There are three types of retinal implants that have shown promise, epiretinal, suprachoroidal and subretinal. Each suffer from unique limitations distinct to their implantation and function [12]. Subretinal implants, which are placed at the back of the retina within the degenerate photoreceptor layer, have the advantage of restoring more "natural" vision, as the implant is able to utilize the remaining functional retinal circuitry [18]. These implants stimulate retinal bipolar cells, which respond to graded potentials and therefore require lower stimulation thresholds [19]. This threshold can be reached by integrating on-chip photodiodes into each pixel of the implant array to replace photoreceptor function directly. Despite lower thresholds, however, the world around us is often rather dim. Ambient light fails to provide the light intensity needed to power photodiode-based retinal stimulation by several orders of magnitude [20]. To obtain a strong enough signal to trigger a response in the bipolar cells, precious pixel space must be allocated for signal amplification [21]. As an added challenge, the inflammatory response of the body in the presence of a foreign object causes scar tissue build up at the electrode interface, resulting in a physical separation between the device and the target cells [22][23]. Both of these factors limit the efficacy of retinal stimulation electrodes and prevent the decrease in pixel size and spacing needed to restore high resolution vision.

While it is important to address the limitations above by maximizing current delivered to the tissue, particular care must be taken to avoid adverse effects over long stimulation time scales. Electrodes in a fluid environment, like the human body, have strict bounds on the voltage and pulse characteristics that can be

used to safely supply current to the tissue. Outside of these bounds, irreversible reactions occur at the electrode surface causing degradation of the material and damage to the surrounding tissue [24][25]. As size decreases, the amount of charge per unit area that an electrode must pass to adequately stimulate target cells quickly exceeds the safe charge injection limit of the electrode [26]. In order to reduce electrode size and safely maximize charge injection simultaneously, one aims to increase the electrode surface area available for charge transfer without increasing the overall electrode footprint. Increasing electrode surface area lowers electrode impedance and increases charge injection capacity, allowing for more efficacious stimulation [27]. Many avenues have been explored to increase the charge transfer surface area, including novel electrode geometries [28][23], materials [29], and surface modifications [26].

The broad challenge of enhancing retinal neuron stimulation can be re-framed simply: How can one maximize the surface area of an electrode within a pixel of finite size to most efficiently utilize a fixed power input? In this dissertation, I tackle this question using a two-pronged approach that probes surface area enhancement at both the microscale and the nanoscale. In Chapter II, I provide the background necessary for understanding my approach. In Chapter III, I provide experimental evidence that microscale patterning to maximize the perimeter-to-surface area ratio of an electrode enhances the stimulation capability. In Chapter IV, I introduce vertically aligned carbon nanotubes (VACNTs) as an ideal high surface area electrode material and demonstrate biocompatibility through a series of *in vitro* retinal cell culture experiments. In Chapter V, I show that VACNTs can be used as high aspect ratio electrodes for *in vivo* rodent studies by introducing an implantable platform. Finally, in Chapter VI, I present preliminary work

towards uniting microscale and nanoscale surface area enhancements into the next generation of retinal implant electrodes and outline future directions for this work.

CHAPTER II

BACKGROUND

2.1. The Retina & Retinal Implants

The human retina is a thin membrane of neurons, or nerve cells, that lines the back of the eye. When light enters the eye through the cornea, it is focused onto the retina by the lens. Light penetrates to the back of the retina where photosensitive cells convert incident light into an electrical signal in a process called phototransduction. This signal is transmitted forward through multiple distinct retinal layers to the optic nerve, which carries the signal to the brain to form an image. There are 5 different types of retinal neurons and each fulfill a critical role in human visual processing. A schematic of the retina can be seen in Fig. 2.1.

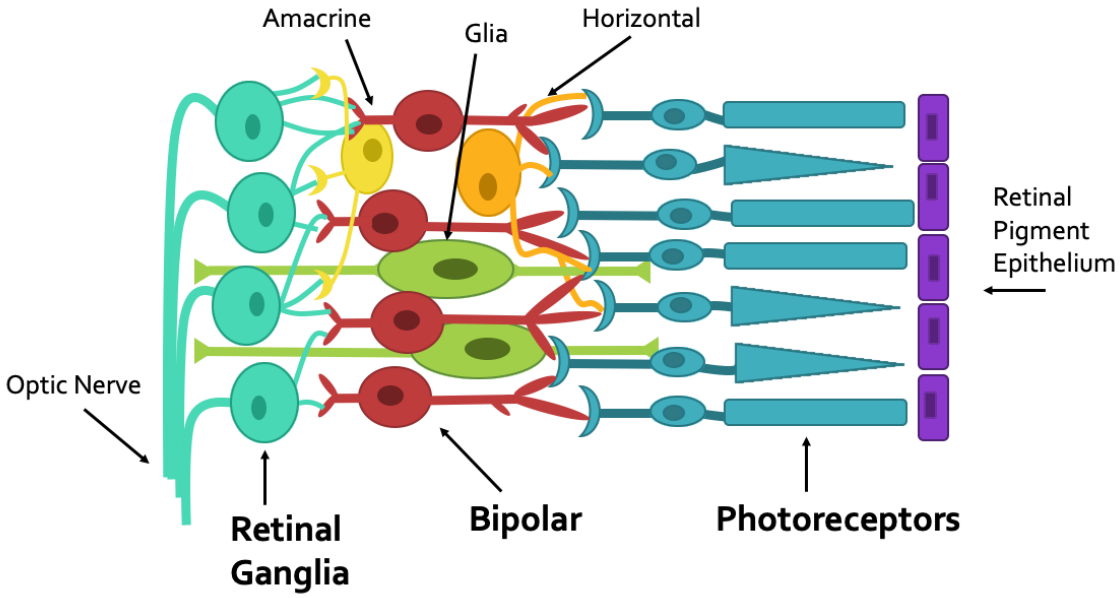

FIGURE 2.1. Schematic of the retinal cell layers.
There are multiple cell types contained within the human retina, including 5 different types of neurons and 3 types of glial cells.

Light is first absorbed by photopigment in the membranes of photoreceptors, or rods and cones, which induces a change in photoreceptor membrane potential [30]. Humans have three types of cone cells, which yield color vision at higher light intensities and are distinguished by their spectral selectivity [31]. Cones are concentrated in the center of the retina in a region called the macula and are responsible for high resolution central vision. Rods, which are 500-1000 times more sensitive than cones, are located in the outer retina and are responsible for peripheral and low light vision [32]. In most mammals, rods outnumber cones by a factor of 20 [33]. At the synaptic terminal of rods and cones, the light-evoked signal is passed to bipolar cells, which respond to graded potentials. There is one type of rod bipolar cell and at least 9 different types of cone bipolar cells which can be further subdivided into OFF and ON [31]. In the simplest case, this graded potential generates an action potential in the axon of a retinal ganglion cell (RGC), which is then routed to the brain via the optic nerve. Neighboring photoreceptors may also contact a horizontal cell at the synaptic terminal. Horizontal cells sum multiple signals and decrease individual photoreceptor illumination via feedback inhibition to increase contrast and reduce signal redundancy [31]. There are 29 different types of amacrine cells, which are involved in very specific tasks related to the control of ganglion cell responses. One example involves mediating the correlated firing of multiple ganglion cells, which is a form of multiplexing that can increase the carrying capacity of the optic nerve [33].

In addition to the five classes of neurons, the retina also contains a very large number of non-neuronal glial cells, or glia. Glia are an important component of the nervous system and serve many vital roles, including providing structural support to neurons, maintaining homeostasis, regulating neuronal communication, and

more [34]. There are three types of glia in the retina, Müller cells, astrocytes, and microglia. Although they vary in their developmental origin, they share many of the same functions. Müller cells are the primary glial cell and comprise ∼90% of retinal glia, forming much of the architectural support within the retinal layers. Müller cell processes ensheath the cell bodies and processes of retinal neurons, and it is likely that interactions between these two cell types promote synapse formation and maintain neuron function by providing them with energy substrates and neurotransmitter precursors [35]. Astrocytes are located primarily within the inner layers of the retina and are thought to be intimately involved in retinal vascularization and maintenance of the blood-retina barrier [34]. The third type of glial cell, microglia, play an important role in the immune response within the CNS [36].

Rods and cones in the retina serve a vital role and any disruption to their function has severe implications for human vision. Retinal degenerative diseases (RDDs), characterized by the gradual dysfunction or death of photoreceptors, impact millions of people throughout the world and are a leading cause of incurable blindness. RDDs can be roughly categorized as either monogenic or multifactorial (complex) [37]. Retinitis Pigmentosa (RP) and Age-related Macular Degeneration (AMD) are two of the most prevalent RDDs in each respective category, and are therefore of particular interest to the neural interface community. RP is a monogenic inherited disease that has a worldwide prevalence of approximately 1 in 4000 and affects more than 1 million people [10]. Disease onset begins with rod apoptosis in the mid-periphery, causing the loss of night vision and an eventual decrease in visual field, i.e. tunnel vision [38]. The disease slowly progresses inwards to the cones in the macula, often rendering patients legally blind by age 40 and

totally blind by age 60 [10]. AMD is a complex RDD with multiple suspected causes linked to genetics, age, and lifestyle [39]. It is the leading cause of blindness in the United States for individuals over the age of 65 [40]. Almost 3 million Americans suffer from late stages of the disease, resulting in a substantial impact to quality of life and billions of dollars in healthcare costs. There are two forms of AMD, wet and dry. Dry AMD accounts for 80-90% of cases and, in the later stages, results in geographic atrophy of the photoreceptors in the macula [41]. Contrary to RP however, photoreceptor degeneration in late stage dry AMD begins in the central vision and then progresses outwards towards the periphery [42]. A visual representation of the effects of these two diseases on human vision can be seen in Fig. 2.2.

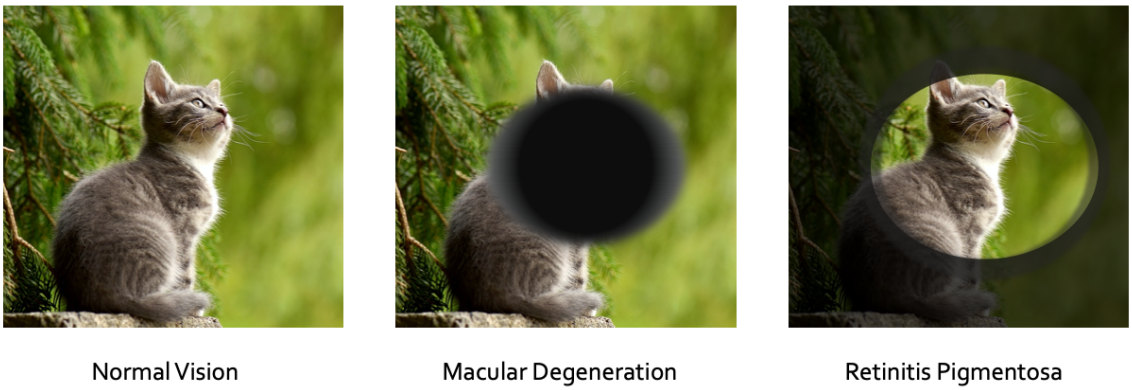

FIGURE 2.2. Retinal degenerative diseases.
Schematic showing how Age-related Macular Degeneration (AMD) and Retinitis Pigmentosa (RP) affect normal vision.

Neither RP nor late-stage dry AMD have a cure and universally adopted treatment options are limited or non-existent, respectively. Gene therapy has shown some promise for treating RP due to the monogenic nature of the disease, however early intervention in young patients may be required to prevent photoreceptor loss [43]. RP can result from a defect in any one of over 60 different genes, each

requiring a specific therapy that must independently clear the lengthy FDA approval process and be tailored to patients based on disease progression [44]. For these reasons, a more universal and timely approach is necessary. Stem cell implantation techniques have shown increasing promise for treating both RP and AMD photoreceptor loss [43][45]. Stem cell approaches to dry AMD typically involve the replacement of malfunctioning retinal pigment epithelial (RPE) cells, which contribute to eventual photoreceptor loss. This approach has seen some clinical success despite concerns regarding abnormal gene expression and adverse surgical effects, however long term safety and efficacy has not yet been demonstrated. Stem cell therapy techniques for RP involve replacing dead photoreceptors with transplanted cells directly, but implanted tissue integration with the host retina is an additional well-documented challenge [46].

A universal treatment for RP and AMD that is independent of the genetic root or underlying mechanism of photoreceptor degeneration would drive the retinal degenerative disease market. Retinal implants, which are small implantable electronic devices composed of arrays of neural stimulating electrodes, have shown promise for restoring vision to patients blinded by RP and AMD [9]. These devices are designed to circumvent the need for healthy photoreceptors and to interface directly with the remaining retinal circuitry to restore light perception. There are multiple categories of retinal implants that are distinguished from each other by their underlying principles of operation and anatomical location of implantation. The two types that have received the most attention from the scientific community and have shown the most clinical success to date are epiretinal and subretinal prostheses. Fig. 2.3 demonstrates the variation in placement between the two.

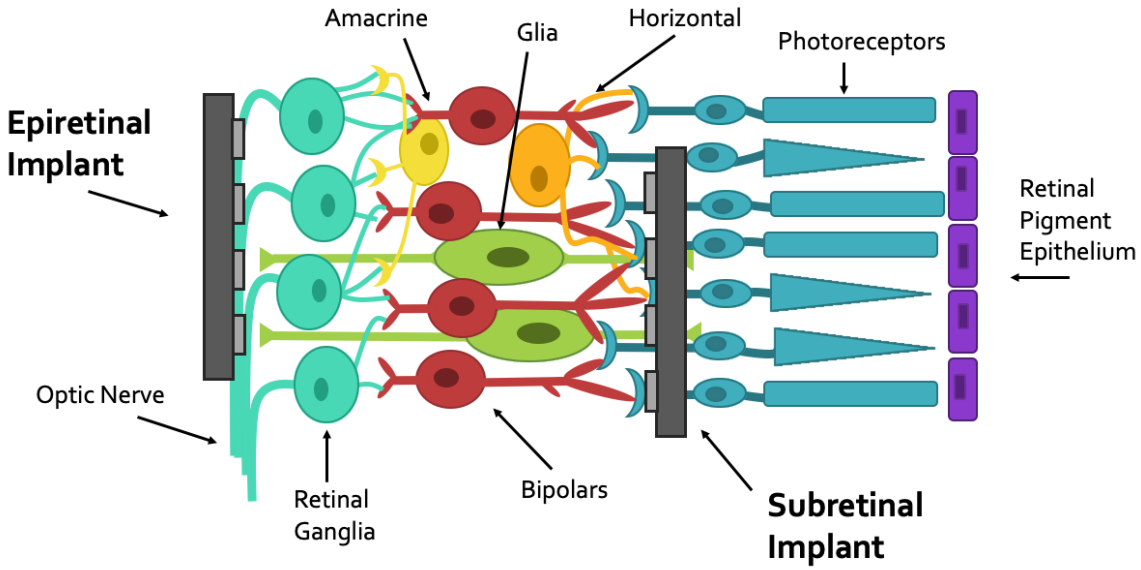

FIGURE 2.3. Epiretinal and subretinal implant placement. Schematic showing the difference in placement for epiretinal vs. subretinal implants. The implants are shown in gray.

Epiretinal implants are positioned on the front surface of the retina, adjacent to the optic nerve and RGCs. These devices aim to stimulate RGCs directly, bypassing the intraretinal circuitry [12]. The Argus II epiretinal prosthesis from Second Sight Medical Products (Sylmar, CA) is the first device of its kind to receive FDA approval (US) and CE marking (Europe) for the treatment of RP [13]. The system consists of a glasses-mounted video camera that captures real time images, which are then translated to electrical stimulating parameters by a visual processing unit. A radiofrequency (RF) coil attached to the glasses wirelessly transmits the data to a hermetically-sealed internal coil and associated integrated circuit attached around the eye. These components are wired to an array of 60 platinum microelectrodes on a flexible polyimide substrate which is then tacked to the surface of the retina. To date, the best recorded improvement in visual acuity for an RP patient implanted with the Argus II has been 20/1262 on the

Snellen scale [47]. Acuity in the epiretinal approach relies on the ability to elicit action potentials in individual RGCs. Axons from remote RGCs, however, must pass under the electrode as they group to form the optic nerve and are often inadvertently stimulated causing large distortions in the retinotopic map [48].

Subretinal implants are positioned within the degenerate photoreceptor layer and are designed to stimulate bipolar cells, thereby exploiting the intrinsic signal processing capability of the intraretinal circuitry and reproducing a more physiological form of vision [9]. In addition, the graded response of bipolars can be modulated based on stimulation amplitude and duration, allowing for greater control compared to the binary on/off response of RGCs [49]. The Alpha IMS (Retina Implant AG, Germany) subretinal implant obtained CE marking in Europe in 2013 [50]. The implant consists of a 1500-element microphotodiode array (MPDA) on polyimide foil which generates electrical signals based off incident light. To amplify these signals for effective stimulation, the implant is connected via a silicone cable to an RF coil affixed to the skull under the skin. This coil is then magnetically coupled to an external power source. This device was shown to restore acuity up to 20/546 in one RP patient, however technical failures during a 12 month implantation period have called device safety and longevity into question. A new generation of the device, the Alpha AMS, is expected to address these issues with comparable performance [51]. Even so, device acuity does not match theoretical predictions based on electrode array density. This is likely due to cross-talk between pixels resulting from a monopolar electrode configuration and physical separation from the target tissues [20].

Arguably one of the most exciting emerging technologies is the PRIMA bionic vision system (Pixium Vision, France), which has recently entered human

feasibility trials in Europe and the US for patients with late-stage dry AMD [15]. The system consists of a wireless photovoltaic array that is 2mm wide and 30μm thick, with 378 isolated 100μm pixels, as seen in Fig. 2.4. Unlike the two systems described above, this device does not need to be wired to external power and associated electronics, which greatly reduces risks and complications related to surgery. Instead, images captured by a camera mounted on a pair of glasses are processed and projected onto the retina using near-infrared (880nm) light. Multiple photodiodes within each pixel generate a voltage from the incident light. This generates a current flow between local active and return electrodes and stimulates nearby inner retinal neurons, mitigating pixel cross-talk [21]. At 12 months post-implantation, a visual acuity of 20/460 was reported - only 10% below the theoretical prediction for the pixel size and spacing [15].

Legal blindness corresponds to a visual acuity of 20/200 or worse. While progress in the field of retinal implants thus far has been truly remarkable, these devices are still a long way from restoring functional vision to those afflicted by RDDs. The PRIMA implant has addressed many of the shortcomings of its predecessors, but new challenges emerge as pixel sizes are decreased in pursuit of high resolution vision. The voltage produced by the photocircuit contained within each pixel must be sufficiently high such that current flow from the active electrode to the target tissue exceeds the threshold for retinal tissue stimulation. To reach this threshold, the PRIMA implant must employ multiple photodiodes in series [52]. Each additional photodiode, however, increases the size of the pixel and reduces the overall energy transfer efficiency by blocking incident light [21]. The introduction of a local return electrode bordering each pixel greatly reduces cross-talk and interference between neighboring electrodes, but simultaneously

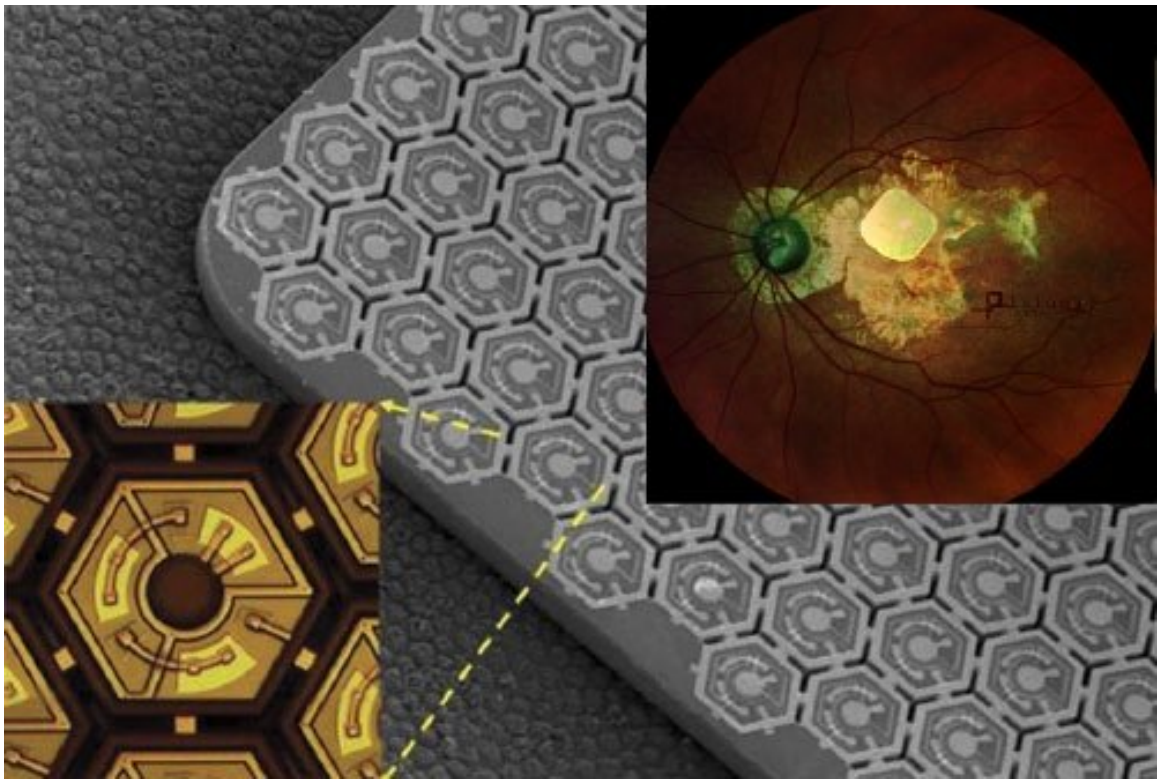

FIGURE 2.4. PRIMA bionic vision system.
The scanning electron microscope (SEM) image (grayscale image) shows the PRIMA bionic chip resting on retinal photoreceptors. The upper inset shows the device implanted in the eye of a patient with late stage AMD. The hexagonally shaped features are the active photovoltaic-based stimulating pixels, also shown in the lower inset [9].

reduces the penetration depth of electric current into the tissue. The penetration depth of the current in this configuration is roughly equal to the electrode diameter [53]. In a degenerate retina, the implant surface is separated from the target tissue by 20-50μm of photoreceptor debris [54]. This places a lower limit on electrode size - to stimulate retinal tissue 20-50μm away, the electrode must be at least 20-50μm in diameter. Fig. 2.5 schematically represents the challenges associated with decreasing retinal implant pixel size. In order to restore vision to useful levels for patients blinded by RDDs, one must find a way to maximize the stimulation range of small pixels.

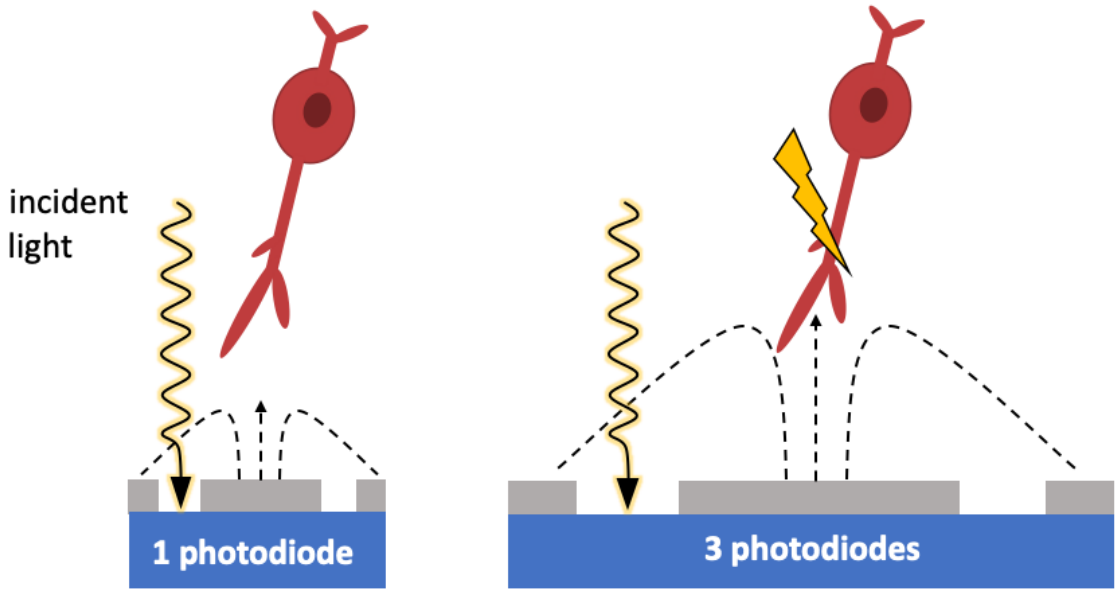

FIGURE 2.5. Trade-off between implant pixel size and stimulation efficiency This figure illustrates that although a larger, three-diode pixel will stimulate deeper into the tissue (dashed lines show electric field lines), it takes up more space than its single-diode counterpart, which decreases implant resolution.

2.2. Neural Stimulation

Paramount to engineering better neural electrodes is a fundamental understanding of how neural stimulation works from both a biological and an electrochemical perspective.

2.2.1. Eliciting a neural response

In their seminal work from the 1950's on giant squid axons, Hodgkin and Huxley developed the physical and mathematical framework to describe how electric signals, or action potentials, propagate in electrically excitable cells [55]. Current is generated by the opening and closing of ion channels in the membrane through which charged ions like sodium and potassium flow in and out, allowing

electrical signals to move through the cell and pass to other cells. Due to the distribution of sodium and potassium at steady state, the resting membrane potential of a neuron is -70mV. An extracellular potential that generates a membrane depolarization of ∼15mV will generate a response from the neuron [56][57].

As a first step towards understanding extracellular neural stimulation, myelinated nerve fibers can be modeled as a networked, infinite series of electronic circuit elements, represented by the circuit diagram shown in Fig. 2.6.

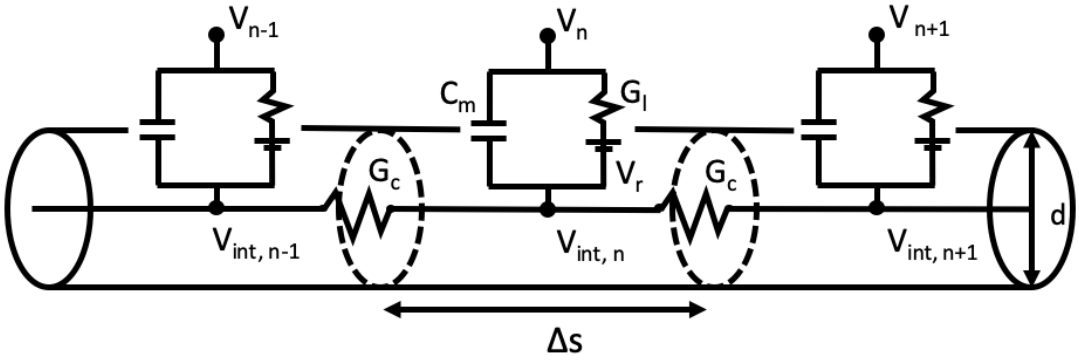

FIGURE 2.6. The cable model of an axon.
The cable circuit models the electric response of a neural axon due to extracellular currents. In this model, the potentials V_n correspond to spatially varying potentials outside the axon, G_l models the ionic leakage pathways and ion channels through the cellular membrane, C_m models the capacitance of the cellular membrane, and G_c models the ionic conductance inside the axon.

In this model, C_m is the membrane capacitance, G_l is the membrane leakage conductance, G_c is the internodal conductance, and $I_{i,n}$ is the total ionic inward current [58][59]. It is useful to express these as linear and surface quantities, summarized in Table 2.1, with internodal distance Δs, fiber diameter d, and intracellular resistivity ρ_i.

C_m	$c_m \pi d \Delta s$
G_l	$g_l \pi d \Delta s$
G_a	$\pi d^2 / 4 \rho_i \Delta s$
$I_{i,n}$	$i_{i,n} \pi d \Delta s$

TABLE 2.1. Reformulation of circuit elements in terms of linear and surface quantities

Applying Kirchhoff's Current Law to any node n in the circuit yields the expression,

$$C_m \cdot \frac{\mathrm{d}(V_{int,n} - V_n)}{\mathrm{d}t} + G_l \cdot (V_{int,n} - V_n - V_r) + I_{i,n} + G_a \cdot (2V_{int,n} - V_{int,n-1} - V_{int,n+1}) = 0 \quad (2.1)$$

Introducing the nodal membrane time constant $\tau = C_m/G_l = c_m/g_l$ and the fiber space constant $\lambda = \sqrt{G_a/G_l} \cdot \Delta s = \sqrt{d/4\rho_i g_l}$, and defining the membrane polarization $V_{m,n}$ at node n as the variation of the membrane potential around the resting potential V_r, we can rewrite the above Kirchoff equation as,

$$\tau \frac{\mathrm{d}(V_{m,n})}{\mathrm{d}t} - \lambda^2 \frac{V_{m,n-1} - 2V_{m,n} + V_{m,n+1}}{\Delta s^2} + V_{m,n} + \frac{i_{i,n}}{g_l} = \lambda^2 \frac{V_{n-1} - 2V_n + V_{n+1}}{\Delta s^2} \quad (2.2)$$

In the continuous limit of internodal distance, $\Delta s \to 0$, this becomes,

$$\tau \frac{\partial V_m(s)}{\partial t} - \lambda^2 \frac{\partial^2 V_m(s)}{\partial s^2} + V_m(s) + \frac{i_i(s)}{g_l} = \lambda^2 \frac{\partial^2 V(s)}{\partial s^2} \quad (2.3)$$

where s is the spatial coordinate along the fiber. Equation 2.2 and 2.3 are known as the cable equations for myelinated and non-myelinated fibers, respectively [59].

Analytical and numerical solutions of these equations have been obtained for a number of simple or specific neuron/electrode configurations, but no general solution exists that can be broadly applied to new systems in order to predict a neural response. Some useful and informative estimates of the membrane potential can be made, however, through a few basic assumptions. The passive cable equation is obtained by setting ionic currents ($i_i(s)$), which represent active channel conductances, to zero. Furthermore, we can obtain a simplified predictor of the membrane potential by considering the initial onset of stimulation, where the membrane potential $V_m(s) = 0$ and the capacitive currents across the cell membrane dominate over intracellular currents within the fiber (i.e. $\partial V_m/\partial t >> \partial^2 V_m(s)/\partial s^2$). Under these assumptions, the cable equation simplifies to,

$$V_m(s) \propto \mathrm{AF} = \lambda^2 \frac{\partial^2 V(s)}{\partial s^2} \tag{2.4}$$

which tells us that the initial membrane polarization is proportional to the second spatial derivative of the external potential, called the activating function (AF) [58] [60] [61]. The AF concept is a simple tool for gaining an initial understanding of how an applied electric field influences a target neuron that does not require solving the cable equation and it can provide qualitative predictions about the likelihood of neurostimulation. Despite it's simplicity, it has been used extensively throughout the literature as a feedback parameter for neural prosthesis design [62][63][64][65]. In addition, it has been shown that retinal neuron stimulation is more efficient with non-uniform electric fields under certain stimulation regimes [66].

A drawback of the AF concept is that it does not explain why neurons can be stimulated with uniform electric fields, where $\frac{\partial^2 V(s)}{\partial s^2} = 0$. This is due to the assumption that nerve fibers are infinite, one-dimensional systems, when in reality they are finite with boundary conditions that alter the excitation effects [59], and have complex multidimensional shapes. Introducing these finite boundary conditions yields a new "driving function" for the membrane potential at the ends of neural processes that is proportional to the magnitude of the electric field, rather than the gradient of the electric field [67]. A more rigorous prediction of the neural activation threshold, therefore, should consider both electric field strength **and** spatial variation.

2.2.2. Generating an extracellular voltage

In the previous section, I outlined how the presence of an extracellular electric signal can and will induce an electrical response from target neurons. For MEA-based neurostimulation applications, it is important to understand how these extracellular signals are generated by neural electrodes in the body.

The basic mechanism for inducing a neural signal involves a transduction of charge carried by electrons in the metal electrode to mobile ions in the physiological medium of the body. When an electrode is immersed in an electrolyte solution, an interfacial dielectric layer (called the electric double layer (EDL)) forms at the surface due to a reorganization of mobile ions in the fluid in response to a build up of electrons [68]. When a voltage is applied to an electrode, there is a large potential drop that occurs across the EDL, which greatly diminishes the current flow in the bulk electrolyte. A schematic of this reorganization can be seen in Fig. 2.7a.

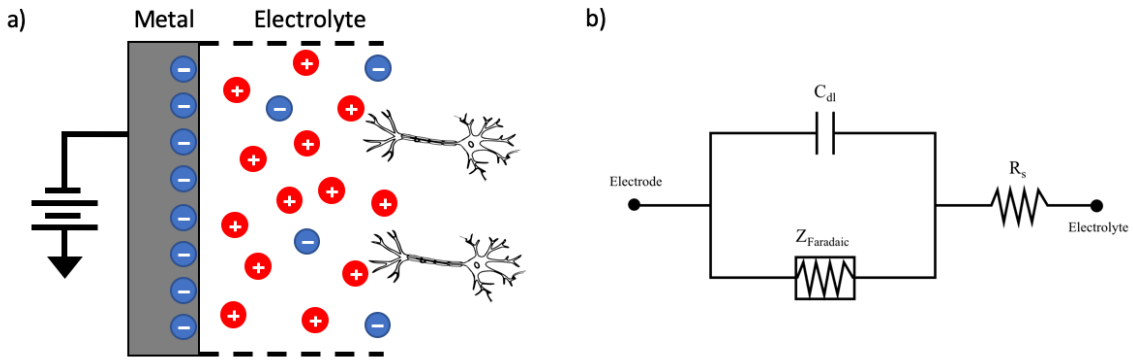

FIGURE 2.7. Electric double layer.
(a) The electric double layer (EDL) forms near an electrode surface in an electrolyte due the motion of ionic species (red cations, and blue anions). The EDL serves to neutralize the electric field in the solution bulk, and will determine the excitation potential of a neuron in the electrolyte. (b) The EDL can be modeled using an impedance Z_{Faradaic}, double-layer capacitance, C_{dl}, and a bulk solution resistance, R_s.

There are two main mechanisms of charge transfer at the electrode-electrolyte interface: Faradaic charge transfer and non-Faradaic (or capacitive) charge transfer. Faradaic charge transfer involves the physical transfer of electrons between the electrode and electrolyte, resulting in the oxidation or reduction of electrolytic species [25]. Capacitive charge transfer is characterized by the redistribution of ions in the fluid without physical electron transfer. The material interface can be represented by a capacitor (EDL) and complex impedance (Faradaic reactions) in parallel, as shown in Fig. 2.7b. Faradaic reactions can be further categorized as reversible or irreversible reactions based on whether or not the oxidation/reduction reactions permanently introduce new chemical species into the solution [24]. Irreversible Faradaic reactions create products that move away from the electrode surface into the electrolyte. These reactions should be avoided during neurostimulation because they can cause electrode corrosion, create biologically toxic products, and alter the pH landscape of the fluid. On the contrary, reversible

Faradaic reactions involve electron transfer between species bound to the electrode surface and can be reversed by passing current in the opposite direction. Even so, reversible Faradaic reactions can still alter fluid pH near the electrode surface, thereby altering the physiological environment of the tissue. For this reason, extra care must be taken when selecting stimulation parameters for reversible Faradaic charge injection [24].

Capacitive charge injection via the EDL is ideal from a safety standpoint because no chemical changes occur, but the amount of charge that can be injected before the onset of irreversible Faradaic reactions is typically lower than for reversible Faradaic reactions. This limit, called the charge injection limit or charge storage capacity (CSC) depends directly on the capacitance of the EDL for a given electrode, which is typically very small. Regardless, clinical adoption of neural prostheses requires long-term safety under chronic stimulation, often with large arrays of densely packed electrodes [69]. For these reasons, the hunt for the ideal capacitive electrode is ongoing.

Increasing the electrode capacitance effectively increases the ability of the electrode to inject charge. To understand why, we can use an RC circuit model for the electrolyte interface, as shown in Fig. 2.8.

Here we have two capacitors in series with a resistor, where capacitor C_1 is the working (or active) electrode and C_2 is the return (ground) electrode some distance away. For simplicity, we let $C_1 = C_2 = C$. The resistor, R_s represents the bulk electrolyte solution. The voltage drop across R_s due to the resistivity of the fluid serves as our estimate of the extracellular voltage. In order to overcome the charge screening of the electric double layer, time dependent voltages are used in neural stimulation. Therefore, we apply an AC bias to our circuit model,

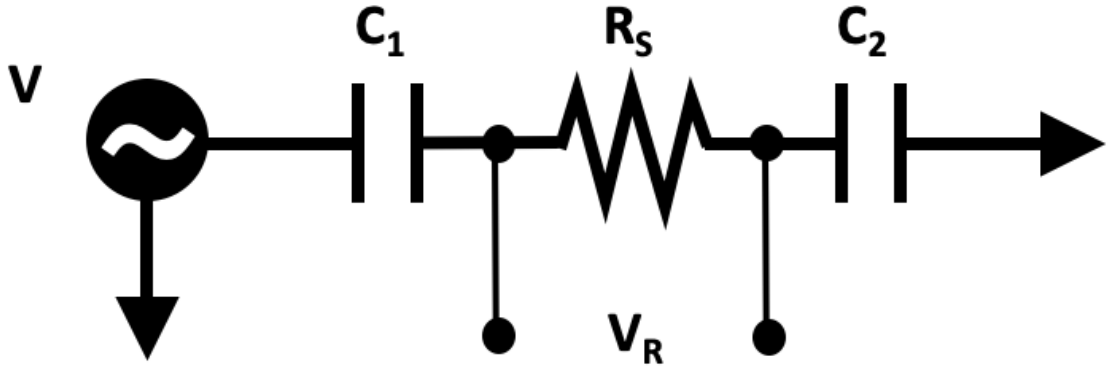

FIGURE 2.8. An RC circuit model for the potential in an electrolyte. The RC circuit used to model the potential landscape of the electrolyte due to an external A.C. potential V has a double layer capacitance at each electrode, C_1 and C_2, and the electrolyte resistance, R_S.

$V(\omega) = Ve^{i\omega t}$, where ω is the angular frequency. We can write the complex impedance of this circuit as,

$$|Z(\omega)| = \sqrt{R_s^2 + \left(\frac{2}{\omega C}\right)^2} \tag{2.5}$$

The current through the circuit is $I = V/Z$, so the voltage drop across the fluid, $V_R = IR_s = \frac{VR_s}{Z}$ is

$$V_R = \frac{V}{\sqrt{1 + \left(\frac{2}{\omega R_s C}\right)^2}} \tag{2.6}$$

From Eq. 2.6, we see the need to stimulate at "high" frequency (i.e. $\omega > \frac{1}{R_s C}$) in order to obtain practical values of V_R. More importantly for this discussion, taking the limit of $C \to \infty$ in Eq. 2.6, we obtain , $V_R \to V$, so the voltage across the resistor will equal the amplitude of the applied bias. Thus, increasing the electrode capacitance has the effect of maximizing the electric signal in the fluid.

In reality, the voltage profile in the bulk fluid is much more complex and drops off non-linearly with distance from the electrode surface. Increasing the capacitance, however, still has the effect of maximizing the current delivered to the tissue by the electrode.

2.3. High Surface Area Electrodes

From a retinal implant perspective, there is a demand for electrodes which increase the spatial range (depth) of stimulation for a fixed voltage input, especially as pixel sizes decrease. From an electrochemical perspective, the safety of electric stimulation is of utmost importance, particularly over long time scales. Capacitive electrodes are safe stimulators under the condition that they are not driven outside of their water window, the potential range characterized by the irreversible reduction of water in the negative direction, and the irreversible oxidation of water in the positive direction [25]. The charge storage capacity (CSC) of an electrode is directly proportional to the capacitance of the electric double layer C_{dl} and the overall electrode surface area available for charge transfer. As electrode size is decreased for high resolution implants, the amount of charge per unit area that an electrode must pass to adequately stimulate target cells requires voltages that exceed the water window limits [26]. Therefore, in order to safely inject more charge at smaller sizes, one aims to increase the surface area of the electrode without increasing the overall electrode footprint. Increasing electrode surface area increases the electrode capacitance and decreases electrode impedance, both of which contribute to more effective stimulation of target neurons [27].

One way to increase electrode surface area without increasing the overall electrode size is to use rough or porous conductive electrode materials or coatings.

This has the effect of increasing the electrochemical surface area (ESA) without altering the geometric surface area (GSA), which greatly improves charge transfer between the electrode and electrolyte [70]. Electrode surface roughening with reactive ion etching has been used to greatly increase the charge injection capacity of Faradaic Pt microelectrodes [71]. Sputtered Titanium Nitride (TiN) is one of the more popular purely capacitive materials that exploits this enhancement and for that reason has been used extensively as a coating for cardiac pacemakers [72][73]. Despite a CSC measured to be slightly lower than some widely-used Faradaic materials like iridium oxide, TiN is more compatible with CMOS processing and further increasing the ESA/GSA ratio could likely improve these numbers [29]. In addition, TiN microelectrodes have shown great promise for ultra-high resolution, low impedance neural recordings [74]. A new but promising class of electrodes utilize carbon-based based materials due to their high capacitance values, low impedance, and good biocompatibility. These materials, which are porous and highly textured, include carbon nanotubes, carbon nanofibers, and glassy carbon [75][76][77][78].

The added advantage of porous electrode materials may be limited by fluid resistance in the pores under high frequency stimulation, which limits the fraction of increased surface area can realistically be accessed for charge storage [27]. De Levie was the first to describe the frequency dispersion in porous electrodes in the absence of internal diffusion limitations, where only a fraction of a pore will take part in double layer charging [79]. We can talk about this in terms of the penetration depth λ_p of the AC current in the pore. This penetration depth can be defined as the square root of the ratio of the interfacial impedance to the pore

resistance. With no Faradaic charge transfer and only double layer capacitance, the penetration depth is given by,

$$\lambda_p = \sqrt{\frac{Z_{inter}}{R_{pore}}} \approx \frac{1}{2}\sqrt{\frac{\sigma r}{C_{DL}\omega}} \tag{2.7}$$

where σ is the solution conductivity and r is the pore radius. When the relative porosity effect is large, the penetration depth is small compared to the depth of the pores.

An alternative way to increase electrode surface area is by altering the physical shape of the electrode through micro-patterning. This technique, while not yet widely adopted in clinical neurostimulation, has been used extensively for applications in supercapacitors, solar energy storage, and antenna technology [80][81][82][83]. Microelectrodes with high perimeter-to-surface area (PSA) ratios result in a modest enhancement in charge injection capacity and a decrease in electrode impedance due to lower ionic solution resistance and higher counter-ion flux [28]. Patterned electrodes also offer a unique way to simultaneously maximize electrode surface area while minimizing blocked light due to their characteristic high PSA ratio. Fractal geometries have emerged as an ideal candidate for patterned electrodes due to their ability to maximize perimeter for a given volume. For this reason, these geometries have been utilized for flexible bioelectronics [84]. Simulations demonstrate that fractal shaped retinal implant electrodes generate larger and deeper-penetrating electric fields than Euclidean electrodes which block the same amount of light, which could correspond to substantial visual acuity enhancements [85][86]. Recent modeling and preliminary *in vivo* studies have shown a 22% reduction in power consumption in neurostimulation electrodes based off Sierpinski carpet fractals [87]. Furthermore, electrochemical

characterization of platinum electrodes resulted in an increased charge storage capacity for fractal geometries over other more simple geometries [88]. Interestingly, in addition to well-documented electrochemical improvement, high PSA electrodes have demonstrated larger activating functions further from the electrode surface due to an increase in the spatial non-uniformity of the current density, resulting in more efficient neurostimulation [89]. Likewise, Park et. al [88] reported higher current density and increased spatial non-uniformity above the surface of fractal electrodes, suggesting the ability of fractal geometries to increase the neural activating function.

CHAPTER III

FIELD GRADIENT PENETRATION OF PATTERNED ELECTRODES FOR NEUROSTIMULATION

3.1. Introduction

As discussed in the previous section, microscale electrode patterning can increase the perimeter-to-surface-area (PSA) ratio and, as a result, enhance the neurostimulation capabilities of electrodes. A higher PSA has two principle effects, both related to an increase in capacitance. The first is larger currents above the electrode surface. The second is that the magnitude of the activating function, defined as

$$V_m(z) \propto \frac{\partial^2 V}{\partial z^2} = -\frac{\partial E}{\partial z} = -\frac{1}{\sigma}\frac{\partial J}{\partial z}, \tag{3.1}$$

will be larger at distances much farther from the electrode surface [89][88]. These features are of particular benefit to photovoltaic subretinal implants because electrodes with significantly higher surface area, like fractal geometries, can be designed such that they block the same amount of light per pixel as their Euclidean counterparts. This serves as a way to maximize the signal output of an implant pixel for a fixed input.

In order to assess the neurostimulation performance of differing electrode geometries, many studies rely on either computer simulations or electrochemical measurements [88][89][85][85][27]. Simulations have many limitations, especially in neuroscience where incredibly complex systems must be greatly simplified to match computation power. Electrochemical measurements only allow one to

make generalizations about the performance of different electrode geometries and provide macroscopic information (i.e. capacitance, charge injection, etc.). Bulk electrochemistry thus does not provide information on the microscopic, localized electric fields. Yet, location specific information is an important feedback mechanism for electrode design, especially when trying to maximize signal penetration above implant surfaces. In addition, certain electrode geometries may have regions of extremely high current which could cause local tissue and electrode damage, or as a positive consequence, hotspots of neural stimulation. Given the limitations of simulations and electrochemical approaches, fine spatially resolved measurements of the activating function have proven elusive.

To understand the effect of sub-micron scale patterning of neural electrodes on their stimulation strength, we experimentally measure the gradient of the electric force at different distances above various electrode geometries. The gradient of the electric force is proportional to variations in both electric field and current density. In our approach, we utilize an atomic force microscopy technique called electric force microscopy (EFM) to map the resonance phase shift in response to the electric force of different Euclidean and fractal electrode geometries in air. We then compare these measurements to finite element simulations of identical electrode geometries. Via both EFM measurements and simulations, we find that geometries with a larger edge perimeter have electric field gradients that extend farther above the electrode surface and therefore increase the likelihood of deep-tissue neurostimulation.

3.2. Electric Force Microscopy

Electric force microscopy (EFM) is an atomic force microscopy (AFM) technique that utilizes a lift-mode scanning approach to map out electric force gradients above a sample surface. In tapping mode AFM, a conductive AFM tip is scanned across the sample surface, line-by-line, to map the sample topography. After each topographic line scan, the cantilever is lifted above the sample surface by a user-defined amount and re-scanned. During the re-scan, a bias is applied between the tip and sample and electrostatic forces cause a shift in the resonant phase of the cantilever [90].

The behavior of an AFM cantilever in tapping mode AFM can be modeled as a driven damped simple harmonic oscillator:

$$\ddot{x} + 2\beta\dot{x} + \omega_0^2 x = f_0 \cos(\omega t) \tag{3.2}$$

where ω_0 is the resonance frequency of the cantilever and the RHS is the time-dependent driving force with frequency ω. Solutions to Eq. 3.2 are of the form $x(t) = A(\omega)\exp\left(i\omega t + \phi(\omega)\right)$, where the amplitude and phase of the AFM cantilever oscillation are given by the expressions:

$$A(\omega) = \frac{f_0}{((\omega^2 - \omega_0^2)^2 + 4\beta^2\omega^2)^{1/2}} \tag{3.3}$$

and

$$\phi(\omega) = \tan^{-1}\left(\frac{2\beta\omega}{\omega^2 - \omega_0^2}\right). \tag{3.4}$$

The frequency of the resonator, ω_0, is determined by the geometry and mechanical elasticity of the cantilever–which will remain constant– but also by local forces, which are a function of the tip position relative to the sample surface. This typically includes electrostatic forces like Van der Waals interactions. In normal amplitude-modulation tapping mode AFM, one tracks the changes to $A(\omega)$ at fixed ω due to spatial variations of ω_0. The typical topographic images of tapping mode map the vertical (i.e. tip-surface distance) displacement of the tip needed to keep $A(\omega)$, and thus ω_0, constant.

In EFM, the phase shift due to the electrostatic force, F, is given by,

$$\Delta\phi \approx \frac{Q}{k}\nabla F \tag{3.5}$$

where Q is the quality factor of the cantilever and k is the spring constant [91]. The potential energy of a capacitor is $U = \frac{1}{2}CV^2$, where C is the capacitance and V is the potential difference. Since $F \equiv -\nabla U$, the 1D force gradient in the z-direction is,

$$\nabla F = \frac{1}{2}\frac{\partial^2 C}{\partial z^2}V_{DC} \tag{3.6}$$

where C is the tip-sample capacitance and V_{DC} is the applied DC bias. These shifts are captured in the phase data and allow the user to map out the qualitative electric force gradient in the x, y, and z dimensions above the sample surface.

The tip-sample capacitance C is a complex function that intimately depends on both the tip geometry and the geometry of the electrode it is scanning. This becomes even more complex when electrode geometries deviate from Euclidean

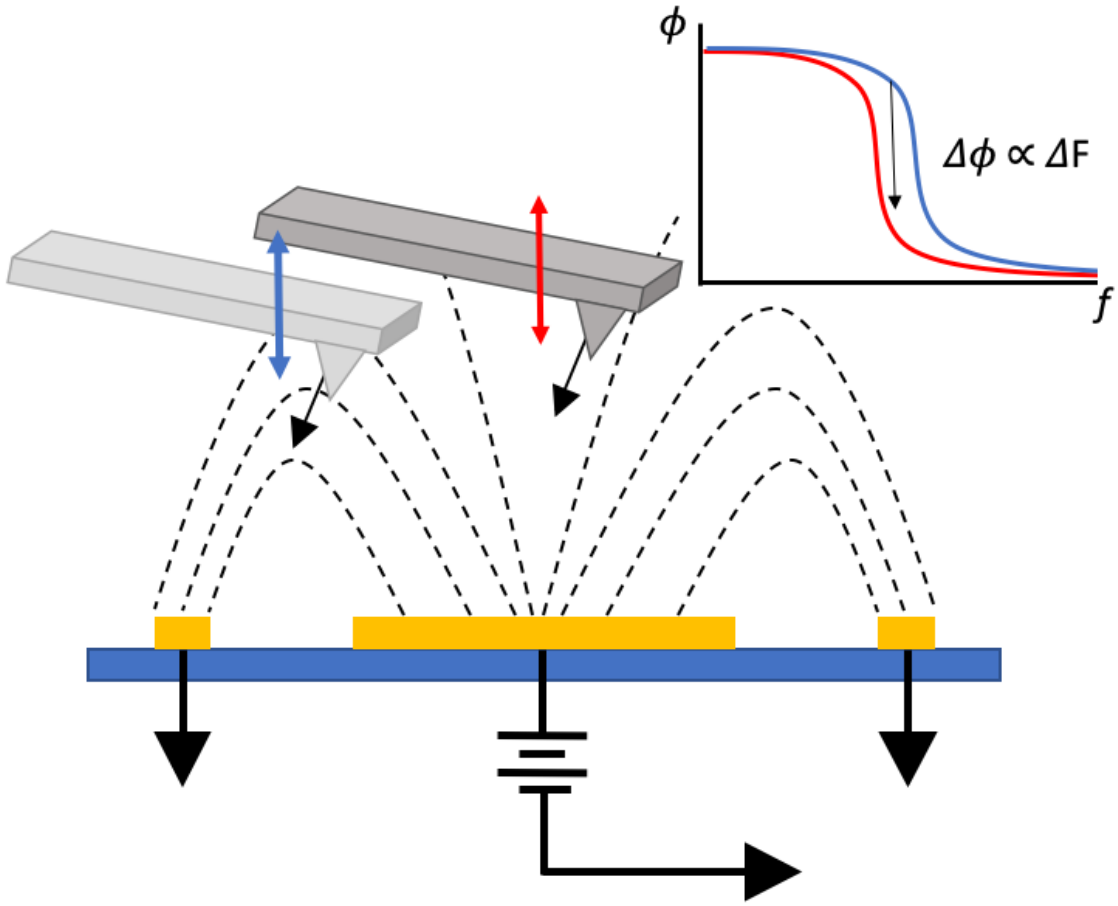

FIGURE 3.1. Electric Force Microscopy.
An illustration of Electric Force Microscopy, or EFM, which is a technique to spatially resolve the electric field gradient in three dimensions with nanometer-scale resolution. The electric field at the tip of an EFM probe due to the surface electrodes modulates the capacitive spring constant of the EFM cantilever, which then shifts the cantilever frequency and phase. The resulting change in the phase (inset), $\Delta\phi$, is proportional to the electric field gradient, $\Delta\phi \propto \Delta F$.

shapes. We can, however, gain some valuable insight on the electrostatic effects we measure with EFM from a simple model.

We assume that the tip/sample interaction can be modeled as a parallel plate capacitor. The capacitance is thus given by:

$$C(x) = \frac{\epsilon A}{d_0 - x} \tag{3.7}$$

where d_0 is the equilibrium distance from tip to sample and A is the cross-sectional area of the tip. The electrostatic force is therefore given by,

$$F(x) = \frac{-dU(x)}{dx} = -\frac{1}{2}V^2\frac{dC(x)}{dx} = -\frac{1}{2}V^2\frac{\epsilon A}{(d_0 - x)^2}. \tag{3.8}$$

Taylor expanding for small x gives,

$$F \approx -\frac{1}{2}V^2\frac{\epsilon A}{d_0^2} + V^2\frac{\epsilon A}{d_0^3}x + ... \tag{3.9}$$

from which we can extract the capacitive spring constant,

$$k_C = -V^2\frac{\epsilon A}{d_0^3} \tag{3.10}$$

The negative value of the capacitive spring constant softens the overall spring constant of the AFM cantilever, $k = k_e + k_C$, where k_e is the elastic spring constant of the cantilever. This softening decreases the measured frequency and red-shifts the corresponding amplitude and phase spectra. The resonance frequency in the presence of an electrostatic force can be written as,

$$\omega_0 = \sqrt{\frac{k_e + k_C}{m}} \approx \sqrt{\frac{k_e}{m}}\left[1 + \frac{1}{2}\frac{k_C}{k_e}\right] \approx \omega_e + \omega_C \tag{3.11}$$

where,

$$\omega_C = \frac{1}{2}\frac{k_C}{k_e}\omega_e \tag{3.12}$$

is the frequency shift due to the capacitive softening, assuming $k_e >> k_C$. Typically, k_e is several orders of magnitude greater than k. From Eq. 3.10, assuming a 100 nm radius plate and a 100 nm separation, $k_C \approx 0.0003$ N/m, whereas the spring constant for typical AFM cantilevers used in this study are in the range of 1-10 N/m.

The phase angle for a driven damped oscillator is given by,

$$\phi = \tan^{-1}\left[\frac{2\beta\omega}{\omega_0^2 - \omega^2}\right] = \tan^{-1}\left[\frac{2\beta\omega}{(\omega_e + \omega_C)^2 - \omega^2}\right] \tag{3.13}$$

To first order, the change in the phase due to a change in the capacitive spring constant is $\phi \approx \phi_0 + \frac{d\phi}{d\omega_C}\Delta\omega_C$ and therefore the phase shift of the cantilever $\Delta\phi \propto \Delta\omega_C \propto \Delta k_C$. If the frequency shift, $\Delta\omega_C$, is due to a change in the z position of the AFM tip, we would expect that,

$$\Delta\phi \propto \frac{1}{d_0^3}. \tag{3.14}$$

Eq. 3.10 also tells us that $k_C \propto A$, where A is the cross-sectional cantilever area. In an ideal experiment, A would remain constant so that shifts in the cantilever frequency could be solely attributed to variations in the electrostatic landscape. In practice, however, an AFM tip becomes increasingly dull over time due to damage caused by repeated scans across a sample surface, making it difficult to discern whether measured phase changes are due to variations in the electric force or the physical alteration of the tip. If $\Delta\omega_C$ was completely due to a change in AFM tip area, then

$$\Delta\phi \propto \Delta A(t) \tag{3.15}$$

and we would observe a constant phase offset due to blunting of the AFM probe over time. In our experiments, we are able to infer $A(t)$ and correct our data for tip dulling.

3.2.1. Electrostatic correlation to fluid behavior

A neural stimulation electrode typically operates in a fluid environment, however electrochemical AFM measurements and AFM measurements in fluid are difficult due to the impact of fluid drag forces on the oscillating AFM cantilever [92]. As demonstrated in Eq. 2.6, the voltage drop across the bulk electrolyte is proportional to DC amplitude of the applied signal. The voltage and electric fields generated in air by a capacitive electrode under an applied DC bias are proportional to those generated by an electrode in fluid with an applied AC bias. Therefore, we expect any enhancements in the field gradients based on electrode geometry and electrode surface area to map accordingly in the fluid environment.

3.3. Methods

To investigate the role that geometry plays in enhancing the electric field gradient penetration above the electrode surface, we chose a representative set of 6 Euclidean and fractal geometries, as shown in Fig. 3.2. The patterns were generated using a custom Matlab program such that each pattern has the same two-dimensional coverage area (i.e. would block the same fraction of light in a photodiode-based pixel). In addition, all geometries except the square have the same bounding area so that no one pattern extends closer to the outer ground wire than another, which may impact the measured force gradients. The line width of the electrode geometry (i.e. the width of the electrode traces) was used as the free

parameter to meet these constraints. Each condition was met within ∼0.2% error or less. Patterns generated by the Matlab code were subsequently output as CAD files for electron beam lithography or .STL files for finite element simulation in COMSOL.

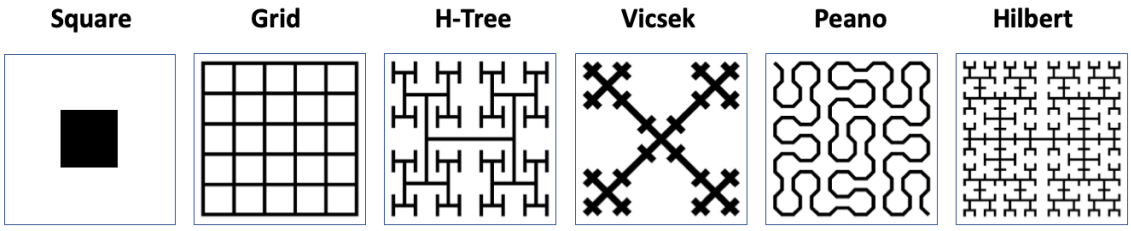

FIGURE 3.2. Electrode patterns for EFM.
In our EFM experiments, we tested the six electrode geometries shown here, including a square and grid, which we call "Euclidean", and H-tree, Vicsek, Peano, and Hilbert geometries, which are low-iteration fractals. The patterns shown here are derived from the CAD files used to both pattern the shapes using lithography and for finite-element simulations.

To create the electrode devices used in EFM measurements, we utilized a combination of optical and electron beam lithography. Contact pads and wires to each geometry were patterned onto a ∼2x2cm silicon chip in AZ-1512 positive photoresist using a 405nm laser in a Suss MicroTec Direct Write Laser Lithography system. Samples were then metallized with 5-10nm of electron beam evaporated Ti as an adhesive layer, and then 40nm of thermally evaporated Au in an Angstrom Engineering Amod Evaporator. Each "pixel" was 50x50μm in total area, surrounded by a 2μm wide outer ground wire. The resolution of direct-write optical lithography (∼1μm) is insufficient for patterning complex electrode geometries with line widths below 1μm as was needed for this study. The patterned electrode structures were aligned to pre-existing Ti/Au contact pads and wires and patterned into PMMA A4 photoresist using electron beam lithography in a Zeiss SEM. A second identical metallization lift-off step in Remover PG completed the

devices. Figure 3.3 shows representative optical images of the finished electrode structures. The silicon chip, each containing two full sets of 6 different electrode geometries, was mounted in the center of a custom printed circuit board from OshPark (Portland, OR). The PCB had ENIG gold pads for wire-bonding to the gold on the device, and soldering pins for simplified and secure electrical connections. Three gold wire bonds were used to attach each electrode contact pad from the Si chip to the underlying PCB. Pins were soldered to contact pads on the edges of the PCB for easy electrical access far from the active electrode/AFM scanning area. Electrical contact along each path was verified prior to all data collection. The final device set up is shown in Fig. 3.4.

3.3.1. Data Collection

In order to avoid variations in manufacturing from tip to tip, the same conductive AFM tip (SCM-PIT-V2, Bruker Nano) was mounted once and used to collect all of the phase data from each pattern on the sample over a period of 3 days. At the start of each scan, the AFM laser and photodetector were aligned carefully to the tip and the cantilever was tuned to a 10% offset below the resonance frequency at a distance of 1mm above the sample surface. The quality factor and resonance frequency was recorded for each tune. The cantilever phase was zeroed at the 10% offset on the resonance curve. An EFM scan was taken of each pattern at a 0V applied bias and a lift height of 250nm in order to calibrate the phase due to tip-sample interactions. A 4V bias was then applied to the central pattern, while the outer ground wire and conductive tip were attached to the global AFM ground pin. Scans were collected at lift heights of 250, 500, 750, 1000, and 1250nm above the surface with the applied bias. Lift-mode AFM necessarily

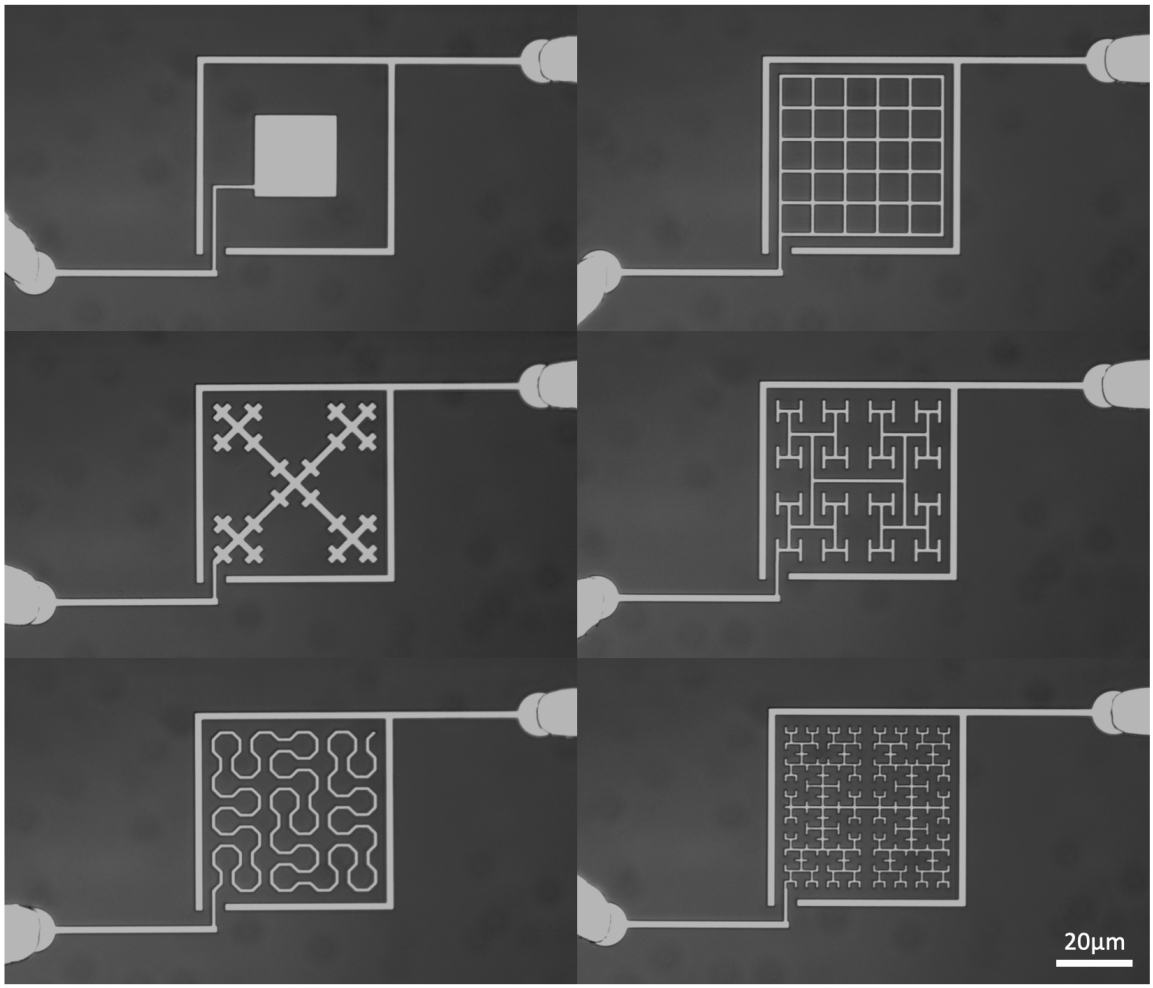

FIGURE 3.3. Electrodes patterned with ebeam lithography
Scanning electron microscopy images of all six patterned electrodes. The electrodes are composed of 40 nm of gold on 10 nm of titanium, all on a silicon/silicon oxide substrate. The electrodes were made by optical and electron-beam lithography.

involves a topographic scan of each line before a phase measurement is collected above the sample surface. Typical scans were 55x22.5μm and 64x128 samples, with the exception of the Peano, which was 55x55μm with 128x128 samples. Due to the large number of topographic scans collected during the experiment, we were concerned that tip-dulling (i.e. an increase in tip area over time) may skew the phase data. Because of this, the square geometry was scanned two times as a control - once at the very beginning of the experiment and once at the end.

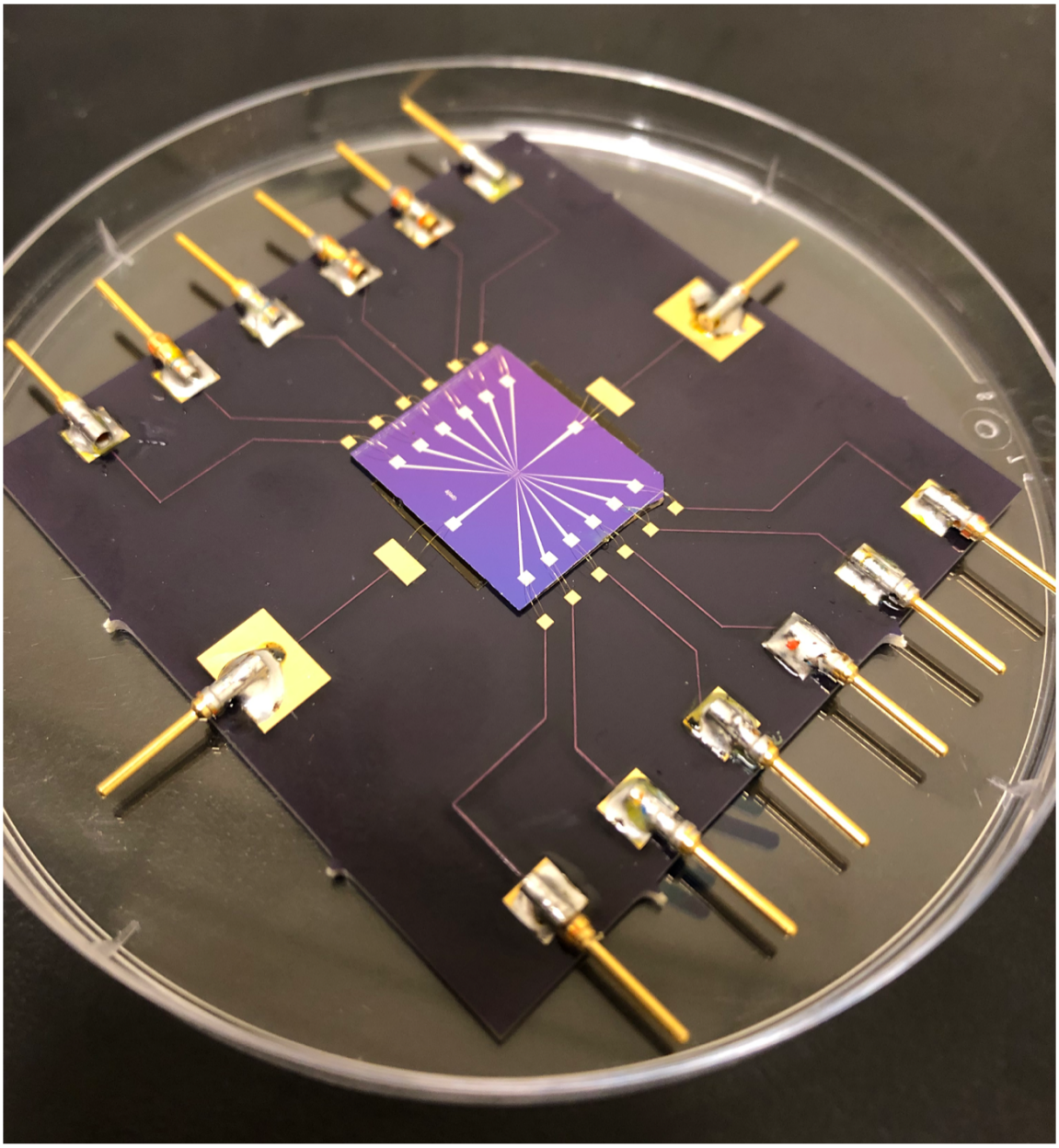

FIGURE 3.4. The Final EFM Device on a PCB.
The final device was mounted on a printed circuit board (PCB) for EFM measurements. The PCB was custom designed and outsourced for production. The PCB has ENIG gold pads for wire-bonding to the gold on the device, and soldering pins for simplified and secure electrical connections.

3.3.2. Data Analysis

Large area AFM scans must be done slowly and carefully to mitigate tip wear. In order to decrease overall scan time, data was collected and analyzed from

one quarter of each pattern, with the exception of the Peano curve which is not symmetric about its center. The same corner of each pattern was analyzed, as outlined in Fig. 3.5. This particular corner was chosen to minimize any adverse electrical affects on the cantilever from the wires connecting each pattern to the applied bias and ground. Each scan was XY plane-fit to remove any linear phase offsets due to stray fields from outer electrodes or sample drift. The average phase measured at a 250nm lift height and 0V applied bias for each geometry was subtracted from the average phase at each lift height with an applied DC bias to isolate the phase shift due to the electrostatic interactions. All of the patterns scanned were located on the same side of the sample. During the experiment, the wire bond to the Hilbert curve broke. After the second scan of the square geometry, the sample was rotated and the cantilever was moved to the opposite side of the chip with another set of identical electrodes to scan the Hilbert. Unfortunately the electrostatic landscape in this set up is not identical due to the orientation of the cantilever with respect to the patterned gold wires, therefore we omitted the Hilbert curve phase data from the experimental results.

3.3.3. Finite Element Simulations in COMSOL

In order to support the experimental data collected on the AFM, finite element simulations of identical geometries were conducted in COMSOL Multiphysics. The patterns generated in Matlab were output as .STL files and imported into COMSOL. Two key variations between the EFM set-up and the simulations were that the electrode height in COMSOL was set to zero (i.e. 2D electrodes) and there was no break in the outer ground wire for electrical access to the pattern in the center. When electrode height was set to ∼50nm to match

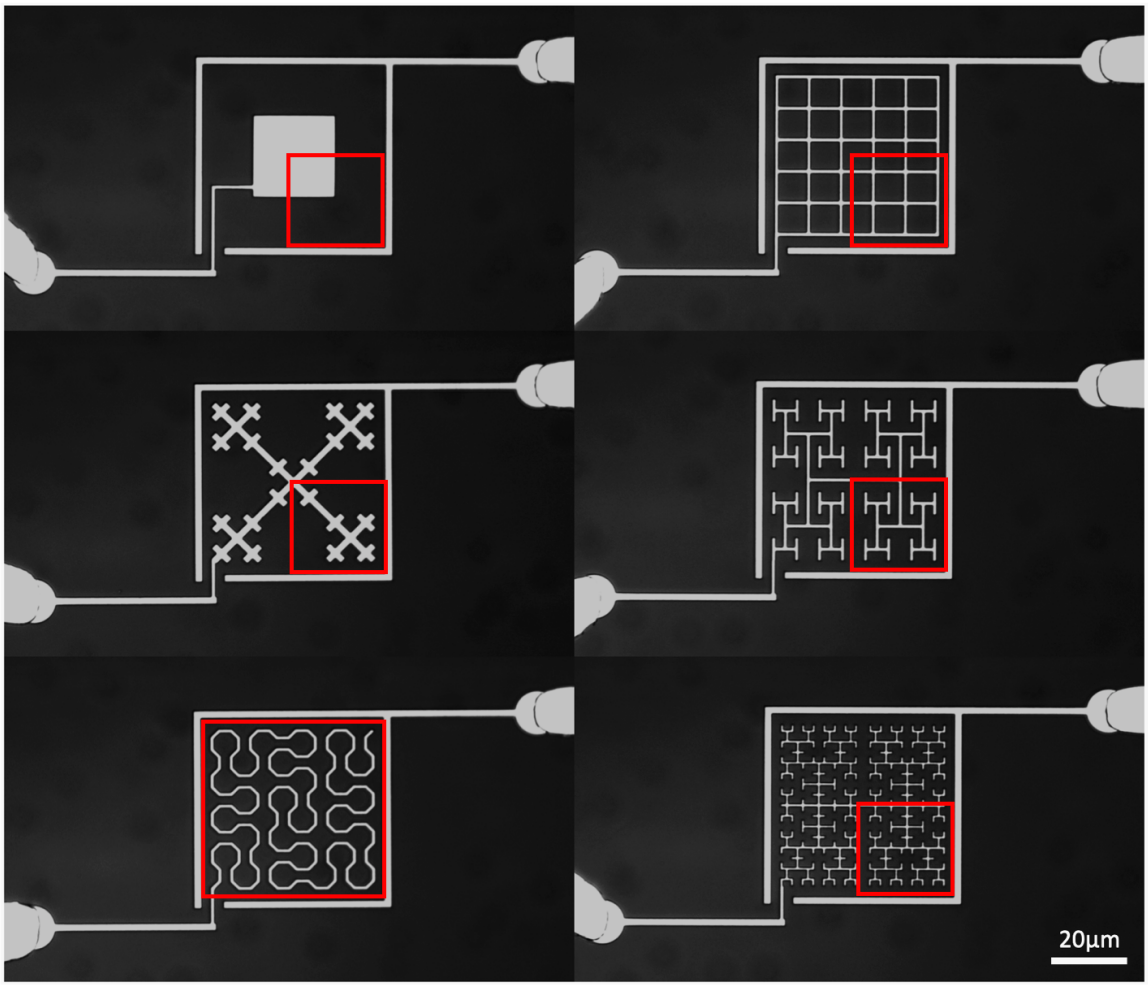

FIGURE 3.5. Scan Areas for EFM measurements.
The scan areas used in EFM measurements are outlined in red. Except for the Peano, we only imaged one-quarter of the electrode because of the rotational symmetry. Running EFM scans of the full geometry can take over a day, so reducing the scan time made the measurement more practical and also minimized tip wear.

experimental conditions, the mesh used in the simulation became unreliable and computationally intensive. Estimating second derivatives from numerical solutions can lead to errors [63], so particular care was taken when constructing the mesh. The same mesh sizes were used for each geometry, with the minimum element size set to 50 nm inside the electrode region. A triangular mesh on the surface was

swept vertically and a swept mesh with ∼60 nm sections in the region of interest was used. Because the electrode height was set to zero, the simulation isolates the effect of changing the perimeter of each geometry rather than surface area as a whole (since SA is fixed). The simulation calculated the average gradient of the electric field in the z-direction by taking a partial numerical derivative of the z component of the electric field.

3.4. Results

3.4.1. EFM Measurements

Two examples of full electrode scans, for the square and the Peano curve, can be seen in Fig. 3.6. As shown, our EFM technique provides a comprehensive mapping of the phase due to the electrostatic force gradient. This allows us to discern spatial information about the electric field gradient in the x and y dimensions at different s heights above the surface. These mappings demonstrate the ability of patterned electrode geometries, like the Peano, to spread the field gradient over a greater area within each confined pixel while maintaining signal magnitude. The As the cantilever is raised above the sample surface, the phase response due to the electrostatic force between the tip and sample decreases. This can be seen as a decrease in phase contrast of the patterns as z increases, which qualitatively aligns with the prediction of Eq. 3.14. In addition, the scans in Fig. 3.6 show the ability of a patterned geometry to maintain that phase contrast at greater distances from the sample surface than a standard square electrode geometry, as evidenced by the scans of each at 1250nm.

Fig. 3.7 contains the raw phase data analyzed for each pattern. As shown, we scanned one quarter of each symmetric pattern to help mitigate the scan time

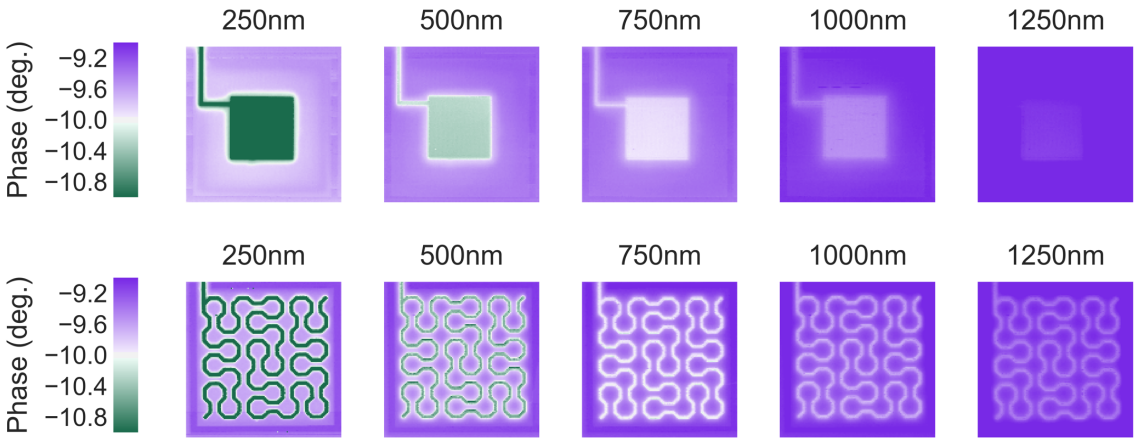

FIGURE 3.6. Full EFM Scans of the Square and Peano Geometries. Full EFM scans of the square and Peano geometries at 250, 500, 750, 1000, and 1250nm lift heights heights. The phase difference varies spatially in the plane, and also varies with lift height as can be seen visually from the decreasing phase contrast.

and tip damage. These scans allow us to visualize how the electric force gradient changes in different regions of the pixel. The phase shift is most negative in regions directly above the gold patterned traces, and most positive towards the outer ground. The electric field lines switch direction as they extend out of the inner biased electrode and then curve towards the outer ground, therefore we expect the force gradient to change direction in the background region between the two electrode surfaces. As shown, the cantilever phase softens and stiffens accordingly.

Since the cantilever phase was zeroed at 1mm above the sample surface, the measured phase close to the sample surface due to tip-sample interactions will be non-zero without an applied bias. To account for these interactions, we measured the phase at an applied DC bias of 0V and a lift height of 250nm, as shown in Fig. 3.8. The background phase we measure is likely due to static charge, photoinduced charge, dipole interactions, or van der waals forces. We used this phase data to offset the phase measurements in Fig.3.7 and to therefore isolate the electrostatic

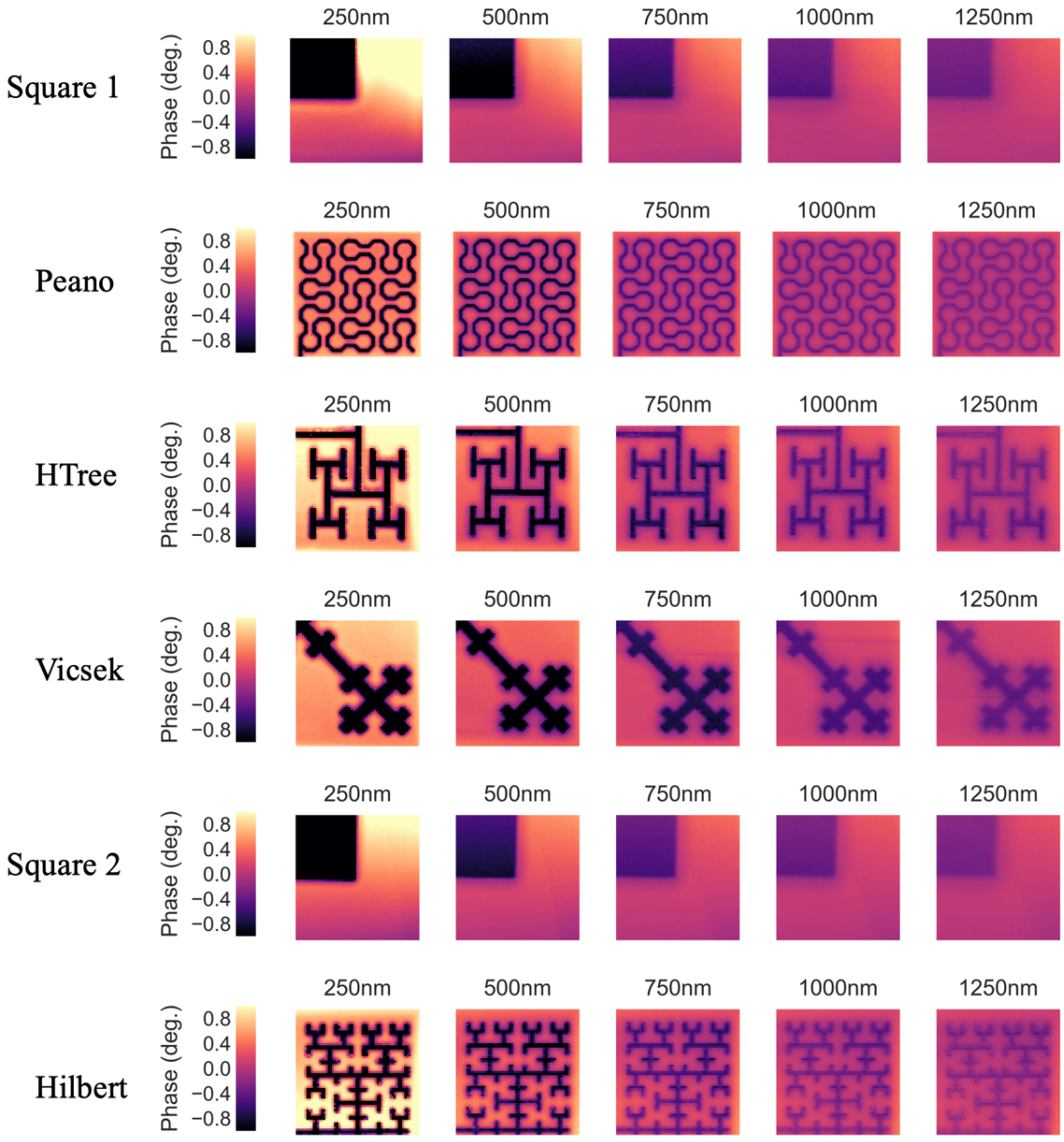

FIGURE 3.7. Scan regions analyzed for all geometries.
For each geometry, with the exception of the Peano, we collected phase data from one quarter of each pattern. The raw phase data for each can be seen here. They are listed column-wise in order of scan - Square 1, Peano, HTree, Vicsek, Square 2, Hilbert.

interactions due to the tip-sample capacitance. As shown, these 0V phase shifts are an order of magnitude smaller than the shifts measured with an applied bias.

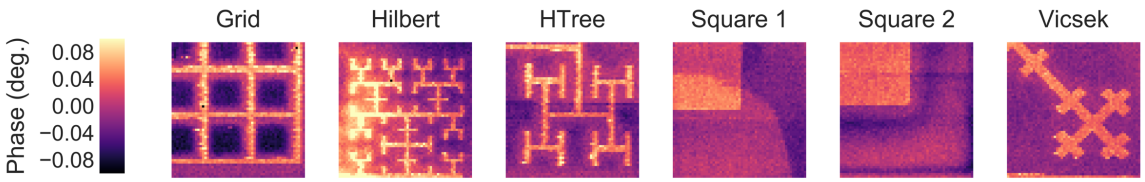

FIGURE 3.8. Phase scans at 0V bias and 250nm height.
We measured the phase at a 0V applied bias and a lift height of 250nm to quantify the shift due to tip-sample interactions. The average phase at 0V and 250nm was used to offset the average phase for each lift height at 4V applied bias.

The average phase shift for each geometry, offset by the 0V average phase at 250nm can be seen in Fig. 3.9. The legend contains each geometry listed in chronological order of the scan. Square 1 was the first geometry scanned, followed by the Peano, HTree, grid, Vicsek, and the square again (square 2). Square 1 exhibits the lowest measured phase shift at every lift height. Each subsequent geometry displayed larger average phase shifts, including the second scan of the square geometry collected last.

Fig 3.10 contains a simplified plot of square 2 (in brown), which was a re-scan of square 1 (in blue) after scanning all other geometries. The offset of the second scan from the first scan confirmed our suspicion that tip-dulling contributes to the measured phase shift of the cantilever in time. If the measured phase shift were solely due to the electrostatic force between the tip and sample, subsequent scans of the same geometry should be identical regardless of when they are collected.

The frequency shift of the cantilever due to tip dulling can be written as,

$$\omega_0(t) = \omega_0 - c \cdot \Delta A(t) \tag{3.16}$$

where c is some constant of proportionality and,

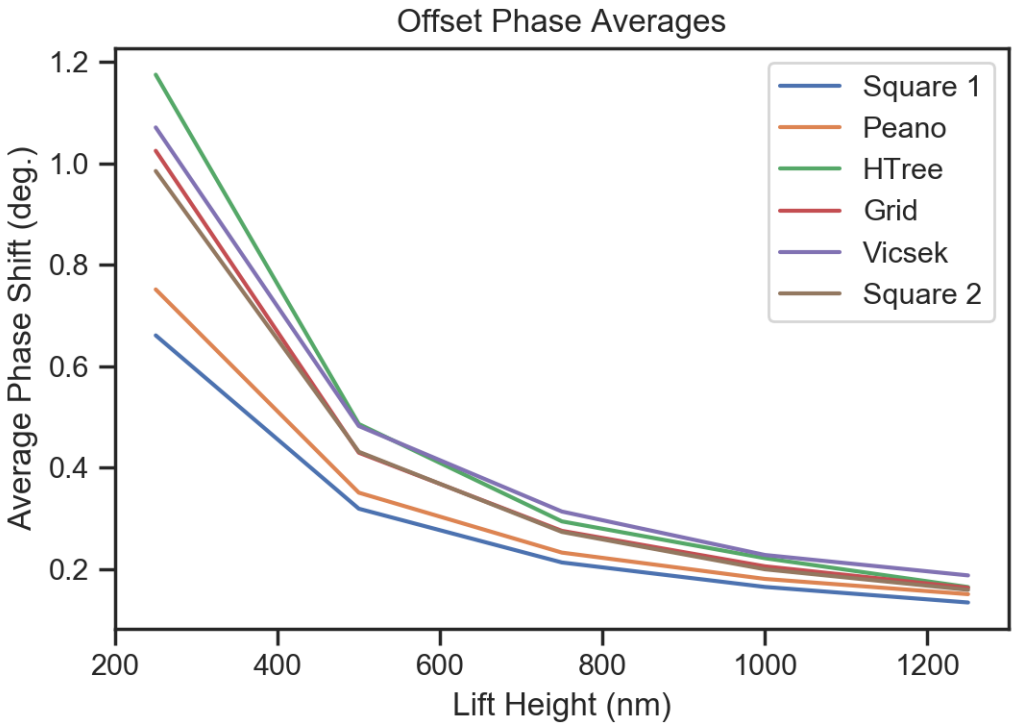

FIGURE 3.9. Average phase shift for all geometries.
The average phase shift relative to the 0V background offset as a function of lift height for all geometries. The square geometry was imaged twice to measure the tip dulling effect.

$$\Delta A(t) = A_0 + b \cdot t \tag{3.17}$$

represents the growing AFM tip area in time. As outlined in the model of section 3.1, the phase shift of the cantilever, to first order, is linearly proportional to the frequency shift and therefore linearly proportional to the changing tip area. This assumption allows us to map the measured average phases of square 2 onto square 1 and obtain a linear translation for each average phase data point for the other geometries based on the scan order. The results of this linear mapping can be seen in Fig. 3.11. The normalized phase shifts yield our best estimate for the ordering of the geometries based on the average phase shift. As shown, the square still exhibits

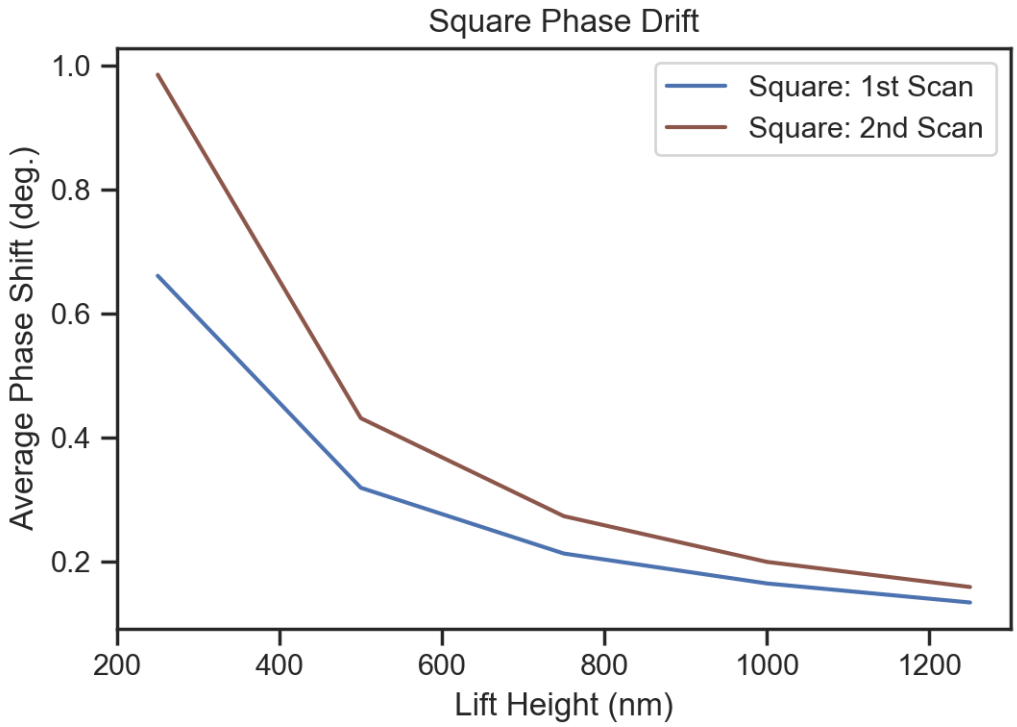

FIGURE 3.10. Phase drift due to tip-dulling.
The average phase vs. lift height for the square geometry for two different scans, one taken at the beginning of the EFM experiments, and one taken just before measuring the last geometry (Hilbert). The difference in the scans is consistent with wear-and-tear dulling of the EFM probe tip, which will increase the effective area of the probe. The difference between these two scans is used to infer the tip area vs. time, $A(t) = A_0 + b \cdot t$, which provides a means to normalize the scans and order the scans.

the lowest average phase shift at all lift heights. The Peano closely follows the square. The Vicsek and grid are very similar close to the surface, but the Vicsek appears to win out with increasing distance from the sample surface. The Htree displays the highest average phase shift and outperforms all of the geometries close to the surface, however behaves very similarly to the others at larger z heights.

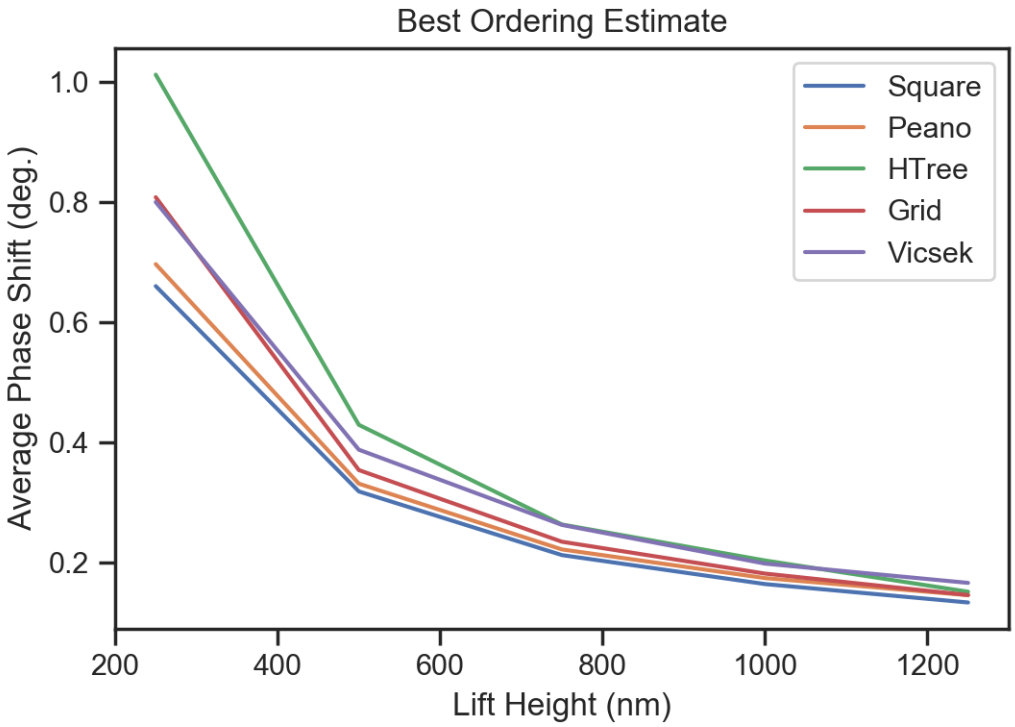

FIGURE 3.11. Best estimate of phase ordering.
The average phase vs. lift height for the tip-dulling normalized data. According to the data, the Htree has the largest average phase shift close to the electrode surface. The Htree outperforms the other geometries for most lift height values, but the relative difference in the effect decreases farther from the surface.

3.4.2. Finite Element Simulations in COMSOL

The result of our finite element simulations can be seen in Fig. 3.12. The square is clearly the least effective electrode geometry in terms of maximizing the field gradient above the surface, closely followed by the Vicsek. The Htree, Peano, and grid all behave very similarly. The Hilbert curve outperforms the other geometries closest to the sample surface but drops off with steeper slope. The ordering of the geometries interestingly correlates quite well to perimeter length, listed in Table 3.1. The square has the lowest overall perimeter, followed by the Vicsek. The grid, Peano, and HTree show very similar qualitative behavior and

have the smallest deviation in overall perimeter. The Hilbert has a significantly higher overall perimeter length than the other geometries.

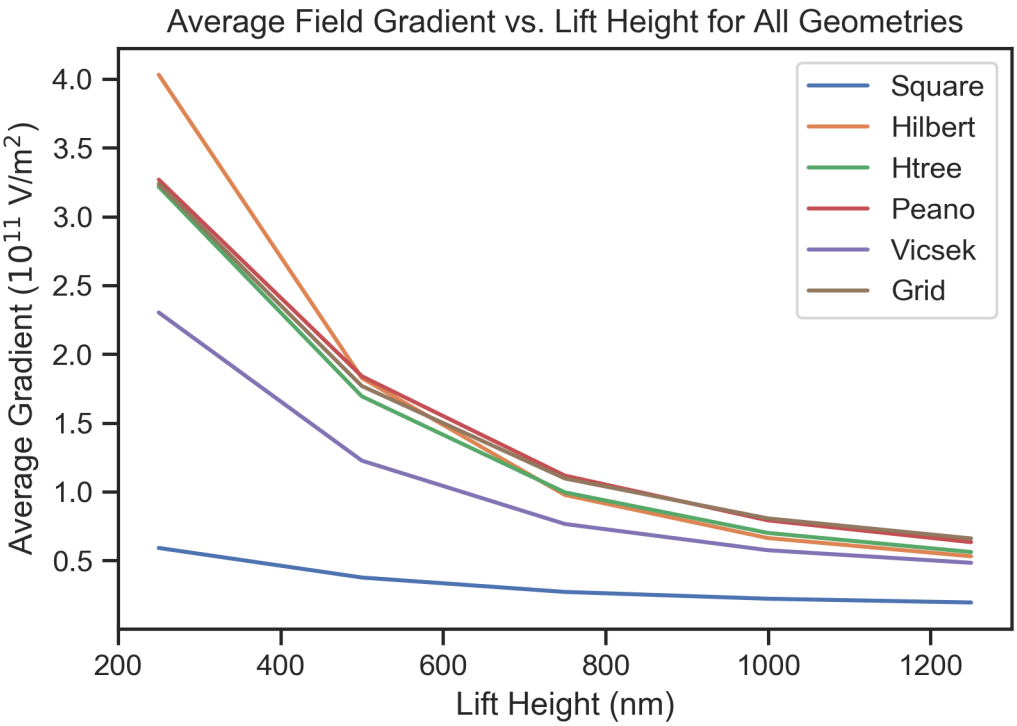

FIGURE 3.12. FEM Simulations.
The average electric field gradient vs. lift height obtained from finite-element simulations.

3.5. Discussion

We used electric force microscopy to measure the electric force gradient penetration above the surface of 5 different geometries of varying complexity. When compared to a simple Euclidean geometry, like a square, all of the patterned geometries demonstrated an increased ability to spread out the field gradient spatially in the XY plane. Since the electric field gradient is directly proportional to the activating function, patterned geometries maximize the AF in more regions of a given pixel while the AF generated by a square geometry is confined to

Geometry	Total Perimeter Length (μm)	Boundary Perimeter Length (μm)
Square	89.2	N/A
Vicsek	530.8	0
Grid	794.2	178
Peano	968.9	58.2
HTree	996.0	66.3
Hilbert	1477.8	65.3

TABLE 3.1. Total perimeter length and boundary perimeter length for all six electrode geometries.

the center of the pixel. Given the correlation between the AF and probability of stimulation, it is likely that this spatial spread of the AF will result in more efficacious neural stimulation simply because it does not require a target neuron to be centered exactly above the center of the pixel. Furthermore, our EFM technique is unique in that it allows us to map this spatial behavior directly so that we are able to visualize regions of large field gradients in a given pixel.

The measured field gradient penetration above the electrode surface for all patterned geometries was larger than for a square geometry of the same surface area, even when the effect of AFM tip-dulling in time was accounted for. The effect is most pronounced close to the electrode surface and becomes less prominent with distance. The shape of the drop off with distance d_0 is similar to what we'd expect from our simple model, although not as steep as would be predicted by the $1/d_0^3$ relationship in Eq. 3.14, suggesting a breakdown of the simple parallel-plate model. An electrostatic model that uses two parallel wires, which also better captures the geometry of the electrode traces, would predict a softer dependence on d_0 closer to what we observe. Of the geometries measured with EFM, the Htree has the largest phase shift and therefore largest field gradient and AF closest to the surface. Therefore, it is expected that Htree electrodes would be the best candidate for

increasing the likelihood of neural stimulation when compared to the other fractal and Euclidean geometries presented here.

The simulation data shows a similar trend to the experimental data, however slight differences between the simulation and experimental measurement result in a few noticeable deviations. Notably, the simulation data appears to be directly correlated to the perimeter of the geometry, with the Hilbert outperforming all other geometries. The Vicsek, which is the most "square-like" geometry - i.e. has a larger line width and shorter perimeter length - severely under-performs when compared to the other patterned geometries. The Htree, Peano, and grid all have similar perimeter lengths, and as such demonstrate very similar trends in their simulated average electric field gradients. The results of the simulation indicate that maximizing perimeter length for a given electrode surface area may be an effective way to maximize the likelihood of neural stimulation above the electrode surface.

In the experimental data, the measured average phase shift for the Peano is significantly lower than what we would expect from the simulation and the perimeter length. The Peano, as mentioned above, is not symmetric about its center and we could not use the same reduced scan area to obtain the average phase shift. Because of this, the electrostatic landscape of the full scan may have had an unintended impact on the overall measured average phase due to the sensitivity of the measurement. Specifically, the AFM cantilever hovered over the ground wire and ground connection to a much greater extent during the top half of the full pattern scan. Since the AFM tip is also grounded, this likely reduced the measured phase shifts from the biased pattern in this region, resulting in an overall reduction in average measured phase. The sensitivity of

AFM measurements, very large scan regions, and complex variations in the global electrostatic landscape that impact the behavior of a conductive AFM tip are the likely cause of slight deviations seen between the simulation and experiment. A more effective comparison would involve simulating the exact experimental set-up, including all connections to ground and the bias voltage, or eliminating those connections from the experimental set-up. This could be done using a heavily doped silicon substrate and backside contacts to the electrodes, eliminating the need for on-chip wires.

We were curious whether or not the boundary perimeter length - defined as the perimeter of each geometry that lies along a box bounding the entire geometry - could shed light on certain discrepancies in the data. If a larger amount of an electrode geometry extends closer to the outer ground wire, we'd expect greater variations in the electric field profile since the distance over which those variations occur is much shorter, analogous to how decreasing the distance between the plates of a capacitor at fixed bias will increase the electric field. As shown in the last column of Table 3.1, the grid has a significantly larger boundary perimeter length than all of the other geometries. This may offer some insight as to why the grid performs similarly to other patterned geometries in both the simulation and experimental data, despite having a lower total perimeter length. It is likely that the ordering we see here is a convolution of both of these effects.

While it is difficult to discern which patterned geometry is "the best", we can conclude that patterned geometries do a better job at maximizing the AF compared to square geometries with the same surface area. The simulation results reveal this enhancement may be correlated with perimeter length, a claim which is also supported by the experimental data despite differences between the two

approaches. This correlation would suggest that to increase the activating function, one should maximize the perimeter length of the electrode. From our study, fractal geometries like the Htree and Hilbert outperform the other geometries, a result that is expected for fractals, since they maximize perimeter length per unit area.

3.6. Conclusion

Our EFM technique provides us with a unique and useful way to visualize how patterned geometries maximize the neural activating function (AF) in the space above a pixel. Since the phase we measure with EFM is proportional to the AF, our work provides the first direct means to image the AF in three dimensions with nanometer-scale spatial resolution, and therefore establishes EFM as a critical tool for future efforts for the rational design of neural electrodes. Our data shows that patterned electrode geometries spread out and maximize the AF to a greater extent, therefore increasing the efficiency of neural stimulation for a fixed coverage area within a photovoltaic retinal implant pixel. Utilizing patterned geometries with high perimeter values in lieu of standard square or circle electrodes may therefore reduce the number of photodiodes needed to power a retinal implant pixel.

CHAPTER IV

CARBON NANOTUBES: A MATERIAL FOR HIGH SURFACE AREA NEURAL ELECTRODES

4.1. Introduction

In the previous chapter, I showed that microscale patterning of electrodes can enhance the electric field gradient penetration above the electrode surface and therefore increase the likelihood of neural stimulation. This means of surface area enhancement is just one way to improve stimulation. It becomes a more powerful approach, however, when it can be combined with a high surface area electrode material that behaves favorably in an electrochemical environment. In this chapter, we investigate vertically aligned carbon nanotubes (VACNTs) as an electrode material and demonstrate biocompatibility through a series of *in vitro* cell culture experiments.

Electrode materials with high surface roughness or high porosity are ideal candidates for neural interfaces because their electrochemical surface area (ESA) greatly exceeds their geometric surface area (GSA), thereby increasing the area available for charge storage for a given electrode footprint [27]. In addition to favorable electrochemical properties, materials for neural interfaces must be biocompatible while meeting a demanding set of chemical and mechanical requirements. Chemically, electrode materials must resist degradation in the physiological environment of neural tissue and should support surface functionalization to increase their hydrophilicity, thereby preventing neuronal cell death and stimulating neurite outgrowth [93]. Mechanically, they need to be

strong and yet flexible to reduce inflammation in the surrounding tissue [94][95]. Furthermore, soft materials (i.e., mechanically compliant) [96][97] and materials with rough, textured surfaces [98][99] can enhance neurite outgrowth, elongation rate, and branching.

The typical foreign-body response to electrode arrays implanted in the CNS is characterized by scar tissue encapsulation of the device, wherein reactive glial cells surround the implant in a layered structure that can be tens to hundreds of microns thick [100]. This process, called gliosis, threatens the efficacy of stimulation by causing a large physical separation between the electrodes and target tissue, and by increasing overall tissue impedance. Because they play a critical role in both retinal health and function [34] and in the immune response to foreign objects like retinal implants, an analysis of electrode material biocompatibility must include glial cell behavior. Retinal neurons and glial cells can be co-cultured in a single step with relative ease, therefore *in vitro* primary cell cultures offer a highly controllable way to assess how both cell types respond to potential new electrode materials. Interestingly, materials with rough, textured surfaces have been shown to mitigate glial cell proliferation *in vitro* [101]. In addition, textured surface patterning can be used to obtain a separation of retinal neurons and glia in distinct but neighboring regions on a substrate [102] and to control astrocyte adhesion [103]. An electrode material that supports neuron growth and adhesion while mitigating the glial inflammatory response, therefore, is ideal for retinal implant applications.

Carbon nanotubes (CNTs) are an electrode material that simultaneously meets many of the requirements for neural prostheses. CNTs are electrically conductive and have a specific capacitance of $\approx$10 mF/cm^2 that compares favorably to nearly every other material [76]. CNTs can be chemically functionalized to

improve neurite outgrowth and branching [104][105]. They are mechanically flexible [106] yet incredibly strong [107], and their molecular-scale diameter (∼1–10 nm) promotes strong adhesion and electrical coupling with neurons [108][109]. Vertically aligned carbon nanotubes (VACNTs) can be patterned and synthesized by chemical vapor deposition (CVD) to form high-aspect-ratio structures with heights exceeding 500μm [110], and because neurons adhere strongly to CNTs, patterned CNTs can be used as scaffolds to guide neurite growth [111]. Importantly, the biocompatibility of VACNTs has been examined *in vitro* with several types of neural tissue, including rat hippocampal and cortical neurons, the NOBEC cell line (glial cells), and retinal precursor cells [110][111][112][113][114]. Due to this combination of useful properties, CNTs have been employed in multi-electrode arrays (MEAs) for epiretinal implants and *in vitro* MEA studies where CNTs improved the signal-to-noise ratio, lowered the stimulation threshold, and minimized glial scarring [115][116].

Despite many promising advances, CNTs have not been widely adopted in neural electrodes, partly because of the structural fragility of CNT films. This fragility is largely caused by poor CNT/substrate adhesion. In the CVD growth of VACNTs where the catalyst (i.e., Fe or nickel (Ni)) is deposited directly onto the substrate, the nanotube films often delaminate and crack [115][116], preventing them from acting as conducting electrodes. Moreover, delamination of CNTs increases the concentration of CNTs dispersed in the culture medium, which can reduce axonal regeneration [117]. A simple approach to strengthen the VACNT/substrate bond is to deposit a thin film of Al between the substrate and the catalyst [118]. While the Al underlayer does greatly reduce cracking and delamination, the neurotoxicity of Al raises the vital and previously unresolved

question about the biocompatibility of the Al-stabilized VACNTs. To test this biocompatibility, we seeded dissociated retinal neurons onto patterned VACNT substrates for several days *in vitro* (DIV).

We measured the extent of neurite outgrowth to infer biocompatibility, as it is well established that neurite outgrowth and cell viability are correlated [119]. Furthermore, we analyzed the distribution of glial cells on substrates patterned with alternating VACNT-SiO_2 rows to determine whether VACNTs suppress the glial inflammatory response *in vitro*. We found that VACNT substrates displayed excellent neurite outgrowth at multiple culture durations up to 17 DIV. In addition, glial cells were found in much higher numbers in between successive rows of patterned VACNTs for multiple gap widths and culture durations, indicating that VACNTs suppress glia proliferation. Our results demonstrate that VACNTs prepared with an Al underlayer are viable electrode candidates for retinal implants.

4.2. Methods

The samples used for this study consisted of 6×6mm patterns of alternating rows of VACNTs and SiO_2 in the center of 1×1cm Si substrates. The VACNT row width was fixed at ∼100μm with SiO_2 gaps of ∼50μm, ∼75μm, and ∼100μm. To assess the need for an Al underlayer, we also qualitatively compared neurite outgrowth and CNT film integrity on non-patterned VACNT "forests". Mats of VACNTs were grown, with and without an Al underlayer, across the entire surface of 1×1cm silicon chips and placed in culture for 3 DIV.

4.2.1. Sample Fabrication & Characterization

Standard optical and direct-write laser lithography processes were used to fabricate the VACNT row samples in this work. Briefly, (100) Si wafers with 300nm of SiO_2 were cleaned with solvents, dehydrated on a 400°C hot plate for 15 minutes, and vapor-coated with hexamethyldisilazane (HMDS) for 20 minutes to promote photoresist adhesion. AZ-1512 positive resist (MicroChemicals GmbH) was spun on at 4000rpm and soft-baked for 2.5 minutes at 105°C to drive out resist solvents. Sample patterns were generated either by UV exposure in a mask aligner using printed transparency masks or via designs generated in CleWin 5 CAD software and transferred to the substrate with a 405nm laser using a dose of 220mJ/cm^2. A post-exposure bake was done for 60s at 105°C and samples were subsequently developed in AZ 300 MIF (1-3% TMAH) developer for 60s. Samples were then hard-baked for 2 min at 105°C to prevent outgassing in the subsequent metallization step.

Samples were mounted in an Amod electron beam evaporator (Oxford Instruments). A 3nm layer of Al (for patterned and Al/Fe forests), which immediately oxidizes to form an alumina adhesive layer, was thermally evaporated onto the substrate surface and then a 6nm layer of Fe was evaporated using the electron beam. Lift-off of photoresist was done in acetone with sonication for 10 minutes. Patterned and metallized samples were placed carefully into a a 2" quartz tube furnace and slowly heated at atmospheric pressure. When the furnace reached 650°C, a 2:1 mixture of ethylene (C_2H_4) and hydrogen (H_2) at 200 and 100 SCCM, respectively, in the presence of 600 SCCM flow of argon (Ar), was injected for 3 minutes. Patterned samples contained VACNT rows with heights ranging from 20-30μm.

Characterization of VACNT samples was conducted using scanning electron microscopy (SEM) and transmission electron microscopy (TEM). Visual characterization of the VACNT structure, topography, and height was carried out using a Zeiss Ultra-55 SEM. TEM imaging of the nanotubes was performed with a FEI Tecnai operated at 80 keV.

4.2.2. Dissociated Retinal Cell Culture

All *in vitro* studies were performed under the approval of the University of Oregon Institutional Animal Care and Use Committees under protocol 16-04, in compliance with National Institutes of Health guidelines for the care and use of experimental animals.

Retinal cells were obtained from wildtype C57BL/6 mice at postnatal day 4, as previously described [120][102]. Animals were first euthanized, and then whole retinas were dissected from the eyes and placed into Dulbecco's modified eagle medium (DMEM) with high-glucose, sodium pyruvate, and L-glutamine (Thermo Fisher Scientific). After dissection, 4 retinas were transferred to an enzyme solution and digested for 22.5 min at 37°C to loosen cell-cell adhesion. The enzyme solution was prepared by combining 3mL DMEM, 3mg papain (Worthington Biochemical Corporation), and 0.9μg L-cysteine (Sigma-Aldrich) and filtering through a 0.22μm filter (Sarstedt). After digestion, the enzyme solution was removed and the retinas were rinsed thoroughly in DMEM. Digested retinas were then placed into 2mL of the final culture medium. The final culture medium was prepared by mixing 21.34mL of DMEM, 440μL of B27 supplement (Sigma-Aldrich), and 220μL L-glutamine-penicillin-streptomycin (Sigma-Aldrich). The final culture medium plus digested retinas were then mechanically agitated through a rounded Pasteur pipette

to break the whole retinas into single cells and cell clusters. Next, 48mL of DMEM was added to the 2mL dissociated retina solution and centrifuged at $900g$ for 5 min. After centrifugation, the supernatant was removed and the remaining 20mL of final culture medium was added to the cell pellet. The cells were again mechanically agitated to re-suspend cells throughout the solution. The cell suspension was then passed through a 40μm cell strainer (Thermo Fisher Scientific) to remove large cell clumps. Finally, 500μL of cell suspension containing with and $\sim 1.7 \times 10^6$ (half for forest samples) cells was carefully plated directly onto a VACNT sample placed in the middle of each well of a 4-well culture plate (Sarstedt, each well 1.9 cm^2) and cultured for 3, 7, or 17 DIV at 37°C and 5% CO_2. Cell plating was randomized between the sample preparations. No chemical functionalization, such as precoating with extracellular matrix (ECM) proteins, was done to the VACNT samples prior to seeding the cells. Medium changes were first performed on the third day after culture and then every two days until culture termination.

4.2.3. Immunohistochemistry

Fluorescent labeling of neurons and glia was achieved through dual staining immunohistochemistry. First, the culture was terminated by fixing the cells with 4% paraformaldehyde (PFA) for 30 min. After fixation, PFA was rinsed with 1X phosphate buffered saline, pH 7.3 (PBS), and cells were pre-incubated in a PBScomp solution containing 2% donkey normal serum (DNS) and 2% goat normal serum (GNS) (Jackson ImmunoResearch) for 1 hour at room temperature. PBScomp was prepared from 1x PBS, 0.25% Triton-X (Sigma-Aldrich) and 1% bovine serum albumin (Sigma-Aldrich). The pre-incubation solution was then removed and the samples were incubated in the primary antibody solution

overnight at 4°C. The primary incubation solution contained PBScomp, 2% DNS, 2% GNS, 1:1500 rabbit anti-β-tubulin III (red neuronal marker) (Sigma-Aldrich), and 1:1500 goat anti-glial fibrillary acidic protein (GFAP, green glia marker) (Dako). The following day, the primary incubation solution was removed and samples were rinsed again in 1X PBS. They were then incubated in a secondary antibody solution containing PBScomp, 1:400 Alexa Fluor 488 donkey anti-rabbit IgG, and 1:200 Cy3 goat anti-mouse IgG (Jackson ImmunoResearch) for 45 min at room temperature. Afterwards, the secondary antibody solution was removed and samples were rinsed again. Finally, the samples were mounted to glass microscope slides with Vectashield containing DAPI (DAPI attaches to DNA in the cell nucleus and fluoresces blue) (Vector Labs).

4.2.4. Image Analysis

Uniform VACNT forest samples (with Fe and Al/Fe catalyst layers) were imaged using a Nikon Eclipse Ti-U epifluorescence optical microscope with an iXon Ultra 888 EMCCD camera at 20X magnification (Nikon CFI S Plan Fluor objective, NA 0.45). A total of 20 randomly chosen positions on each VACNT sample were imaged to statistically assess cell response on that sample. The field of view (FOV) of each image was 0.20mm^2. Patterned VACNT row samples were fully imaged at 20X magnification using a Leica DMi8 inverted fluorescence microscope. Each FOV was 0.44mm^2. Normalized neurite length was examined as the neuron response variable for the different VACNT preparations. To quantify neurite length, we developed an automated image analysis algorithm based on one previously reported [121]. The developed algorithm allowed us to measure the total neurite length in each FOV. For each sample, the normalized neurite length (N_{CNT}) was

calculated by dividing the total neurite length over all FOVs by the available VACNT area.

To analyze glial cell coverage on and off the VACNT surface, full sample fluorescence images were filtered using a standard Gaussian high pass filter to remove low frequency background variations. Anomalous sample regions (i.e. regions of missing CNTs, bubbles, etc.) were further masked from the analyzed data. The mean background intensity values in the SiO_2 and CNT regions of each individual sample were used to determine the proper threshold. Images were thresholded above integer multiples of the mean ranging anywhere from 3-15x the mean value based on individual sample behavior. SiO_2 and CNT regions were thresholded independently but visually inspected for morphological agreement. Pixel groupings less than 20 pix^2 were removed from each thresholded image. The normalized glial cell coverage was determined for each region by dividing the number of GFAP-positive (bright) pixels after thresholding by the overall pixel area of each region. The parameters used were,

$$G_{\mathrm{Si}} = \frac{\#\text{ of bright pixels on } SiO_2}{\text{total } SiO_2 \text{ area}} \tag{4.1}$$

and

$$G_{\mathrm{CNT}} = \frac{\#\text{ of bright pixels on CNT}}{\text{total CNT area}} \tag{4.2}$$

4.2.5. Statistical Analysis

We tested via Kruskal–Wallis analysis with a post-hoc Dunn's test against the null hypothesis that the normalized neurite length was not dependent on VACNT preparation (for uniform forest samples) or culture duration (for patterned

samples). Neurite outgrowth was measured on 8 uniform samples per preparation (Fe and Al/Fe), tested across 3 independent 3 DIV cultures. Neurite outgrowth was measured on row samples with 100μm CNT rows and gaps, with 6 samples at 3 DIV and 11 at 7 DIV, tested across 9 independent cultures. To compare glial cell coverage between CNT and Si surfaces, we analyzed 28 samples spread across 5 independent cultures at both 7 and 17 DIV. The VACNT row width was fixed at $\sim$100μm and SiO_2 gaps between rows were $\sim$50μm (8 samples), $\sim$75μm (8 samples), and $\sim$100μm (12 samples). Full sample images were tested against the null hypothesis that there is no spatial correlation of glial cells on the sample. To do this, we bootstrapped each sample image 500 times by randomly swapping all of the pixels in space and reapplying our masks to separate the two specific regions. This created a distribution centered at a mean of 1, the condition where $G_{\mathrm{Si}} = G_{\mathrm{CNT}}$. P-values were calculated based on the $G_{\mathrm{Si}}/G_{\mathrm{CNT}}$ ratio for each sample.

4.3. Results

VACNT forest samples fabricated for the biocompatibility tests were densely packed as seen in Fig. 4.1a and there were no observable differences in VACNT nanotopography via SEM imaging between the Fe and Al/Fe preparations. Notably, VACNTs grown without the Al underlayer often delaminated from the substrate during pre-culture sample handling. Those samples were omitted from cell culture. However, delamination was also observed during culture, after culture and after immunohistochemistry procedures in samples prepared without the Al adhesive layer, even for those that appeared in tact at the start of the culture. Fig. 4.2 contains a representative post-culture fluorescence image of a sample prepared with only an Fe catalyst layer. The VACNT film has substantially delaminated

from the Si substrate, as demonstrated by the void in β-tubulin III and DAPI signal.

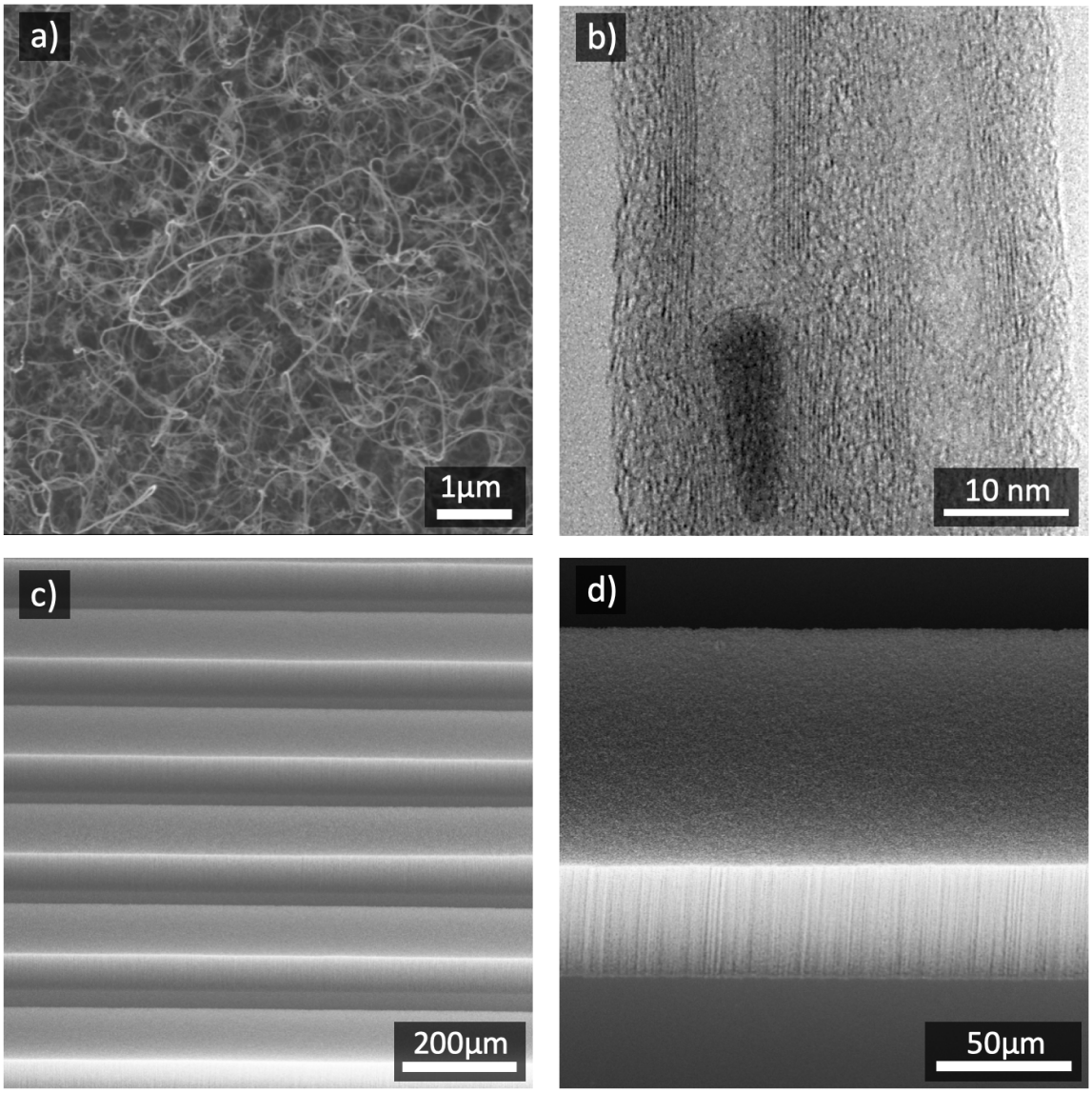

FIGURE 4.1. Vertically aligned carbon nanotubes for *in vitro* studies. a) An example of VACNT surface nanotopography. b) A TEM image showing an encapsulated Fe nanoparticle within a MWCNT. c) An example of a patterned VACNT row sample. d) A high resolution image showing the sidewall of each VACNT row.

High-resolution TEM characterization of the VACNTs revealed clear sidewalls and a hollow core, demonstrating that our fabrication process synthesized multi-

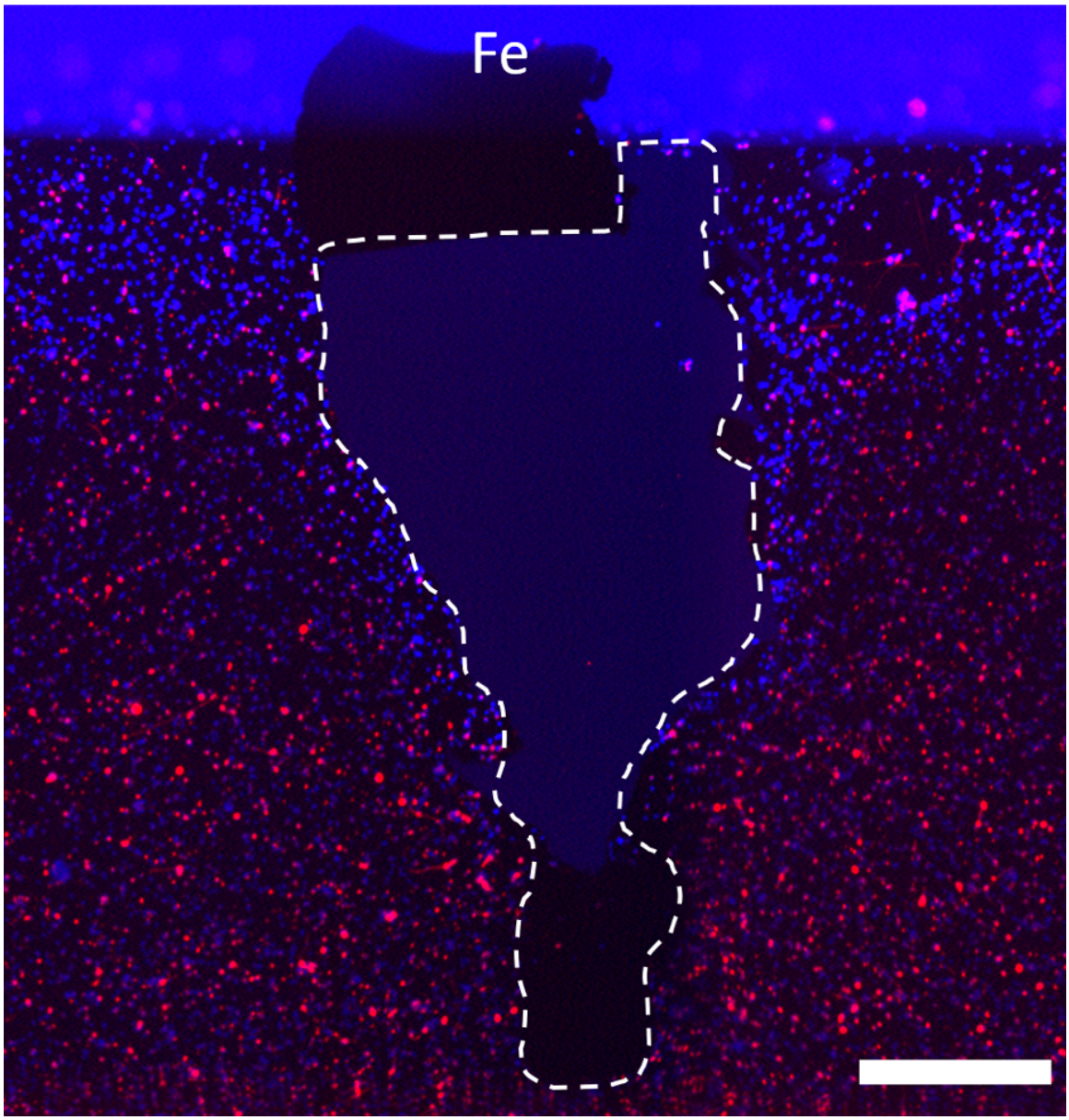

FIGURE 4.2. Delamination of Fe VACNTs.
Delamination of the VACNT forests occured frequently when the tubes were prepared without an Al adhesive layer. Here, we show an area of delamination (outlined in white) in a fluorescence image obtained post-culture. Samples with obvious delamination prior to culture were not used, but the effect was often observed during and post-culture.

walled CNTs (MWCNTs) (Fig. 4.1b). MWCNTs are metallic, so the VACNTs produced via our method meet the basic requirement of electrical conductivity.

The nanotube diameters measured 10-15nm. TEM also revealed the presence of nanoparticle impurities encapsulated within the nanotubes; we did not observe any nanoparticles on the surfaces of the nanotubes. Because of the high contrast and size of these nanoparticles, as seen clearly in Fig. 4.1b, they are composed of atoms much heavier than carbon [122], and they are most likely Fe catalyst nanoparticles. Since transition metal catalysts are known to be cytotoxic [123], this encapsulation should prevent the release of these nanoparticles, thereby improving the biocompatibility of our VACNTs.

4.3.1. Neurite Outgrowth

We assessed the biocompatibility of VACNT forests with retinal neurons by measuring the extent of neurite outgrowth. Fe and Al/Fe preparations supported neuronal process outgrowth for at least 3 DIV (Fig. 4.3) and both preparations contained neurites of several hundred microns. The morphology of glial cells was also similar across both preparations. Normalized neurite lengths were compared across both preparations. Kruskal-Wallis analysis with post-hoc Dunn's testing revealed that samples fabricated with an aluminum underlayer had a median neurite length 3X larger than those with just Fe. However, no statistically significant difference in neurite outgrowth between preparations was found at 3 DIV. Given the extensive delamination observed and general fragility of Fe samples, the Al/Fe preparation was adopted moving forward with patterned substrates.

Having observed the superior mechanical stability of the Al/Fe preparation and its ability to promote neurite outgrowth during 3 DIV cell cultures, we utilized patterned samples with 100μm wide VACNT rows and 100μm wide SiO_2 gaps to determine how neurite outgrowth would change over longer culture durations. The

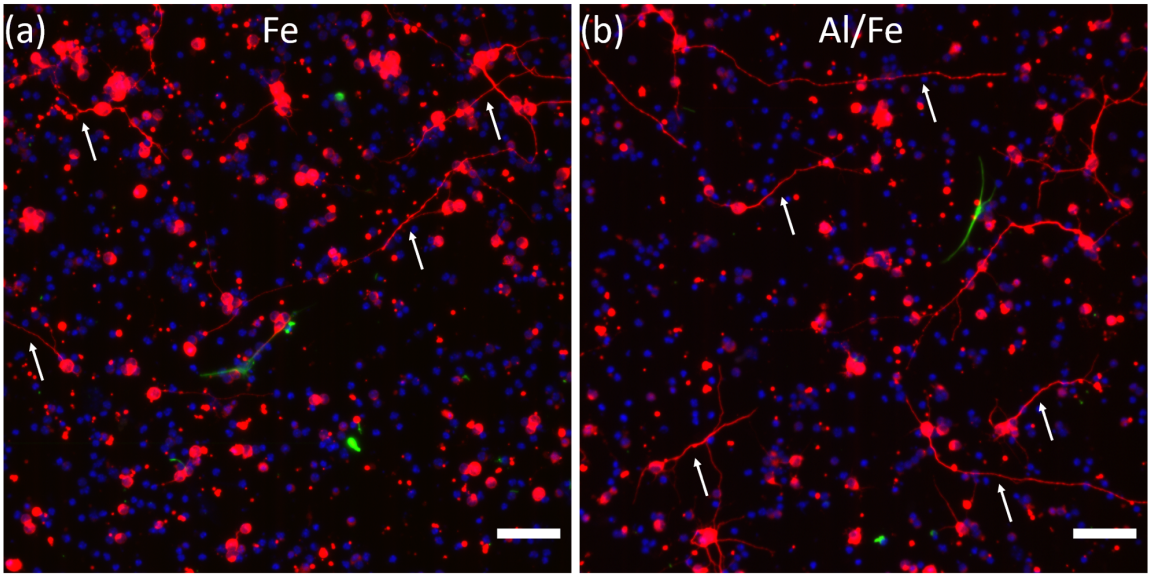

FIGURE 4.3. Neurite outgrowth on Fe and Fe/Al.
A comparison of neurite outgrowth on Fe and Fe/Al substrates at 3DIV revealed the presence of sufficiently long neurites on both substrate preparations and glial cells with similar morhphology. There was no statistical significance in neurite outgrowth between the two groups at 3 DIV.

patterned VACNT rows can be seen in Fig. 4.1c,d. As it has been shown that the height and structure of VACNTs can be affected by the size and geometry of the catalyst patterning [124], the width of the rows was fixed at 100μm. This ensured that neurons were interfacing with VACNTs with similar heights, sufficiently large surfaces (an order of magnitude larger than a cell body), and similar textures to uniform VACNTs. Since textured surfaces are known to affect neurite outgrowth [111], we chose to maintain a consistent texture between all samples. Kruskal-Wallis analysis of the median normalized neurite length on patterned samples showed a statistically significant (p <0.005) increase between 3 and 7 DIV (Fig. 4.4). Although the samples were not rigorously analyzed, excellent neurite outgrowth on VACNTs was also observed at longer culture times. Fig. 4.5a shows extensive outgrowth on a VACNT forest for 8 DIV and Fig. 4.5b shows neurite outgrowth on

100μm VACNT rows after 17 DIV. The SEM image of fixed neurons in Fig. 4.5c show hows neural processes extend along the textured VACNT surface to connect neighboring neurons.

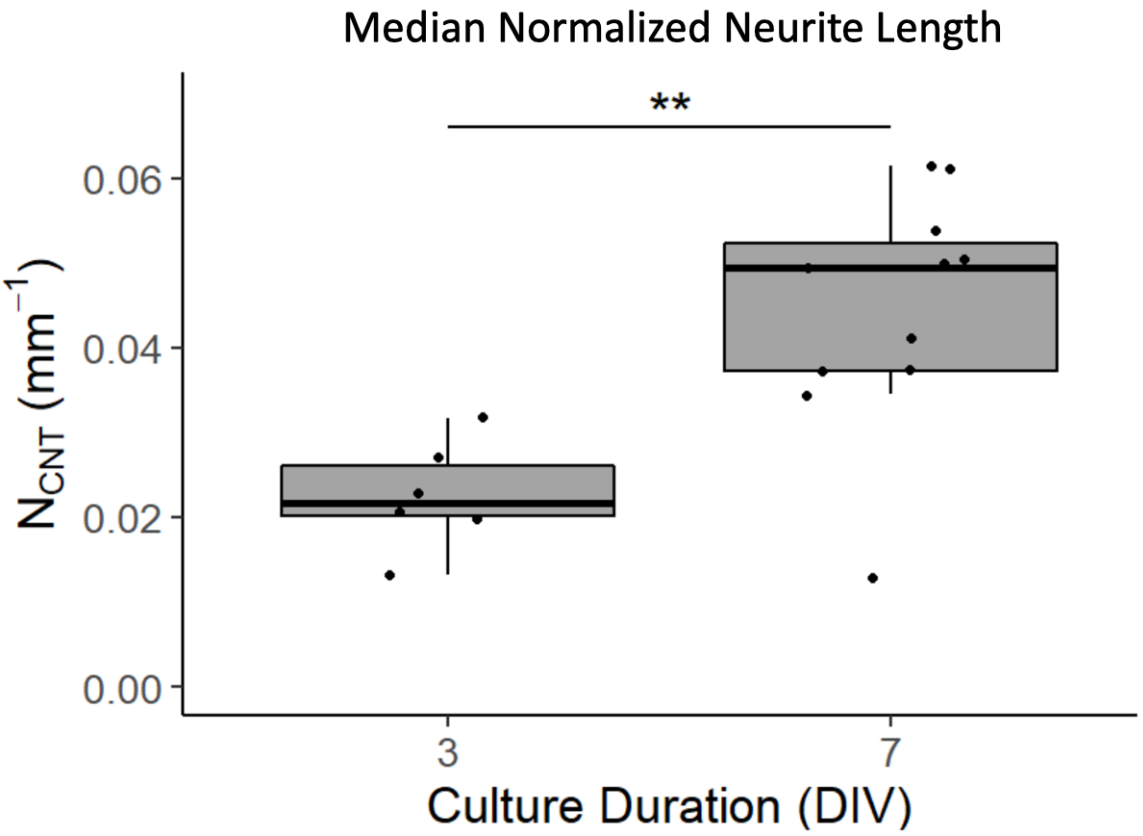

FIGURE 4.4. Neurite length between 3 and 7 DIV.
The median neurite length was calculated on VACNT samples and compared between 3 and 7 DIV using a Kruskal-Wallis analysis. A p value < 0.005 was obtained.

4.3.2. Glial cell distribution

To further assess the biocompatibility of our VACNTs, we analyzed the distribution of retinal glial cells co-cultured with neurons on patterned VACNT substrates. Samples at all SiO_2 gap widths and culture durations displayed large regions of adjacent glial cells in the gaps between VACNT rows. Glial cells were

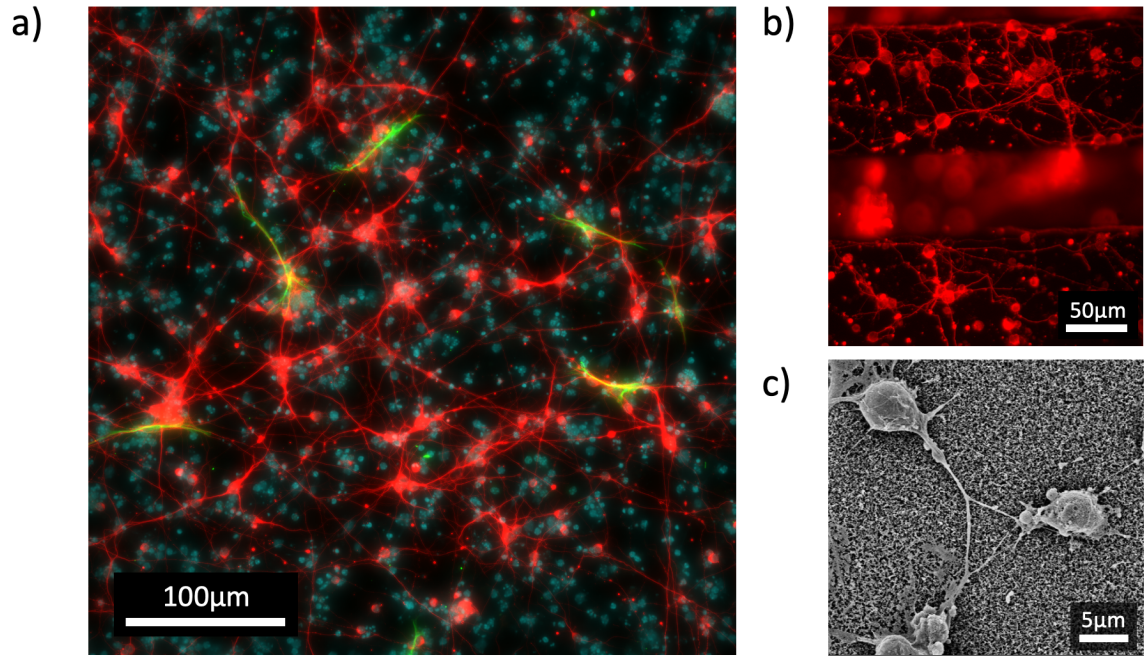

FIGURE 4.5. Neurite outgrowth on VACNTs.
a) A composite fluorescence image showing neurons in red, glia in green, and DAPI (nuclei) in blue reveals excellent neurite outgrowth at 8 DIV. b) Neurite outgrowth on VACNT rows cultured for 17 DIV. c) An SEM showing the morphology of neurons and neural processes on VACNTs.

also observed on top of the VACNT row surfaces, but were almost always observed as isolated single cells rather than groups of connected cells. Fig. 4.6a contains a fluorescence image that demonstrates this phenomenon. The SiO_2 gaps contain a large number of glial cells of various morphologies in close proximity to each other, whereas the VACNT surfaces contain individual glial cells. Fig. 4.6b contains a full sample composite fluorescence image of the patterned VACNT and SiO_2 surfaces that further demonstrates this effect. The vertical green stripes are regions of high glia concentration, which occur exclusively in the smooth SiO_2 gaps between VACNT rows.

To quantify the spatial variation in glial cell prevalence seen on our cultured samples, we determined the normalized glia cell coverage on VACNT and SiO_2

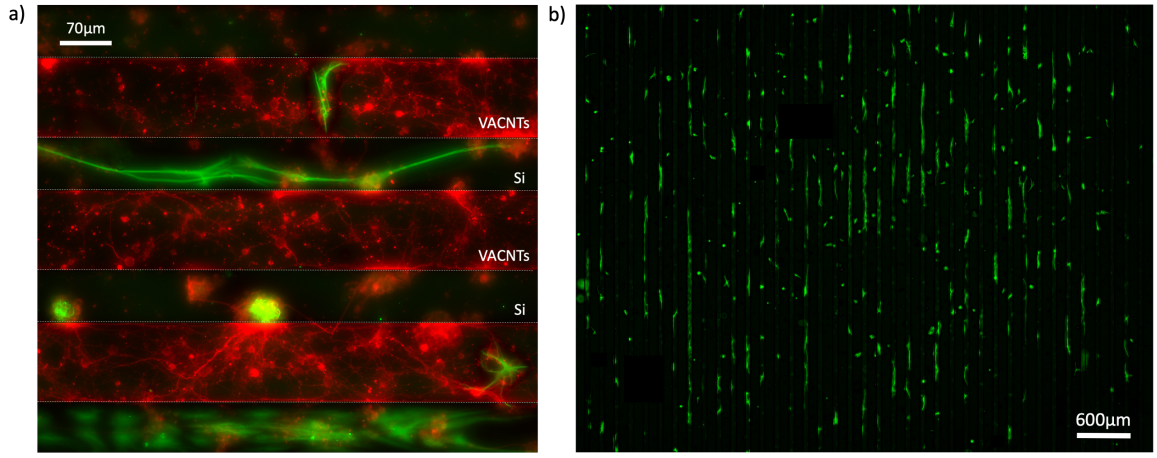

FIGURE 4.6. Glia and neurons on VACNTs.
a) A composite fluorescence image showing β-tubulin III labeled neurons (red) and GFAP labeled glial cells (green). Glial cells are shown preferentially occupying the smooth silicon gaps between VACNT rows, in close proximity to neurons on and off the VACNTs. b) A full sample composite fluorescence image showing clear vertical striations where glia have proliferated in the gaps between the VACNTs.

regions for each sample by analyzing full samples images. The ratio of G_{Si} to G_{CNT} for samples at each gap width and at 7 and 17 DIV can be seen in the box plots in Fig. 4.7.

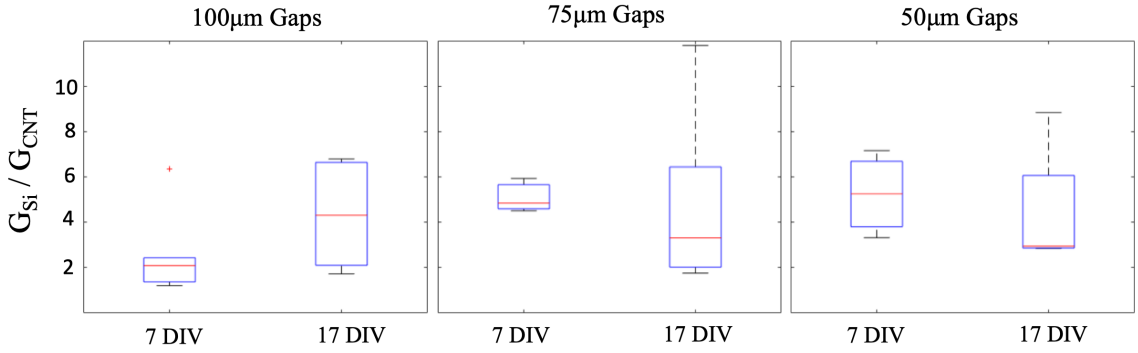

FIGURE 4.7. $G_{\mathrm{Si}}/G_{\mathrm{CNT}}$.
$G_{\mathrm{Si}}/G_{\mathrm{CNT}}$ ratios calculated for each sample group (100, 75, and 50μm gap sizes) at 7 and 17 DIV.

The ratio of G_{Si} to G_{CNT} exceeded the null value of 1 for all samples. For every sample, the calculated p-value was less than 10^{-eps}, or essentially zero, due

to very small standard deviations in the bootstrapped data. It is likely that with a more advanced bootstrapping method, the calculated p-values would be larger. Glial cells exist on the sample as contiguous blocks of bright pixels rather than individual pixels. Assigning a group of pixels of a well-defined size as a "cell" and then randomly dispersing these groups in space would likely result in a larger standard deviation of the null distribution and is therefore a more accurate test of the significance of the data. It is difficult, however, to distinguish individual glial cells in the full sample images due to the multiple glial cell types and morphologies present in our cultures [120]. Regardless, the glial cell distribution for a vast majority of samples greatly exceeded the null hypothesis of $G_{\mathrm{Si}}/G_{\mathrm{CNT}} = 1$, therefore the observed patterned growth is real (i.e. not a probabilistic accident). Our data (as seen in Fig. 4.6) clearly show that glial cell coverage is higher on the SiO_2 surface than the VACNT surface for all gap widths and culture durations.

4.4. Discussion

We investigated whether the addition of an adhesive Al layer resulted in improved mechanical integrity of VACNTs and the extent to which the addition of this layer affected VACNT biocompatibility. We cultured dissociated retinal cells on two VACNT preparations with and without the Al layer. No functionalization with ECM components was used prior to or during the culture, as this would have altered the surface characteristics of our VACNTs. Our goal was not to actively promote cell adhesion and/or survival, but rather study the interactions of retinal neurons with the as-produced VACNT surfaces and to determine whether these different VACNT preparations were stable over time in culture. The median normalized neurite length on VACNTs prepared from an Al underlayer with the

Fe catalyst (Al/Fe preparation) demonstrated a 3X increase, although it was not statistically significant.

Our results established that the Al/Fe and Fe preparations have similar nanotopography and biocompatibility. In fact, the only major difference we detected was that the Fe preparation delaminated easily from the substrate, while the Al/Fe preparation did not. The slight reduction in median neurite outgrowth in the Fe preparation may be due to exposure to VACNTs dispersed in the cell culture medium. In a previous study investigating the effect of dispersed MWCNTs on axonal regeneration of mouse dorsal root ganglia [117], incubation with MWCNTs (10–20μm in length prepared from Fe catalyst) at concentrations increasing from 1μg/mL to 10μg/mL caused a reduction in regenerated axon length by 40% or 70%, respectively, compared to a control. However, these concentrations did not cause cell death. We hypothesize that VACNTs with the Fe preparation occasionally detach either before and/or during the culture, leading to a similar reduction in neurite length without cell death. Since there was no significant difference in neuron density or neurite outgrowth between the two preparations (Fig. 4.3a,b for visual comparison, statistical data not shown), the increase in median normalized neurite length in the Al/Fe preparation likely occurs because of a more favorable growth environment. The addition of the Al underlayer stabilized the VACNT film and yielded favorable neurite outgrowth up to 3 DIV when compared with the Fe preparation. Furthermore, the patterned Al/Fe samples supported neurite outgrowth up to 7 DIV. Therefore, the addition of the Al underlayer constitutes a viable approach for the development of electrodes that may ultimately be used in *in vivo* studies.

Our analysis of the spatial distribution post-culture revealed that glial cells are found at a much higher prevalence between the VACNT rows, within the smooth SiO_2 gaps. The effect was largely independent of the gap widths used and was present at both 7 and 17 DIV. Our results show that VACNTs would likely mitigate the glial inflammatory response when used as an electrode material. Glia, unlike neurons, are able to divide in cell culture. It has been shown that astrocytes readily proliferate on smooth Si/SiO_2 in a process called reactive gliosis [125][100]. It is therefore likely that the large groupings of adjacent glial cells observed in SiO_2 regions on our samples are areas where active proliferation has occurred. It has also been documented that glia do not proliferate as well on soft surfaces [126], so it is likely that the mechanical compliance of 20-30μm VACNT surfaces is a deterrent. In addition, glial cells have been shown to have decreased motility on textured surfaces [101], which makes it more difficult for glia to divide. We hypothesize that the textured nature of our VACNT surfaces prevents glial cell division and therefore mitigates large areas of glial cell proliferation. VACNTs as an electrode material offer promise towards preventing reactive gliosis *in vivo*. Reactive gliosis on top of stimulating electrodes increases tissue impedance and causes a large separation between electrodes and target neurons, both of which decrease the efficacy of an implanted stimulating device. Our results support the notion that VACNT MEAs may be able to localize glial cell proliferation into the smooth areas between active electrodes, leaving the active VACNT area largely unobstructed.

4.5. Conclusion

In conclusion, we produced large-area, uniform VACNTs and uniformly patterned VACNT structures by using a CVD growth process with Fe and Al/Fe

catalysts. VACNT substrates supported retinal neurite growth up to at least 17 DIV. The Al/Fe preparation led to VACNTs with increased mechanical stability and more extensive neurite outgrowth. These results demonstrate that our VACNTs are biocompatible with primary retinal neurons. In addition, we achieved a high-degree of glial cell patterning with VACNTs, wherein glia were largely found in the smooth gaps between patterned VACNT rows, as opposed to on top of the VACNTs, therefore hinting at the material's ability to mitigate scar tissue formation *in vivo*. Taken together, VACNT electrodes synthesized from an Al/Fe catalyst represent an option well worth pursuing to further improve the vision restoration provided by modern retinal implants.

CHAPTER V

RETINAL IMPLANTS WITH CARBON NANOTUBE PENETRATING ARRAYS FOR IN VIVO RETINAL STUDIES

5.1. Introduction

In the previous chapter, I laid the groundwork for VACNTs as a biocompatible electrode material for retinal implant applications through a series of cell culture studies. While *in vitro* experiments demonstrate long-term cell survivability and cell-type selectivity, this environment is much different than an *in vivo* environment like the eye. When transferring this material to *in vivo* applications, many more practical challenges emerge and the need for more complex electrode structures arises.

3D penetrating electrodes — micrometer-scale, needle-like electrodes that penetrate deep into the retinal tissue — promise to improve MEA implants because they allow for closer proximity to the target neurons, thereby decreasing the stimulation threshold and alleviating inflammation [22][23]. It has been shown that 3D microelectrodes have comparable impedance and charge injection to 2D microelectrodes with 3X the diameter, allowing for a 9-fold increase in MEA spatial resolution with similar stimulation performance [127][128]. Extension of the electrode geometry above the implant surface is yet another way to increase electrode surface area, thereby enhancing the electrochemical performance and neurostimulation capabilities [129].

Vertically aligned carbon nanotubes (VACNTs) are an attractive material for penetrating electrodes because of their excellent biocompatibility and neural

stimulation properties, and their intrinsic ability to form mechanically stable, high-aspect-ratio structures. While CNTs have shown promise for use in epiretinal implants [116], the fabrication method used produces randomly oriented CNTs that lack the vertical sidewalls necessary for high density penetrating electrodes. Despite their promise, retinal implants with VACNTs have not been assessed *in vivo*. A key obstacle to *in vivo* work has been to create implants that simultaneously satisfy the physical size requirements (sub-millimeter) for surgical implantation into rodents and the synthesis constraints of high-aspect-ratio VACNT structures, which, although strong, are also mechanically flexible and delicate. Therefore, many fundamental questions remain about the *in vivo* structural integrity and chemical viability of VACNT electrodes and the corresponding *in vivo* physiological response.

In this work, we develop a robust procedure to build passive silicon implants small enough to be implanted into the subretinal space of RCS rats and demonstrate successful implantation. We show that this procedure is compatible with the high-temperature chemical vapor deposition fabrication process used to fabricate VACNT electrodes. Furthermore, we demonstrate the ability of our fabrication process to generate stable, high-aspect ratio VACNT structures down to a few microns. We generate VACNT pillar arrays of various size and spacing and integrate them with passive silicon implant substrates for future *in vivo* retinal studies. This comprehensive *in vivo* platform enables the interrogation of many important questions that remain regarding the use of VACNTs as a high performance electrode material for retinal implants.

5.2. Methods

5.2.1. Implant Fabrication

The size constraints of rodent eyes require new fabrication methods for VACNT-based implants. We fabricated passive silicon implants with lateral dimensions below a millimeter using two different approaches. Bare silicon implants fabricated from each approach were successfully implanted into the subretinal space of RCS rats as a surgical proof-of-concept for our design. We use high-temperature chemical vapor deposition (CVD) to grow VACNT penetrating electrode arrays on passive implants fabricated using the second approach. We generate arrays of various heights, diameters, and spacing.

5.2.1.1. Optical Lithography

Standard optical lithography procedures were utilized in multiple contexts throughout this work. Briefly, Si wafers or chips were cleaned with solvents, dehydrated on a 400°C hot plate for 15 minutes, and vapor-coated with hexamethyldisilazane (HMDS) for 20 minutes to promote photoresist adhesion. AZ-1512 positive resist (MicroChemicals GmbH) was spun on at 4000rpm and soft-baked for 2.5 minutes at 105°C to drive out resist solvents. Pattern designs were generated in CleWin 5 CAD software and transferred to the substrate with a 405nm laser using a dose of 220mJ/cm^2. A post-exposure bake was done for 60s at 105°C and samples were subsequently developed in AZ 300 MIF (1-3% TMAH) developer for 60s. Hard bake times varied from 2-15 minutes based on successive processing steps.

5.2.1.2. First-generation silicon implants

The first method of fabrication we used to micromachine sub-millimeter silicon implants utilized a silicon wet etch. Potassium hydroxide (KOH) is a common etchant used to dissolve silicon. KOH dissolves the various crystal planes of silicon at different rates, thus resulting in an orientation dependent etch [130]. For example, a solution containing 19 wt% KOH in deionized (DI) water at about 80°C removes the (100)-plane at a much greater rate than the (110)- and (111)-planes, with an etch rate ratio of 100:16:1. When used to etch patterned (100) silicon, the solution will carve out U-shaped grooves with sidewalls that are sloped at precisely 54.7°. This is demonstrated in Fig. 5.1.

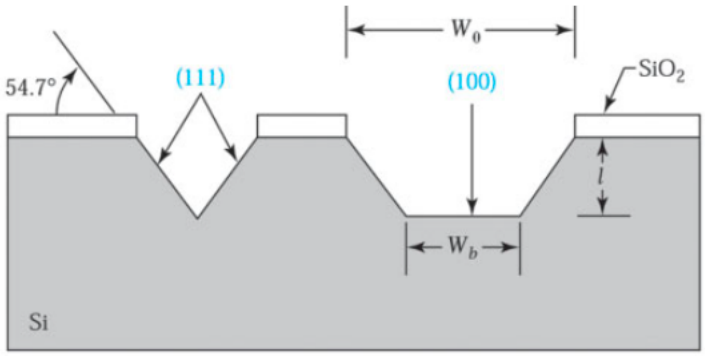

FIGURE 5.1. KOH etching of silicon.
A diagram showing the way in with potassium hydroxide (KOH) etches the different crystal planes of silicon [130].

We started with (100) double-side polished silicon wafers with 100nm of Si_3N_4 on each side. Si_3N_4 functions as an etch mask for KOH on silicon. 2x2cm chips were cut from a larger 2in wafer. An initial round of optical lithography was used to open a 500μm square window in the center of each chip for double-sided pattern alignment. The Si_3N_4 covering this window was removed using CHF_3 gas in an inductively coupled plasma (ICP) dry etch (Oxford Instruments) for 150s. The

chips were then suspended from Teflon tweezers in 30% by weight KOH solution, saturated with IPA, for 2.5 hours at 90°C with a stir bar. During this time, the KOH drilled a square hole through the center of each chip. An example of the result can be seen in Fig. 5.2a. By nature of the etch and crystal structure of Si, the square on the top surface of the chip was perfectly aligned to the square on the back side. As a result, the following two lithography steps on the front and back side were in alignment since they were independently aligned to the corners of each square on their respective faces.

We patterned long vertical stripes on the top side of each chip to create 500μm wide suspended silicon beams from which to separate our devices. On the back side of the chip, we patterned 8 small rectangles perpendicular to each beam defined from the front side lithography. The dimensions of the rectangles were chosen such that the KOH would not etch all the way through from the back, but terminate early such that individual devices remained partially connected. After each round of lithography, exposed Si_3N_4 was removed by a dry etch step in the ICP. We then suspended the chip vertically in an identical KOH solution for 2.5 hours at 90°C with a stir bar. The KOH etched through the Si from both sides simultaneously, creating numerous independent chips along each beam that can then be easily separated from each other with tweezers, as shown in Fig. 5.2b.

5.2.1.3. Second-generation silicon implants

While wet etching of silicon with a KOH solution allowed us to batch fabricate multiple implant devices from the same chip in-house, it was difficult to integrate the wet etch process with the process for chemical vapor deposition of patterned VACNT arrays. For this reason, an alternative approach was used for

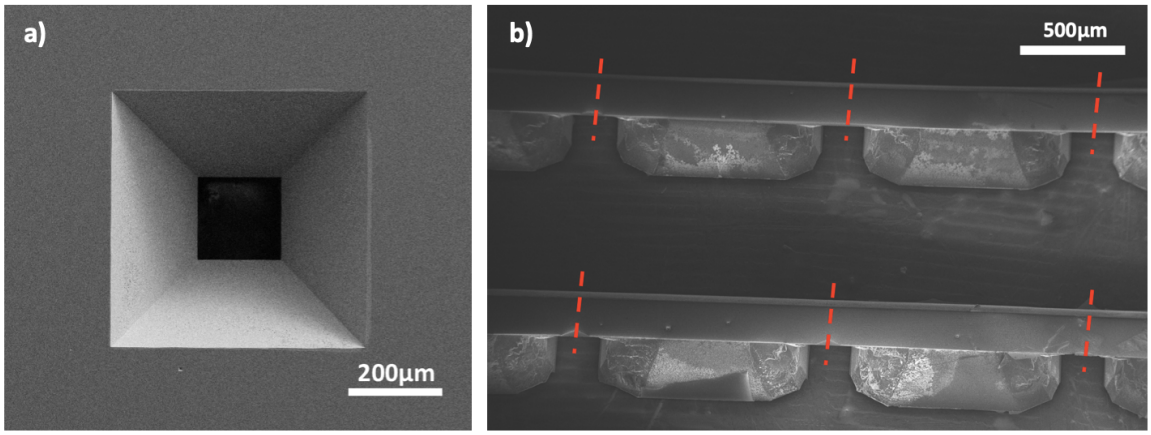

FIGURE 5.2. First generation implant devices.
a) A hole driven through the center of each chip created a front and back-side square for multi-step lithography alignment. b) First generation devices were micromachined from Si such that they could be independently separated from each beam.

second generation implants. (110) double-side polished wafers with 100nm of Si_3N_4 on each side were patterned and metallized with 20μm lines and arrays of circles with differing size and pitch. After patterning and metallization, the wafer surface was coated with AZ-1512 positive photoresist and soft-baked to drive out resist solvent. The wafer was packaged and shipped to the nanofabrication facility at UC Santa Barbara, where an ADT 7100 dicing saw with a 30μm nickel-hubbed blade was used to cut along the thin metal lines. Blade width was accounted for during pattern design, resulting in implant dimensions of roughly 500x1000x250μm. These implants have similar dimensions to the first generation devices, but are perfectly rectangular. The result of the dicing process can be seen in Fig. 5.3.

5.2.1.4. Chemical vapor deposition of high aspect ratio VACNTs

VACNTs can be grown with extremely high aspect ratio using chemical vapor deposition (CVD) at atmospheric pressure. After patterning, Si substrates with

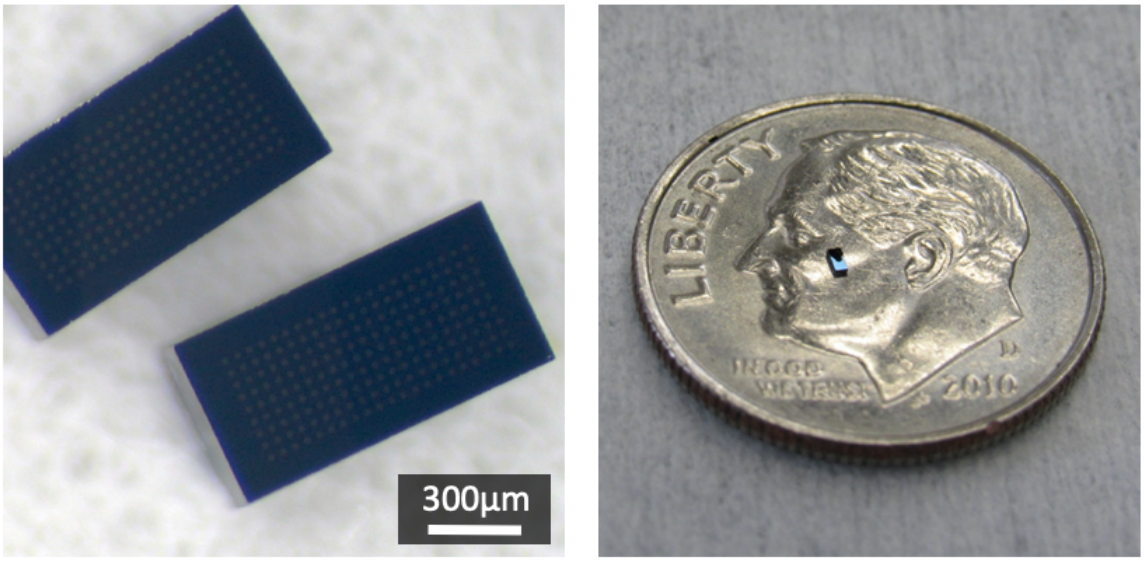

FIGURE 5.3. 2nd generation implant devices
The second generation of rodent implant devices were created by dicing a silicon wafer to sub-millimeter dimensions. A device resting on a dime shown for scale.

a 100nm layer of Si_3N_4 were placed in a thermal evaporator. A 3nm layer of Al, which immediately oxidizes to form an alumina adhesive layer (see Ch. 4), and a 6nm layer of Fe were deposited on the substrate surface. Lift-off of photoresist was done in acetone with sonication for 10 minutes. Patterned and metallized samples were placed carefully into a a 2" quartz tube furnace and slowly heated at atmospheric pressure. When the furnace reached 650°C, a 2:1 mixture of ethylene (C_2H_4) and hydrogen (H_2) at 200 and 100 SCCM, respectively, in the presence of 600 SCCM flow of argon (Ar), was injected for 0.5-3 minutes. Representative examples of high aspect ratio VACNT structures can be seen in Fig. 5.4.

5.2.2. *in vivo* implantation

Post-natal day 23 RCS rats (N=10) were anesthetized with a ketamine/xylazine cocktail (80/5 mg/kg, respectively). The animals were placed on a heated pad under a dissecting microscope and their eyes were dilated using

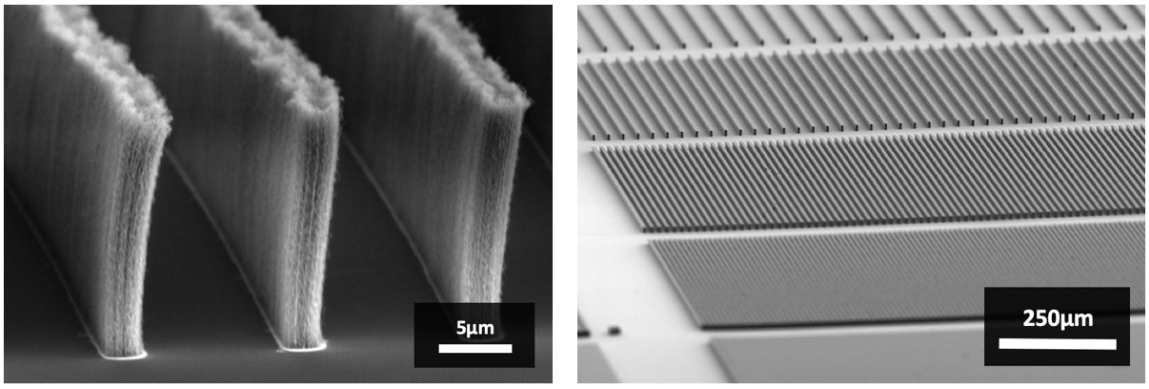

FIGURE 5.4. High aspect ratio VACNT structures.
Images showing high aspect ratio VACNT structures prepared using photolithography and chemical vapor deposition. Aspect ratios as high as ∼20 were obtained, with feature sizes down to 2.5μm.

1.0% trapicamide and 2.5% phenylephrine. The conjunctiva of the dorsotemporal right eye was then resected using forceps and iris scissors. Upon locating a position on the sclera with no large blood vessels, a 30ga hypodermic needle was inserted through the sclera/choroid creating a tunnel into the subretinal space. An additional clean 30ga needle was used to puncture the cornea at the lateral margin to allow aqueous humor to flow outward to compensate for pressure changes upon injection. A handmade glass pipette was inserted into the subretinal space and used to inject 4μL of sterile saline. An 18ga hypodermic needle was then used to widen the scleral tunnel, being careful not to insert the needle tip too deeply. Fine tip (Fine Science Tools) or ILM peel forceps were used to grab the implant and insert it through the widened scleral tunnel. After insertion, the scleral tunnel was either sutured or glued closed and the conjunctiva replaced over the scleral incision. Placement of the implant was confirmed through indirect ophthalmoscopy. Animals with significant retinal or choroidal bleeds were removed from the study.

5.3. Results

Bare silicon implants, identical to those seen in Fig. 5.3 but without patterning, were successfully implanted into the subretinal space of N=10 RCS rats throughout the course of this project. Immediately prior to sacrifice at P30 (7 days post-implantation), animals were anesthetized and fundus photographs were taken of the implant in the subretinal space. A representative image of implant placement can be seen in Fig. 5.5a. Importantly, the implant is located beneath the blood vessel, verifying correct subretinal placement. The animals were then euthanized and the eyes recovered. Following 2 hour fixation in 4% paraformaldehyde, the anterior chamber of the eye was cut away and the lens removed revealing the implant embedded beneath the neural retina, seen in Fig. 5.5b.

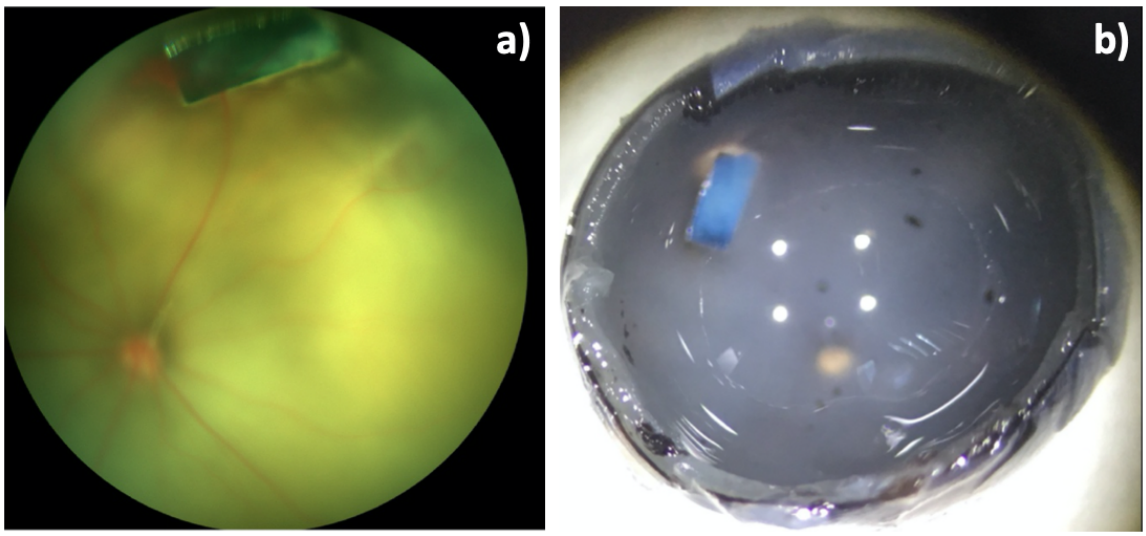

FIGURE 5.5. Implant bare silicon implants.
a) A fundus photograph showing subretinal placement of a bare silicon implant post-implantation. The implant is located underneath the blood vessel (red). b) A dissected retina after euthanasia further confirms implant placement under the neural retina.

Final VACNT devices were roughly 500μm wide, 1mm long, and 250μm thick. A sampling of the final devices can be seen in Fig. 5.6. Our fabrication method

allows us to create custom VACNT electrode arrays with varying width and pitch. Pillar widths presented here ranged from 10-40μm and pillar heights were $\sim$15-30μm. At these sizes, the VACNT pillars were vertical and stable. Minimal bending of the electrode structures was observed.

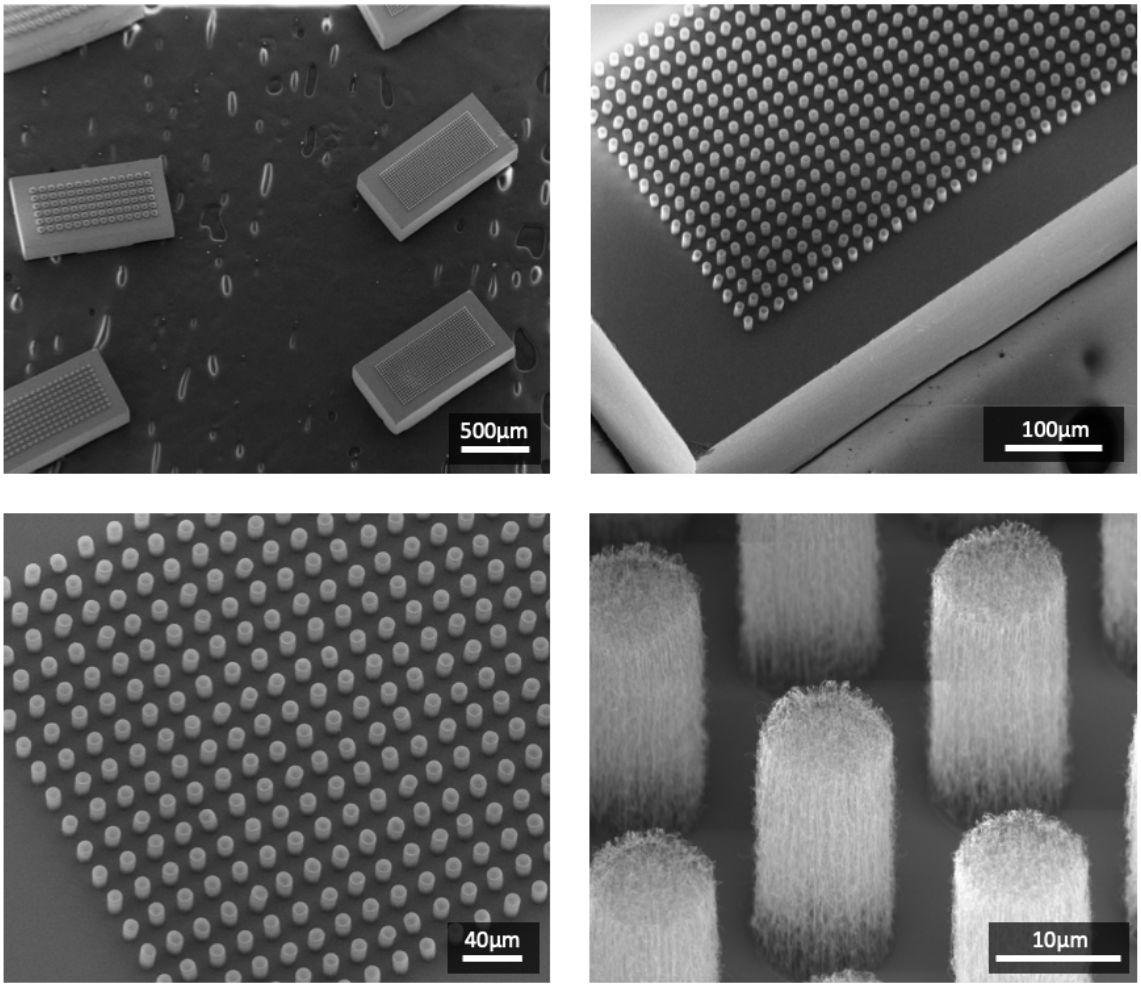

FIGURE 5.6. VACNT retinal implant platform device.
Final VACNT platform devices contained multiple different arrays with various size, spacing, and VACNT pillar heights.

5.4. Discussion

We developed two viable methods for micro-machining silicon into sub-millimeter retinal implants small enough to be implanted in the eyes of RCS rats. Devices generated with both methods were successfully implanted, however the results presented only include second generation devices since first generation devices were incompatible with subsequent fabrication steps for VACNT electrodes. Our implantation procedure allows for correct placement of passive silicon devices into the subretinal space. In some instances, however, retinal detachment from the retinal pigment epithelium was observed, in addition to substantial inflammation and device encapsulation. This is likely caused by the rigidity and thickness of our devices (250μm), as the inflammatory response of the body to rigid implants is well documented [125][100]. While soft, flexible substrates are used extensively in other neural interface applications [131][132], subretinal implants necessarily require semiconducting substrates like Si for wireless power. Photovoltaic subretinal implants with a device thickness down to $\sim$30μm, however, are able to absorb a sufficient amount of light while being thin enough to mitigate damage and inflammation during and post-implantation [18]. The thickness of our Si implants can be decreased using a variety of methods without impacting the viability of our fabrication approach. Future generation implants will have a significant reduction in thickness.

Our passive Si implants are compatible with the CVD growth of VACNTs from an Al/Fe catalyst layer. We have demonstrated the ability to grow high-aspect-ratio VACNT structures with aspect ratios of at least $\sim$20. Using this process, we created comprehensive passive implant devices with a variety of different VACNT electrode pillar arrays for use in *in vivo* experiments. Because

our method is compatible with standard optical lithography, it is possible to create VACNT electrode arrays with a great deal of customizability. The pillar structures presented here are relatively modest and the limits of the process have not been thoroughly explored. It is likely that structures with even higher aspect ratios could be obtained. Restoration of normal visual acuity (20/20) corresponds to an implant pixel size of 5μm [20], and a penetrating electrode must be $\sim$30μm tall to pass all the way through the photoreceptor debris of the inner nuclear layer [23]. Stable aspect ratios in excess of 5 are required to simultaneously meet both of these conditions. The VACNT pillar electrodes presented here are well poised to meet the aspect ratio requirements needed to restore high VA. In the future, we aim to use our approach to identify the optimal pillar penetration depth that simultaneously maximizes electrode stability and minimizes the immune response of the retina post-implantation.

5.5. Conclusion

This work makes the crucial first step towards assessing the viability of VACNTs as an electrode material in MEA-based retinal implants. We have demonstrated two methods for the fabrication of bare silicon implants with sub-millimeter features that are small enough to be surgically implanted into the subretinal space of rats. Furthermore, we have shown that our bare silicon implants can be seamlessly integrated with the photolithography and chemical vapor deposition processes necessary for developing customized MEA implants with high-aspect-ratio VACNT electrodes. This platform will enable us to answer many fundamental questions about the long-term integrity and viability of VACNTs in

a physiological environment. If proven to be stable *in vivo*, VACNT penetrating electrodes offer promise for restoring high resolution vision to blind patients.

CHAPTER VI

FUTURE DIRECTIONS: TOWARDS A COMPLETE STIMULATION PLATFORM.

In the previous chapters, I demonstrated how surface area enhancement of stimulating electrodes can improve retinal neuron stimulation from both a microscale and nanoscale perspective. Increasing the electrode surface area allows an electrode to store more charge for use in neurostimulation, thereby increasing the efficacy of stimulation. This is particularly impactful for MEA-based applications like retinal implants, where a substantial decrease in electrode size is necessary, yet risky.

In Chapter 3, I outlined an experiment that uses electric force microscopy to directly measure the relative penetration depth of the electric force gradient above different micro-patterned electrode geometries and showed that certain geometries better maximize the activating function. The activating function has long been used as a metric to predict likelihood of stimulation and, while limited, provides a means for qualitative comparison. Microscale patterning also allows for an increase in electrode capacitance and a decrease in electrode impedance. Together, these factors contribute towards more effective stimulation of target neural tissue.

In Chapter 4, I introduced vertically aligned carbon nanotubes (VACNTs) as an ideal electrode material for stimulating neurons and demonstrated biocompatibility with primary retinal neurons. In addition, I demonstrated that textured VACNTs have the ability to suppress glial cell proliferation, which may favorably suppress the immune response *in vivo*. VACNT electrode structures are porous, with rough textured surfaces. In addition to the myriad of other

favorable properties, the nanotopography of the material greatly increases the electrochemical surface area (ESA) over the geometric surface area (GSA). Increasing the ESA/GSA ratio increases electrode capacitance for a given electrode footprint since charge can theoretically be stored within the porous, nanoscale features of the material.

In Chapter 5, I demonstrated that high aspect ratio VACNT electrode structures can be used as penetrating electrodes - electrodes which extend up off the surface of an implant and therefore draw closer to the target tissue. Closer proximity to the target tissue is a way to effectively increase the stimulation capability since stimulation strength usually drops off quickly with increasing distance to the electrode surface. In addition, the vertical sidewalls of 3D penetrating electrodes offer more surface area for charge storage. Furthermore, I showed that VACNT electrode structures are compatible with a silicon micromachining process for creating sub-millimeter rodent implants. The developed platform will allow for a comprehensive study of VACNT pillar dimensions and their effect on tissue reorganization *in vivo*.

Any one of these approaches - electrode micro-patterning, electrode materials with nanoscale porosity, or penetrating electrode structures - promise to improve the efficacy of retinal neuron stimulation. A platform that combines all three, therefore, is likely to be a very powerful approach. Because VACNTs can be patterned with a stable high aspect ratio, they are an ideal candidate for electrode micro-patterning. As explained in Chapter 5, our VACNT preparation is unique compared to others in the retinal implant field in that it generates near-perfect vertical sidewalls such that structures can be patterned with aspect ratios $\sim$20 or higher with feature sizes below a few microns.

As a first step towards an integrated platform, we were interested in testing whether or not our VACNT growth process would be compatible with the microscale patterns first introduced in Ch. 3. We utilized electron beam lithography to generate the same subset of geometries and subjected them to the VACNT growth process outlined in both Ch. 4 and Ch. 5. As shown in Fig. 6.1, we were successfully able to fabricate arrays of electrodes, with each of the six geometries represented. The smallest feature size was that of the Hilbert curve, as shown in the bottom right corner of Fig. 6.2, with a feature line width of $\sim$700nm. The aspect ratio for these structures was $\sim$6 or lower. The limits of this process were not tested and it is likely that feature sizes could be further reduced and aspect ratios increased. As demonstrated, VACNTs allow for superb pattern control with extremely small feature sizes. The combined effects of the high surface area VACNT material, high surface area geometries, and increased tissue penetration are expected to result in very favorable electrochemical and neurostimulation properties.

The next step in this work is to measure the enhancement in the electrochemical properties of patterned VACNT electrode structures. Measuring the electrochemical properties of these structures, using both cyclic voltammetry and electrochemical impedance spectroscopy, would allow us to quantify the expected increase in charge storage capacity and decrease in electrode impedance. These quantities elucidate much about the stimulation capability and are a critical step towards comparing our electrodes to existing technology. That being said, electrochemical measurements offer a limited view into how an electrode will behave when implanted into a living person or animal. To truly determine whether these structures can enhance stimulation capability, they must be integrated into a fully-

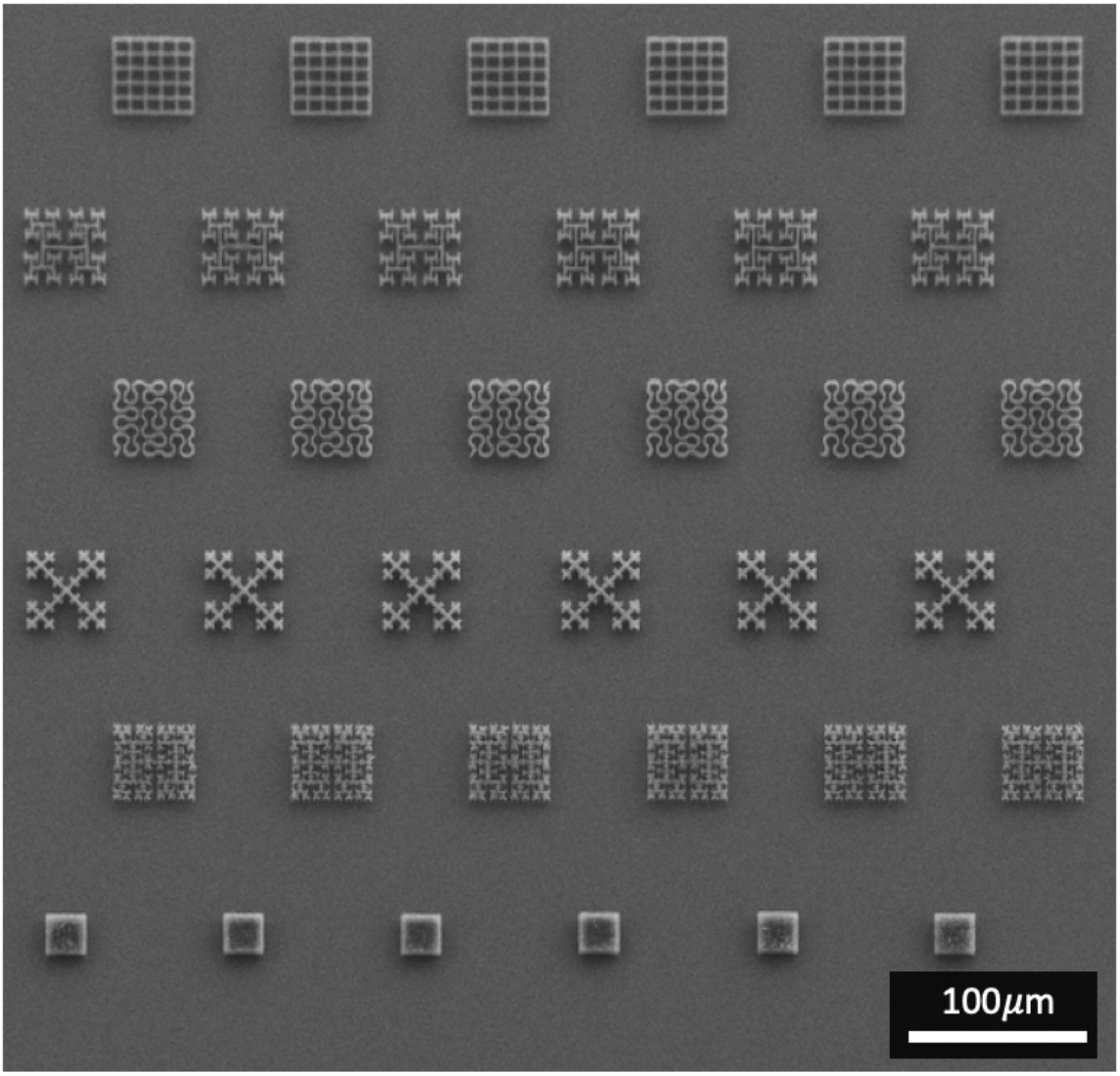

FIGURE 6.1. VACNT fractal and Euclidean geometries.
We utilized electron beam lithography to generate VACNT structures that match the patterns used for the experiments of Chapter 3.

functioning electronic device and implanted. While we have developed the means to study passive VACNT electrode structures *in vivo*, the electronic integration of these electrodes into a fully functioning device requires a significant amount of further engineering and introduces a whole new set of challenges that must be surmounted.

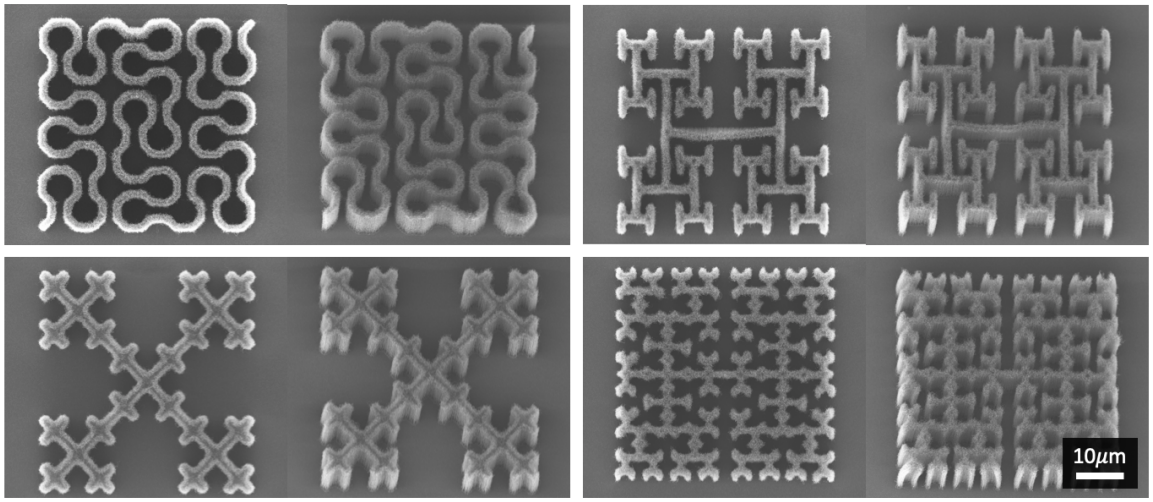

FIGURE 6.2. VACNT Ebeam Lithography.
VACNT electrode structures micro-patterned in various fractal geometries combine excellent material properties, microscale surface area enhancement, and tissue penetration to improve retinal neuron stimulation.

Taken as a whole package, the electrode surface area enhancements presented in this dissertation are expected to improve the ability of a retinal implant electrode to stimulate retinal bipolar cells. The overall goal of engineering better subretinal implant electrodes is to safely increase the magnitude of stimulation without increasing the electrode footprint. In a photodiode-based subretinal implant, this would alleviate the need for multiple photodiodes, allowing for a further decrease in pixel size and spacing. Retinal implant MEAs would consequently be able to maintain their stimulation ability as pixel sizes are decreased to the extent needed for high resolution. Without this increase MEA density, it is unlikely that retinal implants will ever restore functional vision to the millions of patients blinded by diseases like Macular Degeneration and Retinitis Pigmentosa. Furthermore, the results outlined in this thesis have implications beyond just the retina, as low charge injection capabilities and high electrode impedance are issues that plague almost every application of neural stimulation.

REFERENCES CITED

[1] R. K. Shepherd, *Medical Neurobionics: Fundamental Studies and Clinical Applications*. Hoboken, NJ, USA: John Wiley & Sons, Inc., 8 2016.

[2] G. E. Loeb, "Neural Prosthetics: A Review of Empirical vs. Systems Engineering Strategies," *Applied Bionics and Biomechanics*, vol. 2018, 2018.

[3] C. G. Ngan, R. M. Kapsa, and P. F. Choong, "Strategies for neural control of prosthetic limbs: From electrode interfacing to 3D printing," *Materials*, vol. 12, no. 12, 2019.

[4] E. H. Rijnbeek, N. Eleveld, and W. Olthuis, "Update on Peripheral Nerve Electrodes for Closed-Loop Neuroprosthetics," *Frontiers in Neuroscience*, vol. 12, p. 350, 5 2018.

[5] E. Fernández, B. Greger, P. A. House, I. Aranda, C. Botella, J. Albisua, C. Soto-Sánchez, A. Alfaro, and R. A. Normann, "Acute human brain responses to intracortical microelectrode arrays: Challenges and future prospects," *Frontiers in Neuroengineering*, vol. 7, no. JUL, 2014.

[6] A. D. Sdrulla, Y. Guan, and S. N. Raja, "Spinal Cord Stimulation: Clinical Efficacy and Potential Mechanisms," *Pain Practice*, vol. 18, no. 8, pp. 1048–1067, 2018.

[7] A. M. Lozano, N. Lipsman, H. Bergman, P. Brown, S. Chabardes, J. W. Chang, K. Matthews, C. C. Mcintyre, T. E. Schlaepfer, M. Schulder, Y. Temel, J. Volkmann, and J. K. Krauss, "Deep brain stimulation: current challenges and future directions Europe PMC Funders Group," *Nat Rev Neurol*, vol. 15, no. 3, pp. 148–160, 2019.

[8] T. Lenarz, "Cochlear implant – state of the art," *GMS Current Topics in Otorhinolaryngology, Head and Neck Surgery*, vol. 16, 2017.

[9] E. Bloch, Y. Luo, and L. da Cruz, "Advances in retinal prosthesis systems," *Therapeutic Advances in Ophthalmology*, vol. 11, p. 251584141881750, 1 2019.

[10] D. T. Hartong, E. L. Berson, and T. P. Dryja, "Retinitis pigmentosa," 11 2006.

[11] R. D. Jager, W. F. Mieler, and J. W. Miller, "Age-Related Macular Degeneration," *New England Journal of Medicine*, vol. 358, pp. 2606–2617, 6 2008.

[12] G. A. Goetz and D. V. Palanker, "Electronic approaches to restoration of sight," *Reports on Progress in Physics*, vol. 79, no. 9, p. 096701, 2016.

[13] A. K. Ahuja, J. D. Dorn, A. Caspi, M. J. McMahon, G. Dagnelie, L. DaCruz, P. Stanga, M. S. Humayun, and R. J. Greenberg, "Blind subjects implanted with the Argus II retinal prosthesis are able to improve performance in a spatial-motor task," *British Journal of Ophthalmology*, vol. 95, pp. 539–543, 4 2011.

[14] E. Zrenner, K. U. Bartz-Schmidt, H. Benav, D. Besch, A. Bruckmann, V.-P. Gabel, F. Gekeler, U. Greppmaier, A. Harscher, S. Kibbel, J. Koch, A. Kusnyerik, T. Peters, K. Stingl, H. Sachs, A. Stett, P. Szurman, B. Wilhelm, and R. Wilke, "Subretinal electronic chips allow blind patients to read letters and combine them to words," *Proceedings of the Royal Society B: Biological Sciences*, vol. 278, no. 1711, pp. 1489–1497, 2011.

[15] D. Palanker, Y. Le Mer, S. Mohand-Said, M. Muqit, and J. A. Sahel, "Photovoltaic Restoration of Central Vision in Atrophic Age-Related Macular Degeneration," in *Ophthalmology*, vol. 0, Elsevier Inc., 2020.

[16] L. N. Ayton, P. J. Blamey, R. H. Guymer, C. D. Luu, D. A. Nayagam, N. C. Sinclair, M. N. Shivdasani, J. Yeoh, M. F. McCombe, R. J. Briggs, N. L. Opie, J. Villalobos, P. N. Dimitrov, M. Varsamidis, M. A. Petoe, C. D. McCarthy, J. G. Walker, N. Barnes, A. N. Burkitt, C. E. Williams, R. K. Shepherd, and P. J. Allen, "First-in-human trial of a novel suprachoroidal retinal prosthesis," *PLoS ONE*, vol. 9, 12 2014.

[17] J. F. Rizzo, "Update on Retinal Prosthetic Research: The Boston Retinal Implant Project," *Journal of Neuro-Ophthalmology*, vol. 31, pp. 160–168, 6 2011.

[18] L. Wang, K. Mathieson, T. I. Kamins, J. D. Loudin, L. Galambos, G. Goetz, A. Sher, Y. Mandel, P. Huie, D. Lavinsky, J. S. Harris, and D. V. Palanker, "Photovoltaic retinal prosthesis: implant fabrication and performance," *Journal of Neural Engineering*, vol. 9, no. 4, p. 046014, 2012.

[19] D. Boinagrov, S. Pangratz-Fuehrer, G. Goetz, and D. Palanker, "Selectivity of direct and network-mediated stimulation of the retinal ganglion cells with epi-, sub- and intraretinal electrodes," *Journal of Neural Engineering*, vol. 11, p. 026008, 3 2014.

[20] D. Palanker, A. Vankov, P. Huie, and S. Baccus, "Design of a high-resolution optoelectronic retinal prosthesis," *Journal of Neural Engineering*, vol. 2, no. 1, pp. S105–S120, 2005.

[21] D. Boinagrov, X. Lei, G. Goetz, T. I. Kamins, K. Mathieson, L. Galambos, J. S. Harris, and D. Palanker, "Photovoltaic Pixels for Neural Stimulation: Circuit Models and Performance," *IEEE TRANSACTIONS ON BIOMEDICAL CIRCUITS AND SYSTEMS*, vol. 10, no. 1, 2016.

[22] A. Butterwick, P. Huie, B. W. Jones, R. E. Marc, M. Marmor, and D. Palanker, "Effect of shape and coating of a subretinal prosthesis on its integration with the retina," *Experimental Eye Research*, vol. 88, pp. 22–29, 2008.

[23] T. Flores, X. Lei, T. Huang, H. Lorach, R. Dalal, L. Galambos, T. Kamins, K. Mathieson, and D. Palanker, "Optimization of pillar electrodes in subretinal prosthesis for enhanced proximity to target neurons," *Journal of Neural Engineering*, vol. 15, p. 036011, 6 2018.

[24] L. S. Robblee and T. L. Rose, "Electrochemical Guidelines for Selection of Protocols and Electrode Materials for Neural Stimulation," in *Neural Prostheses: Fundamental Studies*, pp. 25–66, Prentice Hall, 1990.

[25] D. R. Merrill, M. Bikson, and J. G. Jefferys, "Electrical stimulation of excitable tissue: Design of efficacious and safe protocols," *Journal of Neuroscience Methods*, vol. 141, no. 2, pp. 171–198, 2005.

[26] U. A. Aregueta-Robles, A. J. Woolley, L. A. Poole-Warren, N. H. Lovell, and R. A. Green, "Organic electrode coatings for next-generation neural interfaces," *Frontiers in Neuroengineering*, vol. 7, 5 2014.

[27] S. F. Cogan, "Neural Stimulation and Recording Electrodes," *Annual Review of Biomedical Engineering*, vol. 10, no. 1, pp. 275–309, 2008.

[28] S. F. Cogan, J. Ehrlich, and T. D. Plante, "The effect of electrode geometry on electrochemical properties measured in saline," in *2014 36th Annual International Conference of the IEEE Engineering in Medicine and Biology Society, EMBC 2014*, pp. 6850–6853, Institute of Electrical and Electronics Engineers Inc., 11 2014.

[29] J. D. Weiland, D. J. Anderson, and M. S. Humayun, "In vitro electrical properties for iridium oxide versus titanium nitride stimulating electrodes," *IEEE Transactions on Biomedical Engineering*, vol. 49, pp. 1574–1579, 12 2002.

[30] F. D. e. a. Purves D, Augustine GJ, "The Retina - Neuroscience - NCBI Bookshelf," 2001.

[31] H. Wässle, "Parallel processing in the mammalian retina," 10 2004.

[32] "Rods - American Academy of Ophthalmology."

[33] R. H. Masland, "The fundamental plan of the retina," 2001.

[34] E. Vecino, F. D. Rodriguez, N. Ruzafa, X. Pereiro, and S. C. Sharma, "Glia-neuron interactions in the mammalian retina," 3 2016.

[35] F. W. Pfrieger and B. A. Barres, "New views on synapse-glia interactions," *Current Opinion in Neurobiology*, vol. 6, pp. 615–621, 10 1996.

[36] M. J. Carson, J. M. Doose, B. Melchior, C. D. Schmid, and C. C. Ploix, "CNS immune privilege: Hiding in plain sight," 10 2006.

[37] S. Veleri, C. H. Lazar, B. Chang, P. A. Sieving, E. Banin, and A. Swaroop, "Biology and therapy of inherited retinal degenerative disease: Insights from mouse models," 2 2015.

[38] F. Parmeggiani, F. S. Sorrentino, D. Ponzin, V. Barbaro, S. Ferrari, and E. Di Iorio, "Retinitis Pigmentosa: Genes and Disease Mechanisms," *Current Genomics*, vol. 12, pp. 238–249, 5 2011.

[39] L. G. Fritsche, R. N. Fariss, D. Stambolian, G. R. Abecasis, C. A. Curcio, and A. Swaroop, "Age-Related Macular Degeneration: Genetics and Biology Coming Together," *Annual Review of Genomics and Human Genetics*, vol. 15, pp. 151–171, 8 2014.

[40] D. S. Friedman, B. J. O'Colmain, B. Muñoz, S. C. Tomany, C. McCarty, P. T. DeJong, B. Nemesure, P. Mitchell, J. Kempen, and N. Congdon, "Prevalence of Age-Related Macular Degeneration in the United States," *Archives of Ophthalmology*, vol. 122, pp. 564–572, 4 2004.

[41] J. Ambati and B. J. Fowler, "Mechanisms of age-related macular degeneration," 7 2012.

[42] R. P. Danis, J. A. Lavine, and A. Domalpally, "Geographic atrophy in patients with advanced dry age-related macular degeneration: Current challenges and future prospects," 11 2015.

[43] M. K. Lin, Y.-T. Tsai, and S. H. Tsang, "Emerging Treatments for Retinitis Pigmentosa: Genes and stem cells, as well as new electronic and medical therapies, are gaining ground.," *Retinal physician*, vol. 12, pp. 52–70, 3 2015.

[44] H. Petrs-Silva and R. Linden, "Advances in gene therapy technologies to treat retinitis pigmentosa," 12 2013.

[45] L. F. Hernández-Zimbrón, R. Zamora-Alvarado, L. O.-D. l. Paz, R. Velez-Montoya, E. Zenteno, R. Gulias-Cañizo, H. Quiroz-Mercado, and R. Gonzalez-Salinas, "Age-Related Macular Degeneration: New Paradigms for Treatment and Management of AMD," *Oxidative Medicine and Cellular Longevity*, vol. 2018, 2018.

[46] Y. He, Y. Zhang, X. Liu, E. Ghazaryan, Y. Li, J. Xie, and G. Su, "Recent advances of stem cell therapy for retinitis pigmentosa," 8 2014.

[47] Y. H. L. Luo and L. da Cruz, "The Argus® II Retinal Prosthesis System," 1 2016.

[48] D. Nanduri, I. Fine, A. Horsager, G. M. Boynton, M. S. Humayun, R. J. Greenberg, and J. D. Weiland, "Frequency and amplitude modulation have different effects on the percepts elicited by retinal stimulation," *Investigative Ophthalmology and Visual Science*, vol. 53, pp. 205–214, 1 2012.

[49] H. Lorach, G. Goetz, R. Smith, X. Lei, Y. Mandel, T. Kamins, K. Mathieson, P. Huie, J. Harris, A. Sher, and D. Palanker, "Photovoltaic restoration of sight with high visual acuity," *Nature Medicine*, vol. 21, no. 5, pp. 476–482, 2015.

[50] K. Stingl, K. U. Bartz-Schmidt, D. Besch, C. K. Chee, C. L. Cottriall, F. Gekeler, M. Groppe, T. L. Jackson, R. E. MacLaren, A. Koitschev, A. Kusnyerik, J. Neffendorf, J. Nemeth, M. A. N. Naeem, T. Peters, J. D. Ramsden, H. Sachs, A. Simpson, M. S. Singh, B. Wilhelm, D. Wong, and E. Zrenner, "Subretinal Visual Implant Alpha IMS - Clinical trial interim report," *Vision Research*, vol. 111, pp. 149–160, 2015.

[51] K. Stingl, R. Schippert, K. U. Bartz-Schmidt, D. Besch, C. L. Cottriall, T. L. Edwards, F. Gekeler, U. Greppmaier, K. Kiel, A. Koitschev, L. Kühlewein, R. E. MacLaren, J. D. Ramsden, J. Roider, A. Rothermel, H. Sachs, G. S. Schröder, J. Tode, N. Troelenberg, and E. Zrenner, "Interim Results of a Multicenter Trial with the New Electronic Subretinal Implant Alpha AMS in 15 Patients Blind from Inherited Retinal Degenerations," *Frontiers in Neuroscience*, vol. 11, p. 445, 8 2017.

[52] K. Mathieson, J. Loudin, G. Goetz, P. Huie, L. Wang, T. I. Kamins, L. Galambos, R. Smith, J. S. Harris, A. Sher, and D. Palanker, "Photovoltaic retinal prosthesis with high pixel density," *Nature Photonics*, vol. 6, pp. 391–397, 6 2012.

[53] J. D. Loudin, D. M. Simanovskii, K. Vijayraghavan, C. K. Sramek, A. F. Butterwick, P. Huie, G. Y. McLean, and D. V. Palanker, "Optoelectronic retinal prosthesis: system design and performance," *Journal of Neural Engineering*, vol. 4, p. S72, 2 2007.

[54] K. Gregory-Evans, M. E. Pennesi, and R. G. Weleber, "Retinitis Pigmentosa and Allied Disorders," in *Retina Fifth Edition*, vol. 2, pp. 761–835, Elsevier Inc., 12 2012.

[55] A. L. Hodgkin and A. F. Huxley, "A quantitative description of membrane current and its application to conduction and excitation in nerve," *The Journal of Physiology*, vol. 117, pp. 500–544, 8 1952.

[56] T. H. Bullock, R. Orkand, and A. Grinnell, *Introduction to Nervous Systems*. San Francisco: W. H. Freeman, 1977.

[57] B. Coburn, "Neural modeling in electrical-stimulation," *Critical reviews in biomedical engineering*, vol. 17, no. 2, pp. 133–178, 1989.

[58] F. Rattay, "Analysis of Models for External Stimulation of Axons," *IEEE Transactions on Biomedical Engineering*, vol. BME-33, no. 10, pp. 974–977, 1986.

[59] S. Joucla and B. Yvert, "Modeling extracellular electrical neural stimulation: From basic understanding to MEA-based applications," *Journal of Physiology Paris*, vol. 106, pp. 146–158, 5 2012.

[60] F. Rattay, "Analysis of Models for Extracellular Fiber Stimulation," *IEEE Transactions on Biomedical Engineering*, vol. 36, no. 7, pp. 676–682, 1989.

[61] F. Rattay, "The basic mechanism for the electrical stimulation of the nervous system," *Neuroscience*, vol. 89, pp. 335–346, 3 1999.

[62] C. C. McIntyre, S. Mori, D. L. Sherman, N. V. Thakor, and J. L. Vitek, "Electric field and stimulating influence generated by deep brain stimulation of the subthalamic nucleus," *Clinical Neurophysiology*, vol. 115, no. 3, pp. 589–595, 2004.

[63] L. Guo, J. P. Cranford, J. C. Neu, and W. K. Neu, "Activating function of needle electrodes in anisotropic tissue," *Medical and Biological Engineering and Computing*, vol. 47, pp. 1001–1010, 7 2009.

[64] F. Rattay, H. Bassereh, and A. Fellner, "Impact of Electrode Position on the Elicitation of Sodium Spikes in Retinal Bipolar Cells," *Scientific Reports*, vol. 7, pp. 1–12, 12 2017.

[65] P. Werginz, H. Benav, E. Zrenner, and F. Rattay, "Modeling the response of ON and OFF retinal bipolar cells during electric stimulation," *Vision Research*, vol. 111, pp. 170–181, 6 2015.

[66] R. J. Jensen, J. F. Rizzo, O. R. Ziv, A. Grumet, and J. Wyatt, "Thresholds for activation of rabbit retinal ganglion cells with an ultrafine, extracellular microelectrode," *Investigative Ophthalmology and Visual Science*, vol. 44, pp. 3533–3543, 8 2003.

[67] S. S. Nagarajan, D. M. Durand, and E. N. Warman, "Effects of Induced Electric Fields on Finite Neuronal Structures: A Simulation Study," *IEEE Transactions on Biomedical Engineering*, vol. 40, no. 11, pp. 1175–1188, 1993.

[68] A. J. Bard and L. R. Faulkner, *Electrochemical Methods: Fundamentals and Applications*. John Wiley & Sons, Inc., 2nd ed., 2001.

[69] D. L. Guyton and F. Terry Hambrecht, "Theory and design of capacitor electrodes for chronic stimulation," *Medical & Biological Engineering*, vol. 12, pp. 613–620, 9 1974.

[70] S. M. Wellman, J. R. Eles, K. A. Ludwig, J. P. Seymour, N. J. Michelson, W. E. McFadden, A. L. Vazquez, and T. D. Kozai, "A Materials Roadmap to Functional Neural Interface Design," 3 2018.

[71] S. Negi, R. Bhandari, and F. Solzbacher, "A novel technique for increasing charge injection capacity of neural electrodes for efficacious and safe neural stimulation," in *Proceedings of the Annual International Conference of the IEEE Engineering in Medicine and Biology Society, EMBS*, pp. 5142–5145, 2012.

[72] M. Schaldach, M. Hubmann, A. Weikl, and R. Hardt, "Sputter-Deposited TiN Electrode Coatings for Superior Sensing and Pacing Performance," *Pacing and Clinical Electrophysiology*, vol. 13, pp. 1891–1895, 12 1990.

[73] A. Norlin, J. Pan, and C. Leygraf, "Investigation of Electrochemical Behavior of Stimulation/Sensing Materials for Pacemaker Electrode Applications," *Journal of The Electrochemical Society*, vol. 152, p. J7, 12 2005.

[74] R. Fiáth, B. C. Raducanu, S. Musa, A. Andrei, C. M. Lopez, C. van Hoof, P. Ruther, A. Aarts, D. Horváth, and I. Ulbert, "A silicon-based neural probe with densely-packed low-impedance titanium nitride microelectrodes for ultrahigh-resolution in vivo recordings," *Biosensors and Bioelectronics*, vol. 106, pp. 86–92, 5 2018.

[75] K. Wang, H. A. Fishman, H. Dai, and J. S. Harris, "Neural Stimulation with a Carbon Nanotube Microelectrode Array,"

[76] T. Gabay, M. Ben-David, I. Kalifa, R. Sorkin, Z. R. Abrams, E. Ben-Jacob, and Y. Hanein, "Electro-chemical and biological properties of carbon nanotube based multi-electrode arrays," *Nanotechnology*, vol. 18, p. 035201, 1 2007.

[77] F. Vitale, S. R. Summerson, B. Aazhang, C. Kemere, and M. Pasquali, "Neural stimulation and recording with bidirectional, soft carbon nanotube fiber microelectrodes," *ACS Nano*, vol. 9, pp. 4465–4474, 4 2015.

[78] S. Nimbalkar, E. Castagnola, A. Balasubramani, A. Scarpellini, S. Samejima, A. Khorasani, A. Boissenin, S. Thongpang, C. Moritz, and S. Kassegne, "Ultra-Capacitive Carbon Neural Probe Allows Simultaneous Long-Term Electrical Stimulations and High-Resolution Neurotransmitter Detection," *Scientific Reports*, vol. 8, pp. 1–14, 12 2018.

[79] R. de Levie, "On porous electrodes in electrolyte solutions. I. Capacitance effects," *Electrochimica Acta*, vol. 8, pp. 751–780, 10 1963.

[80] A. Tiliakos, A. M. Trefilov, E. Tanas, A. Balan, and I. Stamatin, "Space-Filling Supercapacitor Carpets: Highly scalable fractal architecture for energy storage," *Journal of Power Sources*, vol. 384, pp. 145–155, 4 2018.

[81] L. V. Thekkekara and M. Gu, "Bioinspired fractal electrodes for solar energy storages," *Scientific Reports*, vol. 7, no. February, p. 45585, 2017.

[82] N. A. Saidatul, A. A. Azremi, R. B. Ahmad, P. J. Soh, and F. Malek, "A development of fractal PIFA (Planar Inverted F Antenna) with bandwidth enhancement for mobile phone applications," in *Loughborough Antennas and Propagation Conference, LAPC 2009 - Conference Proceedings*, pp. 113–116, 12 2009.

[83] C. P. Baliarda, J. Romeu, and A. Cardama, "The Koch monopole: A small fractal antenna," *IEEE Transactions on Antennas and Propagation*, vol. 48, no. 11, pp. 1773–1781, 2000.

[84] J. a. Fan, W.-H. Yeo, Y. Su, Y. Hattori, W. Lee, S.-Y. Jung, Y. Zhang, Z. Liu, H. Cheng, L. Falgout, M. Bajema, T. Coleman, D. Gregoire, R. J. Larsen, Y. Huang, and J. a. Rogers, "Fractal design concepts for stretchable electronics.," *Nature communications*, vol. 5, p. 3266, 2014.

[85] W. J. Watterson, R. D. Montgomery, and R. P. Taylor, "Fractal Electrodes as a Generic Interface for Stimulating Neurons," *Scientific Reports*, vol. 7, p. 6717, 12 2017.

[86] W. J. Watterson, R. D. Montgomery, and R. P. Taylor, "Modeling the Improved Visual Acuity Using Photodiode Based Retinal Implants Featuring Fractal Electrodes," *Frontiers in Neuroscience*, vol. 12, p. 277, 4 2018.

[87] L. Golestanirad, B. Elahi, A. Molina, J. R. Mosig, C. Pollo, R. Chen, and S. J. Graham, "Analysis of fractal electrodes for efficient neural stimulation," *Frontiers in Neuroengineering*, vol. 6, p. 3, 7 2013.

[88] H. Park, P. Takmakov, and H. Lee, "Electrochemical Evaluations of Fractal Microelectrodes for Energy Efficient Neurostimulation,"

[89] X. F. Wei and W. M. Grill, "Analysis of high-perimeter planar electrodes for efficient neural stimulation.," *Frontiers in neuroengineering*, vol. 2, p. 15, 2009.

[90] M. Bockrath, N. Markovic, A. Shepard, M. Tinkham, L. Gurevich, L. P. Kouwenhoven, M. W. Wu, and L. L. Sohn, "Scanned Conductance Microscopy of Carbon Nanotubes and λ-DNA,"

[91] C. Staii, A. T. Johnson, and N. J. Pinto, "Quantitative Analysis of Scanning Conductance Microscopy,"

[92] H. J. Shih and P. J. Shih, "Tip effect of the tapping mode of atomic force microscope in viscous fluid environments," *Sensors (Switzerland)*, vol. 15, pp. 18381–18401, 7 2015.

[93] P. Roach, T. Parker, N. Gadegaard, and M. R. Alexander, "Surface strategies for control of neuronal cell adhesion: A review," 6 2010.

[94] P. J. Rousche, D. S. Pellinen, D. P. Pivin, J. C. Williams, R. J. Vetter, and D. R. Kipke, "Flexible polyimide-based intracortical electrode arrays with bioactive capability," *IEEE Transactions on Biomedical Engineering*, vol. 48, no. 3, pp. 361–370, 2001.

[95] V. S. Polikov, P. A. Tresco, and W. M. Reichert, "Response of brain tissue to chronically implanted neural electrodes," 10 2005.

[96] L. A. Flanagan, Y.-E. Ju, B. Marg, M. Osterfield, and P. A. Janmey, "Neurite branching on deformable substrates," *Neuroreport*, vol. 13, no. 18, p. 2411, 2002.

[97] A. P. Balgude, X. Yu, A. Szymanski, and R. V. Bellamkonda, "Agarose gel stiffness determines rate of DRG neurite extension in 3D cultures," *Biomaterials*, vol. 22, pp. 1077–1084, 5 2001.

[98] S. P. Khan, G. G. Auner, and G. M. Newaz, "Influence of nanoscale surface roughness on neural cell attachment on silicon," *Nanomedicine: Nanotechnology, Biology, and Medicine*, vol. 1, pp. 125–129, 6 2005.

[99] Y. W. Fan, F. Z. Cui, L. N. Chen, Y. Zhai, Q. Y. Xu, and I. S. Lee, "Adhesion of neural cells on silicon wafer with nano-topographic surface," *Applied Surface Science*, vol. 187, pp. 313–318, 2 2002.

[100] J. W. Salatino, K. A. Ludwig, T. D. Kozai, and E. K. Purcell, "Glial responses to implanted electrodes in the brain," *Nature Biomedical Engineering*, vol. 1, pp. 862–877, 11 2017.

[101] J. L. McKenzie, M. C. Waid, R. Shi, and T. J. Webster, "Decreased functions of astrocytes on carbon nanofiber materials," *Biomaterials*, vol. 25, pp. 1309–1317, 3 2004.

[102] G. Piret, M. T. Perez, and C. N. Prinz, "Support of Neuronal Growth Over Glial Growth and Guidance of Optic Nerve Axons by Vertical Nanowire Arrays," *ACS Applied Materials and Interfaces*, vol. 7, pp. 18944–18948, 9 2015.

[103] L. Kam, W. Shain, J. N. Turner, and R. Bizios, "Correlation of astroglial cell function on micro-patterned surfaces with specific geometric parameters," *Biomaterials*, vol. 20, pp. 2343–2350, 12 1999.

[104] M. P. Mattson, R. C. Haddon, and A. M. Rao, "Molecular functionalization of carbon nanotubes and use as substrates for neuronal growth," *Journal of Molecular Neuroscience*, vol. 14, no. 3, pp. 175–182, 2000.

[105] J. Liu, F. Appaix, O. Bibari, G. Marchand, A.-L. Benabid, F. Sauter-Starace, and M. D. Waard, "Control of neuronal network organization by chemical surface functionalization of multi-walled carbon nanotube arrays," *Nanotechnology*, vol. 22, no. 19, p. 195101, 2011.

[106] M. David-Pur, L. Bareket-Keren, G. Beit-Yaakov, D. Raz-Prag, and Y. Hanein, "All-carbon-nanotube flexible multi-electrode array for neuronal recording and stimulation," *Biomedical Microdevices*, vol. 16, pp. 43–53, 2 2014.

[107] E. W. Wong, P. E. Sheehan, and C. M. Lieber, "Nanobeam mechanics: Elasticity, strength, and toughness of nanorods and nanotubes," *Science*, vol. 277, pp. 1971–1975, 9 1997.

[108] G. Cellot, E. Cilia, S. Cipollone, V. Rancic, A. Sucapane, S. Giordani, L. Gambazzi, H. Markram, M. Grandolfo, D. Scaini, F. Gelain, L. Casalis, M. Prato, M. Giugliano, and L. Ballerini, "Carbon nanotubes might improve neuronal performance by favouring electrical shortcuts," *Nature Nanotechnology*, vol. 4, no. 2, pp. 126–133, 2009.

[109] R. Sorkin, A. Greenbaum, M. David-Pur, S. Anava, A. Ayali, E. Ben-Jacob, and Y. Hanein, "Process entanglement as a neuronal anchorage mechanism to rough surfaces," *Nanotechnology*, vol. 20, p. 015101, 1 2009.

[110] C. Nick, S. Yadav, R. Joshi, C. Thielemann, and J. J. Schneider, "Growth and structural discrimination of cortical neurons on randomly oriented and vertically aligned dense carbon nanotube networks," pp. 1575–1579, 2014.

[111] X. Zhang, S. Prasad, S. Niyogi, M. Ozkan, and C. Ozkan, "Guided Neurite Growth on Patterned Carbon Nanotubes,"

[112] T. Gabay, E. Jakobs, E. Ben-Jacob, and Y. Hanein, "Engineered self-organization of neural networks using carbon nanotube clusters," *Physica A: Statistical Mechanics and its Applications*, vol. 350, pp. 611–621, 5 2005.

[113] Messina A, Mangione A, Basirico L, and M. Jc, "Basic Research for Peripheral Neural Regeneration by CNTs, A Preliminary " in vitro " Study," *J Nanomed Nanotechnol*, vol. 6, no. 6, 2015.

[114] S. Johnen, F. Meißner, M. Krug, T. Baltz, I. Endler, W. Mokwa, and P. Walter, "Properties of Retinal Precursor Cells Grown on Vertically Aligned Multiwalled Carbon Nanotubes Generated for the Modification of Retinal Implant-Embedded Microelectrode Arrays," *Journal of Ophthalmology*, vol. 2016, pp. 1–13, 4 2016.

[115] A. Shoval, C. Adams, M. David-Pur, M. Shein, Y. Hanein, and E. Sernagor, "Carbon nanotube electrodes for effective interfacing with retinal tissue.," *Frontiers in neuroengineering*, vol. 2, p. 4, 2009.

[116] C. G. Eleftheriou, J. B. Zimmermann, H. D. Kjeldsen, M. David-Pur, Y. Hanein, and E. Sernagor, "Carbon nanotube electrodes for retinal implants: A study of structural and functional integration over time," *Biomaterials*, vol. 112, pp. 108–121, 1 2017.

[117] D. Wu, E. S. Pak, C. J. Wingard, and A. K. Murashov, "Multi-walled carbon nanotubes inhibit regenerative axon growth of dorsal root ganglia neurons of mice," *Neuroscience Letters*, vol. 507, pp. 72–77, 1 2012.

[118] L. Delzeit, C. V. Nguyen, B. Chen, R. Stevens, A. Cassell, J. Han, and M. Meyyappan, "Multiwalled carbon nanotubes by chemical vapor deposition using multilayered metal catalysts," *Journal of Physical Chemistry B*, vol. 106, pp. 5629–5635, 6 2002.

[119] M. K. Hancock, L. Kopp, N. Kaur, and B. J. Hanson, "A Facile Method for Simultaneously Measuring Neuronal Cell Viability and Neurite Outgrowth," *Current Chemical Genomics and Translational Medicine*, vol. 9, pp. 6–16, 3 2015.

[120] G. Piret, M. T. Perez, and C. N. Prinz, "Neurite outgrowth and synaptophysin expression of postnatal CNS neurons on GaP nanowire arrays in long-term retinal cell culture," *Biomaterials*, vol. 34, pp. 875–887, 1 2013.

[121] C. Wu, J. J. Schulte, K. J. Sepp, J. T. Littleton, and P. Hong, "Automatic robust neurite detection and morphological analysis of neuronal cell cultures in high-content screening," *Neuroinformatics*, vol. 8, pp. 83–100, 6 2010.

[122] D. B. Williams and C. B. Carter, *Transmission Electron Microscopy: A Textbook for Materials Science*. Boston, MA: Springer, 1996.

[123] Y. Liu, Y. Zhao, B. Sun, and C. Chen, "Understanding the toxicity of carbon nanotubes," *Accounts of Chemical Research*, vol. 46, pp. 702–713, 3 2013.

[124] G. H. Jeong, N. Olofsson, L. K. Falk, and E. E. Campbell, "Effect of catalyst pattern geometry on the growth of vertically aligned carbon nanotube arrays," *Carbon*, vol. 47, pp. 696–704, 3 2009.

[125] J. N. Turner, W. Shain, D. H. Szarowski, M. Andersen, S. Martins, M. Isaacson, and H. Craighead, "Cerebral astrocyte response to micromachined silicon implants," *Experimental Neurology*, vol. 156, pp. 33–49, 3 1999.

[126] P. C. Georges, W. J. Miller, D. F. Meaney, E. S. Sawyer, and P. A. Janmey, "Matrices with compliance comparable to that of brain tissue select neuronal over glial growth in mixed cortical cultures," *Biophysical Journal*, vol. 90, no. 8, pp. 3012–3018, 2006.

[127] S. Lee, J. Ahn, H. Yoo, S. Jung, S. Oh, S. Park, and D. Cho, "Electrical characteristics of 2D and 3D microelectrodes for high-resolution retinal prostheses," in *Proceedings of the Annual International Conference of the IEEE Engineering in Medicine and Biology Society, EMBS*, pp. 3535–3538, 2013.

[128] S. Lee, J. H. Ahn, J. M. Seo, H. Chung, and D. I. ho, "Electrical characterization of 3D au microelectrodes for use in retinal prostheses," *Sensors (Switzerland)*, vol. 15, pp. 14345–14355, 6 2015.

[129] T. Fujisawa, T. Noda, M. Hayashi, R. Kobe, H. Tashiro, H. Takehara, K. Sasagawa, T. Tokuda, C.-Y. Wu, and J. Ohta, "Performance Improvement of a Micro-stimulus Electrode for Retinal Prosthesis by Introducing a High-Performance Material and a Three-Dimensional Structure," *Sensors and Materials*, p. 1303, 2016.

[130] S. M. Sze and M. K. Lee, *Semiconductor Devices - Physics and Technology*. John Wiley & Sons Inc., 3rd ed., 2012.

[131] S. P. Lacour, S. Benmerah, E. Tarte, J. Fitzgerald, J. Serra, S. McMahon, J. Fawcett, O. Graudejus, Z. Yu, and B. Morrison, "Flexible and stretchable micro-electrodes for in vitro and in vivo neural interfaces," 10 2010.

[132] N. Lago and A. Cester, "Flexible and organic neural interfaces: A review," 12 2017.